Gecko Adhesion and Gecko-Inspired Dry Adhesives: From Fundamentals to Characterization and Fabrication Aspects

by

Hadi Izadi

A thesis
presented to the University of Waterloo
in fulfillment of the
thesis requirement for the degree of
Doctor of Philosophy
in
Chemical Engineering

Waterloo, Ontario, Canada, 2014

AUTHOR'S DECLARATION

I hereby declare that I am the sole author of this thesis. This is a true copy of the thesis, including any required final revisions, as accepted by my examiners.

I understand that my thesis may be made electronically available to the public.

Abstract

This study focuses on fabrication of dry adhesives mimicking gecko adhesion. We also look into the origin of the supreme adhesion of geckos, which have inspired the fabrication of fibrillar dry adhesives during the last decade or so. In principle, the superior material properties of β-keratin (the main material comprising the fibrillar feature on gecko toe pads) along with the hierarchical high aspect-ratio fibrillar structure of geckos' foot pad have enabled geckos to stick readily and rapidly to almost any surface in both dry and wet conditions. In this research, non-sticky fluoropolymer (Teflon AF) resembling β-keratin rigidity and having an extremely low surface energy and dielectric constant was applied to fabricate a novel dry adhesive consisting of extremely high aspect-ratio nanopillars (200 nm in diameter) terminated with a fluffy top nanolayer. Both the nanopillars and the terminating layer were fabricated concurrently by replica-molding using a nanoporous anodic aluminum oxide membrane as the mold. In particular, upon infiltration of Teflon AF melt into the anodic aluminum oxide nanopores, the polymer melt fingered over the pore walls. The fingerlike structure formed during infiltration, subsequently collapsed after removal of the mold, developing a unique sheet-like nanostructure on top of the base nanopillars. Concurrent fabrication of the terminating nanostructure helps the fabrication of extremely high aspect-ratio (27.5–225) nanopillars which, up to an aspect-ratio of 185, neither collapse at the tip nor bundle. In order to fabricate nanopillars of different topographical properties, in our first approach, the height of the nanopillars as well as the size and density of the terminating nanostructure are carefully controlled by adjusting the processing temperature.

Following that, a novel replica-molding technique for fabrication of bi-level Teflon AF nanopillars is reported. The developed technique relies on the concurrent heating and cooling of the Teflon AF melt which filled vertically-aligned alumina nanochannels. Unlike conventional polymer infiltration methods which consist of filling the mold by only heating the polymer above its glass transition temperature, in our novel method, the polymer melt is also simultaneously cooled down during the infiltration process. Concurrent cooling of the Teflon AF melt allows control over the interfacial instabilities of the polymer thin film, which forms ahead of the polymer melt upon its infiltration into the alumina nanochannels. Doing so, the geometrical properties of the subsequently developed peculiar fluffy nanostructure – after removal of the mold – on top of the extremely high aspect-ratio Teflon AF nanopillars (~25 μm tall) are modified.

In this project, we have also shown that the adhesion of the fabricated dry adhesives for the most part arises from electrostatic interactions of the applied polymer. In other words, Teflon AF, having an exceptional potential for developing electric charges at its surface upon contact with other materials via the so-called contact electrification phenomenon, can develop significant electrostatic interactions at its surface upon contact. In the current thesis, tribological results were discussed in detail to clarify the contribution of the structural properties of the fabricated dry adhesives toward their remarkable adhesion and friction forces generated via contact electrification. Nanopillars of specific geometrical properties have achieved remarkable adhesion and friction strengths, up to ~2.1 N/cm^2 and 17 N/cm^2, respectively (up to ~2.1 and 1.7 times larger than those of a gecko toe pad).

It is commonly accepted that the adhesive performance of other synthetic bio-inspired dry adhesives is due to the formation of van der Waals interactions at the tip or side of the dry adhesives fibrils with the substrate they are brought into contact with. However, what has been usually neglected in this connection is that electrostatic interactions may also be developed at the contact between any two materials via the familiar contact electrification phenomenon. Although contact electrification is common and can have a large influence on interfacial interaction forces, its impact on adhesive properties of synthetic dry adhesives has been overlooked. Our results on adhesion of bi-level Teflon AF nanopillars, which can generate strong adhesion forces relying on electrostatic interactions arising from contact electrification, have brought to light again the idea that charging the surface of dry adhesives, specifically polymeric ones, can play a very crucial role in their adhesive behavior. From this perspective, the main reasons that have caused this lack of attention to this concept and the possible contributions of contact electrification to interfacial interactions of polymeric dry adhesives, other than bi-level Teflon AF nanopillars, are also thoroughly discussed in this thesis.

Besides synthetic fibrillar dry adhesives, the possibility of the occurrence of contact electrification and its contribution to the supreme dry adhesion of geckos have also been overlooked for several decades. In this research, by the simultaneous measurement of electric charges and adhesion forces that gecko toe pads develop on two distinct substrates (a sticky and a non-sticky one), we have shown that the toe pads generate significantly large amounts of electric charge on both substrates. More importantly, we have found that there is a direct correlation between the contact electrification-driven electrostatic forces and the measured

adhesion forces. Otherwise stated, we have shown that what makes the difference that geckos stick strongly to one surface and not to the other are the electrostatic interactions arising from contact electrification, and not van der Waals interactions, which have been considered as the prime source of adhesion of geckos for many years.

Acknowledgements

First and foremost, I would like to thank my supervisor, Professor Alexander Penlidis, for all his guidance and support throughout my PhD research. To put all my appreciation in a sentence, I should say I was honored to do my PhD under his supervision.

I would also like to pass my great appreciation to Professor Neil McManus for his insightful guidance and support throughout these years. Many thanks go to my friends and colleagues at the University of Waterloo for their patience and support during the course of my PhD career.

I wish to acknowledge financial support from the Natural Sciences and Engineering Research Council (NSERC) of Canada and the Canada Research Chair (CRC) program.

Last but not least, my sincere gratitude goes to my parents and my brother for all their support and patience, not only during my PhD career, but also throughout my whole life.

Table of Contents

List of Figures

List of Tables

Chapter 1. Introduction, Motivation, and Thesis Outline

It is not exactly known when the first time was that human beings used nature as the prototype to produce biomimetic tools and devices, but it is well accepted that if it was not for the imitation of flying birds, maybe airplanes would never exist! Transferring ideas from nature to technology is essentially a shortcut to fabrication of novel materials and structures by employing biological ideas and principles which nature has developed over millions of years of evolution [1]. However, 'prototyping' biological systems for the production of biomimetic replicas requires that these 'prototypes' and also the produced 'replicas' be experimentally examined and theoretically analyzed.

In this connection, groundbreaking research has been conducted – during the last century or so – to shed light on the principles of fibrillar adhesion systems that animals and insects, like geckos and spiders, employ for their locomotion [2-14]. In the search for fabricating novel synthetic bio-inspired fibrillar adhesives (also known as dry adhesives) with high-end properties, a new series of studies was initiated in the early 2000s [15-19], contemporary with elucidating the adhesion mechanism of the world supreme climbers, namely, geckos [2,3]. Strong, directional, and repeatable, the flawless adhesion of geckos has become the prime example for the fabrication of the majority of bio-inspired dry adhesives, essentially the adhesives of a new era! Keeping the sticky foot pads of geckos in mind, scientists are basically trying to pursue the fantasy of a science-fictional character, Spider-Man, a fantasy which nowadays is – more than ever – fairly close to reality.

The gecko's extraordinary climbing and locomotion abilities are attributed to arrays of thousands of fine microscopic fibrils (commonly named setae), which split up at the tips into hundreds of nanoscale spatulas [2,4,5]. The hierarchical level and high aspect-ratio (AR) of the structure which is mainly made up of a rigid material (*i.e.*, β-keratin, Young's modulus ≈ 2 GPa) [20,21], bring the effective elastic modulus of the whole setae arrays down to ~100 kPa, enhancing the compliance and adaptability of the toe pad to the substrate the animal wants to walk on or cling to [6]. For fabrication of a synthetic dry adhesive, such design constraints (*i.e.*, high AR and hierarchical structure) [16-18,22-24] point to the direction of a rigid material with low surface energy, thus allowing for the fabrication of tall and narrow pillars with a hierarchical level on top.

In the current research, we have succeeded in fabricating nanopillars terminated with a fluffy sheet-like nanostructure on the top, comparable (but not exactly identical) to both the flat structure of thin-film-terminated dry adhesives and the smaller-scale feature of hierarchical gecko-inspired adhesives (see Figure 1.1). The terminating nanostructure which effectively hindered the collapse of the nanopillars at the tip was initially developed upon infiltration of the employed polymer (Teflon AF; surface energy = 15.7 mJ/m^2, Young's modulus = 1.5 GPa) [25] into anodic aluminium oxide (AAO) nanopores. In principle, due to extremely high surface energy of AAO nanopore walls, the penetration of Teflon AF melt in the mold took place with formation of a thin (typically < 100 nm) precursor film ahead of the developing polymer melt. Caused by thermocapillarity-driven stresses at the contact line of

the precursor film, the generated thin film fingered over the nanopore walls (the so-called fingering phenomenon) [26-28], and resulted in the formation of a novel fingerlike structure ahead of the penetrating Teflon AF melt [29]. After solidification of the polymer melt and removal of the mold, the fingered hierarchical structure collapsed during the drying step and formed a fluffy sheet-like nanostructure on top of the nanopillars (Figure 1.1).

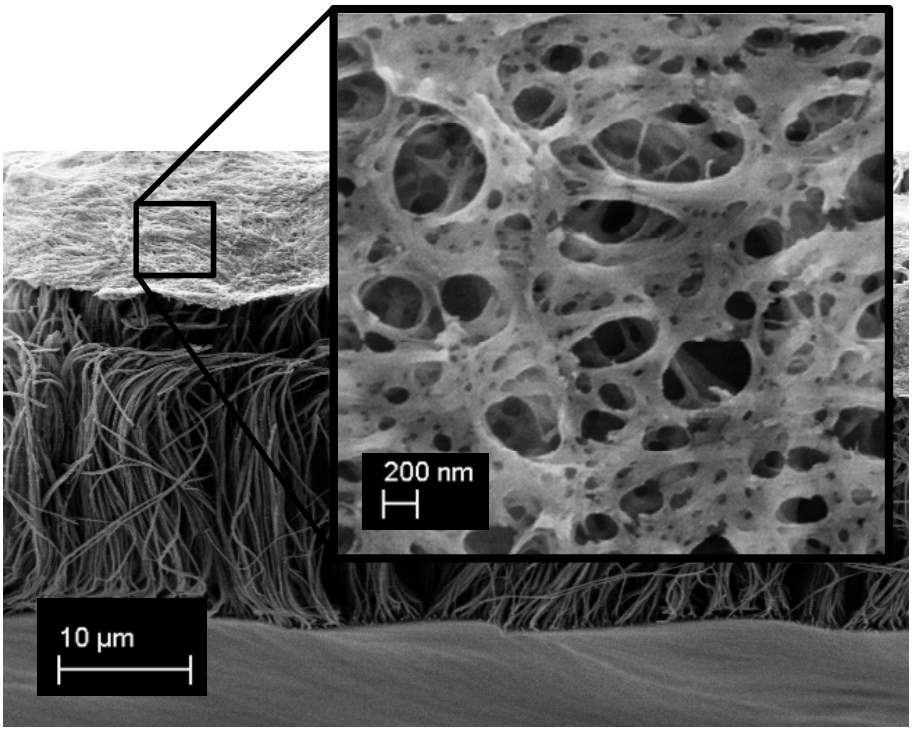

Figure 1.1. Scanning electron microscope (SEM) images (45°-view) of bi-level Teflon AF nanopillars. Extremely high AR (up to 185) nanopillars of 200 nm in diameter are terminated at the tip with a unique fluffy nanolayer of the same material. The magnified image is from the top.

Concurrent fabrication of the terminating nanostructure helped the fabrication of extremely high AR nanopillars which, up to an AR of 185, neither collapse at the tip nor bundle. In order to fabricate nanopillars of different topographical properties, the height of the nanopillars as well as the size and density of the terminating nanostructure were carefully

controlled by adjusting the processing temperature.

We have also developed a novel fabrication technique relying on the concurrent heating and cooling of the Teflon AF melt which filled vertically-aligned alumina nanochannels. Unlike conventional polymer infiltration methods which consist of filling the mold by only heating the polymer above its glass transition temperature, in this unique method, the polymer melt was also simultaneously cooled down during the infiltration process. Concurrent cooling of the Teflon AF melt allowed control over the interfacial instabilities of the polymer thin film, which formed ahead of the polymer melt upon its infiltration into the alumina nanochannels. Doing so, the geometrical properties of the peculiar fluffy nanostructure which was developed on top of the extremely high AR Teflon AF nanopillars were modified, while the height of the base nanopillars was kept constant.

Although the special properties of Teflon AF contributed to fabrication of a double-level and high AR nanopillars, it should be noted that in the sense of its application in dry adhesives, Teflon AF cannot effectively generate van der Waals (vdW) interactions, which have been assumed to form the basis of adhesion of gecko and gecko-inspired adhesives. However, Teflon AF, like other fluoropolymers, has the advantage of generating large electrostatic forces by getting charged at its surface upon contact with other materials via the so-called contact electrification (CE) phenomenon. CE refers basically to the separation of electric charges following contact between dissimilar materials or, in certain cases, between identical materials [30-33]. Although the precise understanding of this phenomenon for insulating

surfaces, known since antiquity, is still elusive [30-37], it is well known that upon contact of two materials, similar or dissimilar, electric charges would transfer between two surfaces and a net negative charge would develop over one surface, whereas the other surface would mainly host positive charges. Some of the charges transferred across the interface would separate upon detachment of the two bodies, leading to an electrostatic interaction and consequently adhesion between them [30-37], as schematically shown in Figure 1.2 for bi-level Teflon AF nanopillars in contact with a hemispherical fused silica probe.

It is worthwhile mentioning that the work of adhesion due to electrostatic interactions via CE can be much larger than that generated by short-range vdW forces, while it can even match the fracture energies of ionic-covalent materials [32]. Besides, it should be noted that CE at the surface of fluoropolymers (like Teflon AF) is more significant in comparison to other polymers in that they have very low dielectric constants, which along with the high electronegativity of fluorine-based units of their chains, facilitate the trapping of electric charges at their surface (Teflon AF has the lowest dielectric constant of any known solid organic polymer (ε = 1.93) [25]).

The special CE-driven adhesion of Teflon AF nanopillars helped them to generate extremely large adhesion forces, even up to ~100 times larger than those attainable by vdW forces [29]. The nanopillars of specific geometrical properties have achieved remarkable adhesion and friction strengths up to ~2.1 N/cm^2 and 17 N/cm^2 [29,38], respectively (~2.1 and 1.7 times larger than those of a gecko toe pad) [2].

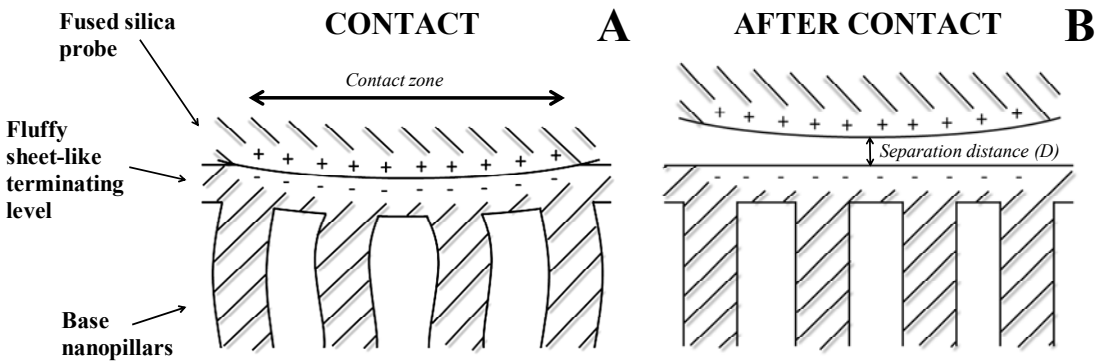

Figure 1.2. (A) Schematic of charge transfer via contact electrification in contact between Teflon AF nanopillars terminated with a fluffy sheet-like nanostructure and a hemispherical fused silica probe (8 mm in diameter). (B) Charges which separate upon detachment of the probe from the sample are generating electrostatic interaction between two surfaces at a separation distance (*D*).

Not only have the fabricated nanopillars generated considerable adhesion in dry conditions, but also certain types of them have managed to generate high pull-off forces under water (on average ~70% of the dry adhesion), which is a rare behavior among previously reported dry adhesives [39,40].

Even though bi-level Teflon AF nanopillars are the only reported dry adhesives so far which mainly rely for their performance on CE-driven electrostatic interactions, effect of surface charging and in turn, electrostatic interactions developed by it on the adhesive properties of other synthetic dry adhesives (SDAs), specifically polymeric ones, should not be taken lightly. More specifically, neither of the properties that enabled Teflon AF nanopillars to generate significant adhesion forces via CE-driven electrostatic interactions (*i.e.*, flexibility of the fibrillar structure and electrical properties of the polymer) are restricted only to this SDA. Regarding the former, it should be mentioned that having a soft conformable structure is not an exclusive feature for bi-level Teflon AF nanopillars. On the contrary, it is a

structural pre-requirement for any effective SDA, even those considered to work based on vdW interactions [15-18,22].

Besides, it should be noted that Teflon AF is not the only polymer which can get charged at the surface via CE. While Teflon AF and fluoropolymers, in general, are very efficient in trapping electric charges at their surfaces, they are only one type of polymers having this characteristic. For instance, other than Teflon (polytetrafluoroethylene; PTFE) [34-36,41-48], many other polymers such as polydimethylsiloxane (PDMS) [34-36,41-48], polyurethane (PU) [48], polycarbonate (PC) [35,36,45,49], polystyrene (PS) [34,44,45], poly(methyl methacrylate) (PMMA) [42,44,45,50,51], and polypropylene (PP) [34] have been widely employed in studies on CE over insulators. In fact, because of their insulating nature, the aforementioned polymers have the ability to hinder the transfer of surface charges into the polymer matrix and accordingly, they can motivate the efficient surface charging upon contact. In this regard, they have been widely used, alongside Teflon, in studies on CE of insulators. Here, it is also interesting to mention that all of the aforementioned polymers, with the exception of Teflon, have commonly been employed in the fabrication of SDAs as well. In general, polymeric dry adhesives are conventionally made from such insulating polymers as PDMS [39,52-61], PU [62,63], PC [23], PS [64], PMMA [65,66], or PP [67-71]. Hence, noticing that these polymers are all efficient surface charge trappers, it is expected that CE happens in an effective manner over polymeric SDAs made from these polymers and accordingly, must have a large impact on their adhesive properties.

Despite all these observations, little attention has been paid to date to the contribution of CE in the adhesive behavior of polymeric SDAs. The lack of attention in this regard is chiefly due to a lack of precise knowledge about CE in the case of insulating materials, which makes prediction of its occurrence very difficult. The relatively superficial understanding of CE over insulators requires, in fact, that occurrence of surface charging as well as its ultimate properties are monitored through real physical experiments. Even so, an experimental technique capable of characterizing the amount of electric charges which might develop over a polymeric dry adhesive upon contact, is still missing. As a matter of fact, the available tribological tests which are conventionally carried out to investigate the adhesive properties of SDAs, only report the absolute value of the surface forces, while nothing much can be determined from this absolute value about the specific contribution of electrostatic forces.

Not only is CE expected to contribute in the interfacial interactions of polymeric SDAs, but we have also shown that it plays a crucial role in gecko adhesion. Since the unique fibrillar feature of the toe pads of geckos allow them to develop a large actual area of contact with the substrate the animal is walking on or clinging to [2,4], the toe setae exchange significant numbers of electric charges with the contacted substrate via the CE phenomenon [30,31]. In the current research, by measuring the magnitude of the electric charges – together with the adhesion forces – that gecko foot pads develop in contact with different materials, the occurrence and effectiveness of CE and electrostatic interactions arising from it in gecko adhesion have also been investigated.

In the following chapter, general principles of gecko adhesion and gecko-inspired dry adhesives and the fabrication techniques for producing SDAs will be discussed. Details on the fabrication of the state-of-the-art bi-level Teflon AF nanopillars and their CE-driven adhesive properties, both in dry conditions and under water, are presented in Chapters 3–5. In Chapter 6, the possible contributions of CE in the interfacial interactions of polymeric SDAs, in general, along with the main reasons that have caused the lack of attention to this concept, are thoroughly discussed. Chapter 7 contains the details on the role of CE and the electrostatic interactions arising from it in the interfacial interactions of gecko toe pads and their contribution to gecko adhesion. Finally, the thesis ends with Chapter 8, with the main concluding remarks based on the results obtained in this study, the main contributions of the thesis, and also both short-term and long-term recommendations for future work of this project.

Chapter 2. Literature Background

2.1 Gecko adhesion

2.1.1 Adhesion and adhesives

There are many ways to define *adhesion* [72], as a bond, a phenomenon, or an interaction, in many contexts or perspectives of surface science [73,74], polymer science [75], or materials science [76]. Due to its interdisciplinary nature, adhesion includes a complicated set of inter-connected phenomena (occurring at a material surface and in its bulk), which is still far from being completely understood [77]. Here, we refer to adhesion as a *physical state of two similar or dissimilar materials coming into contact because of such surface attractive or adhesive forces as the van der Waals (vdW), electrostatic, and/or capillary forces*.

For most ordinary materials, their surfaces are rough, preventing an intimate contact, for a sufficient surface force to develop between the two surfaces. In engineering practice, a third material, called an *adhesive* [72], is commonly used to bond two dissimilar materials to form a laminated structure. Adhesives are soft or liquid-like materials in the form of either liquid, paste, or film so that they can conform to the rough surfaces of bonded materials forming intimate contacts [72,77].

The oldest – documented – use of adhesives by humans goes back to about 200,000 years ago. It appears that at that time, single-component natural adhesives, extracted from a – birch

– tree, were the sticky substances capable of holding things in place. It took a long time until about 5,000 years ago when adhesive materials were derived from other natural sources like animal tissues (*e.g.*, bones and skins) [78]. Despite this 'sluggish' start, production of adhesives has experienced a great boost during the last few centuries. The relatively recent large leap in adhesive technology is contemporary with the development of polymeric materials, which has led to the production of modern polymeric adhesives. From a consumer's point of view, however, production of the first pressure-sensitive adhesives (PSAs) – known to many as 'scotch tapes' – about 160 years ago and the development of duct tapes – an urgent necessity triggered by World War II – are perhaps the most important 'signposts' in adhesive technology [78].

Going through thousands of years of evolution, adhesives have found numerous applications in almost every facet of today's life; they represent indeed 'a way of life'! We use them for food and supplies packaging, labeling, wound-care dressing, surface protection, piping, sealing, furniture making, and for almost any other conceivable application [77,78]. Other than common everyday purposes, adhesives have also extensively contributed to such more complex modern industries as aerospace, electronics, and automobile; many parts in the fuselage, the wing structure, the cabin, and even the engine housing of aircrafts are typically bonded together by adhesives. Fastening the car windshield to its frame, bonding the car outer doors to their inner shell, and joining various car panels are all physically possible these days by using adhesives of specific types and properties [77].

The current multi-billion dollar industry of adhesives is offering a wide variety of adhesives formulated from both natural and synthetic materials. Natural adhesive materials (*e.g.*, starch, dextrin, gelatin, natural rubber, or shellac) are those substances derived from such natural sources as corn, wheat, tapioca, soya flour, skim milk, animal bone, fish skin, and also the rubber tree [78]. Synthetic adhesives, on the other hand, are chiefly made from certain types of polymers such as vinyls (*e.g.*, polyvinyl acetate (PVAc), polyvinyl alcohol (PVA), and polyvinyl ether (PVE)), synthetic rubbers (*e.g.*, polychloroprene (also known as neoprene), polyisobutylene (PIB), and polyurethane (PU)), and amine-based resins (*e.g.*, polyamide (PA), polyimide (PI), and polybenzimidazole (PBI)).

Refinement of existing adhesives and production of new ones in order to satisfy the more advanced human demands naturally need to go through the two important steps of synthesis and characterization. In particular, producing adhesives of superior – physical, chemical, and mechanical – properties inevitably involves the modification of the type and properties of the adhesive components through physical and/or chemical procedures. Producing an adhesive of particular properties encompasses – and requires an in-depth knowledge of – both the physics and chemistry of either the natural and/or synthetic materials which are employed for production of the adhesive. Like any other products, however, the final properties of the produced adhesives for their target application(s) need to be eventually characterized using suitable characterization methods. Various characterization techniques may be performed to study adhesive properties. Depending on the nature of the adhesive and also that of the adherend as well as the information required from the adhesion test, techniques ranging from

large-scale conventional methods, such as depth-sensing indentation, peeling tests, and shear adhesion tests, to more recent small-scale methods, including micro/nanotribological tests, can be carried out to investigate and evaluate the adhesive properties of an adhesive product [78,79].

2.1.2 Biological adhesion for locomotion

In dealing with real surfaces, which are usually rough and have complex shapes and features, using biological adhesion systems as the prototype could be very helpful. Independent evolution of biological adhesive surfaces (*e.g.*, hairy legs of insects or sticky foot pads of lizards) has enabled them to attach easily and detach rapidly from walls and ceilings [4,5,8,80]. Mimicry of these biological adhesion systems could be a promising approach in achieving repeatable, self-cleaning, flawless, and robust synthetic adhesion resembling its natural prototype [15-18,79].

Generally, biological adhesion systems can be categorized into two distinct mechanisms, namely, *wet adhesion* and *dry adhesion* [9,10]. Most insects rely on the wet adhesion mechanism, while lizards and spiders use dry adhesion. In dry adhesion systems, lizards and spiders (and even some insects) use the hairy attachment system of their feet; put otherwise, dry adhesion relies only on the fine hairy structure of the foot pad which is able to conform to most rough surfaces and develop a large number of contacts or large real contact area compared to flat surfaces [9,10,81]. On the other hand, most insects, which mostly benefit

from wet adhesion, secrete certain types of fluid into the contact area, which helps them to benefit also from capillary forces along with vdW and electrostatic forces. Expectedly, decrease in this secretion could dramatically decrease adhesion, indicating that this secretion layer is a crucial part of their attachment device [10]. It should be noted that these different mechanisms have their own advantages and disadvantages for insects and animals; that is, biological attachment mechanisms are specialized for different insects and animals, according to their needs and the environment in which they live.

From another point of view, sticky food pads of animals and insects can be categorized into two completely distinct groups: *smooth pads* and *hairy surfaces* (see Figure 2.1) [10].

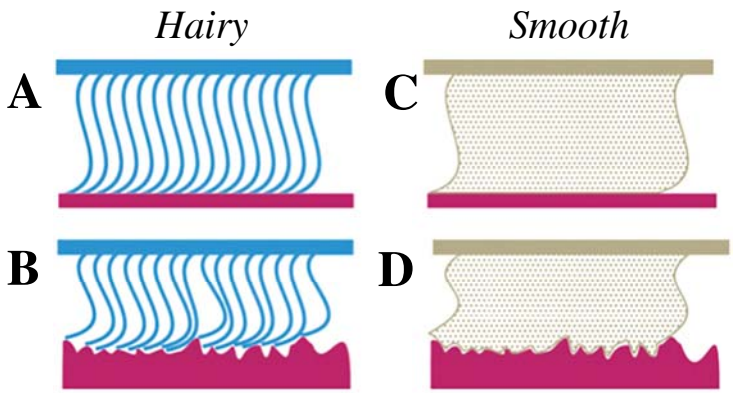

Figure 2.1. Diagram of the action of (A, B) hairy and (C, D) smooth pad attachment systems on (A, C) smooth and (B, D) rough substrates [10].

Smooth pads consist of a fibrous material with a specific inner structure which enables the pad to replicate the surface profile (Figures 2.1.C and 2.1.D). The filaments and fluid are covered by a thin-film surface layer [10]. The closest industrial product resembling these attachment systems in adaptability, viscoelasticity, and pressure sensitivity is PSAs. Hairy

pads (see Figures 2.1.A and 2.1.B), on the other hand, consist of fine and long surface outgrowths, terminated by thin-film tips of different shapes [9,10]. Hairy attachment pads, which could be found in some insects, spiders, and also animals like geckos, employ other features like flaw tolerance and lower sensitivity to roughness and contamination.

It is worthwhile mentioning that since animals cannot increase the area of the attachment in a way proportional to their body weight, the density of hairs sharply increases with increasing body weight. Besides, animals using the dry adhesion mechanism possess much higher density of hairs than those using wet adhesion; therefore, in selecting the prototype for the desired engineering adhesion system, a dry hairy adhesion system is a more interesting candidate. It is also interesting to note that the largest animals that use dry hairy adhesion for locomotion are geckos and therefore, could be the best candidate as a prototype for fabrication of dry fibrillar adhesives.

2.1.3 Adhesion of geckos

Geckos can attach and detach in milliseconds while running on almost any surface [4,5,82]. Recent experimental and theoretical studies have attributed the directional adhesion ability of geckos to the hierarchical structure of their toe pads [2,5,83]. Figure 2.2 illustrates this hierarchical structure from the molecular to the macroscopic level. The first level of hierarchy on their toe pad is the mesoscale setal arrays, called adhesive lamellae (Figure 2.2.B). Each seta (Figure 2.2.C), which is about 110 μm in length and 4.2 μm in diameter [4,5], branches at the end to form nanoscale arrays of hundreds of spatula structures (Figure

2.2.D), bringing the toe pads to an intimate contact with rough surfaces (on average, each gecko has approximately 6.5 million setae). Each spatula, which is 200–300 nm in length and also in width at the tip, has a thin (5–10 nm), roughly triangular end which is connected from its apex to the stalk of the spatula [4,5,84]. At the molecular level, setae are mostly composed of β-keratin (Figure 2.2.E), while also contain α-keratin and some minor proteins [20,21].

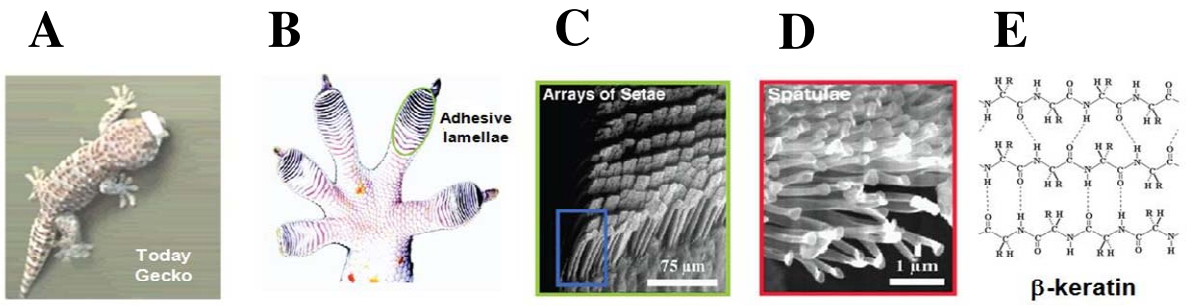

Figure 2.2. Hierarchical structures of a Tokay gecko. (A) A Tokay gecko climbing on a wall; (B) gecko foot pads sticky setal arrays called adhesive lamellae; (C) rows of setal arrays; (D) each seta terminating with 100–1000 spatulas; (E) the whole hierarchical feature of the toe pads is mainly composed of β-keratin.

The hierarchical structure of the fibrillar feature of gecko foot pad allows an intimate molecular contact of the foot with the surface. As mentioned earlier, in conventional adhesion, this could be achieved by using adhesives that flow in a liquid-like fashion to bring the surfaces into maximum contact. In the gecko adhesion system, however, the nano-sized spatulas which conform to the topography of the surface at small scales are responsible for surprisingly enhanced real contact area which will increase the adhesion for geckos [4,5,82]. Geckos can generate strong adhesion forces in both normal and shear directions (up to 1 N/cm^2 and 10 N/cm^2, respectively) [2]. Even so, geckos can detach from surfaces in milliseconds with no measurable detachment force. This contradiction has been described by

a peeling mechanism, the fact that geckos adhere to a surface not only via adhesion but also via friction, allowing the animal to attach strongly and detach easily [7,84].

2.2 Bio-inspired synthetic dry adhesives

Fabrication of dry adhesives inspired by the gecko lizard's toe pads has been a subject of great interest for the last decade or so [15-18,79]. From the humble beginnings as an adhesive which could hold a "Spider-Man toy" clinging with one of its hands to a horizontal glass plate, certain types of current bio-inspired dry adhesives can even hold a "human adult" hanging from a ceiling! Strength, repeatability, anisotropic behavior, and self-cleaning properties of certain types of gecko-inspired dry adhesives [16-18,79,85], mimicking those of the gecko lizard toe pads, have led to distinct applications, particularly in the production of climbing robots and wound-care dressing. Strong attachment and easy detachment, as prerequisites for any efficient synthetic dry adhesive, are actually the properties that any climbing robot – for either surveillance or search-and-rescue missions – can largely benefit from [1]. The same properties, on the other hand, have opened the door for the entry of dry adhesives into the realm of medical applications, where always a "strong adhesion" and an "easy peel-off" can be beneficial [1]. However, it should be noted that gecko-inspired dry adhesives fabricated so far have generally been faced with certain difficulties with respect to mass production for commercial applications. The low dimension of the patterned structures as well as the high cost and complexity of the current fabrication processes are basically the

main challenges, which have slowed down the transfer of gecko-inspired adhesives from research labs to the market.

2.2.1 Micro/nanofabrication for fabrication of synthetic dry adhesives

To transfer micro/nanoscale features onto distinct substrates to fabricate fibrillar adhesives like the fibrillar feature of gecko foot pad, different methods ranging from various lithographic methods (including photolithography, soft-lithography, electron beam lithography (EBL), and ion beam lithography (IBL)), to completely non-photolithographic methods (including micro/nano-machining, diblock copolymer self-assembly, and replica-molding), have been applied [79,86].

Indeed, among all micro/nanofabrication methods specifically for polymer surfaces, photolithography is the most well-known and versatile method. Fabrication of high aspect-ratio (AR) patterns, hierarchical structures, and even three-dimensional (3D) structures on polymer surfaces are all possible by advanced photolithography [86]. In spite of many unique benefits photolithography has, some of its disadvantages, such as the cost of maintaining a contamination-free condition in which it should be carried out and the cost of making a chrome-mask, has restricted its application for many large-scale and cost-effective needs [86]. These drawbacks have urged the necessity of maskless methods like two-photon lithography (TPL), EBL, IBL, or scanning probe resist lithography. However, although these so-called maskless methods are capable of serial writing and also fabrication of 3D

structures, their low-speed writing has restricted their application mostly for high-throughput needs. Besides, it should be noted that these serial writing and also machining methods, involve very expensive equipment which is not available in every lab.

Amongst non-photolithographic methods, however, replica-molding is indeed the most versatile and common micro/nanofabrication technique which is commonly employed for fabrication of fibrillar dry adhesives. Low cost, simplicity, and also its applicability for patterning of large surface areas are in fact the main advantages of method over photolithographic methods.

As a matter of fact, applying different preparation methods essentially affect the final characteristics and properties of the fabricated micro/nanostructures. There is not a better or worse micro/nanofabrication method; rather there is either appropriate or inappropriate method, depending on desired properties of the feature and also the type of the material used for fabrication of the dry adhesive. In other words, each method has its own advantages and disadvantages that could be used for different applications.

2.2.2 Dry adhesives: Choice of the material and structural design

Choosing an appropriate micro/nanofabrication technique for producing a fibrillar dry adhesive is basically dependent on adaptability of the employed method to both the nature of the material of the dry adhesive and also the geometrical properties that the fabricated

micro/nanostructures should have [16-18]. The choice of the material is very crucial toward the final adhesive performance of the dry adhesive; in the case of geckos, the fibrillar feature of the foot pads is mainly β-keratin [20,21]. β-keratin is basically a very rigid material with Young's modulus of ~2 GPa [6]. Even so, a very large AR of the setae and also the presence of the hierarchy on top of each seta (see Figure 2.2) brings the effective elastic modulus (E_{eff}) of the fibrillar feature of the food pad down to approximately 100 kPa, which is comparable to the elastic modulus of conventional PSAs [4,6]. In general, the effective elastic modulus of a fibrillar structure can be calculated by [6]

$$E_{eff} = \frac{3EIdsin(\theta)}{L^2 cos^2(\theta)[1 \pm \mu \tan(\theta)]}$$

Equation 2.1

where E is the elastic modulus of the polymer, $I = \pi r^4/4$ (r is the radius of each hair) is the moment of inertia, d is the pillar density, θ is the hair angle to its base, L is the length of each pillar, and μ is the friction coefficient. According to Equation 2.1, it might appear that materials of lower elasticity are more favorable for fabrication of fibrillar dry adhesives, seeing that they lead to lower effective elastic modulus of the fibrillar feature of the dry adhesive and therefore, better conformability of the dry adhesive to the roughness of the substrate in contact. But, in fact, there is an upper limit and lower limit for elasticity of the material forming micro/nanostructures! In particular, the employed material should be elastic enough to allow the conformation of the structure at small-scales (as Equation 2.1 indicates), given that stiff materials cannot bend and hence cannot adapt to micro/nanoscale roughness of the substrate in contact. Even so, very low elasticities will decrease the required energy for bending of pillars, leading to enhancement of the risk of the collapse of the pillar in the

lateral direction (the so-called condensation). Put otherwise, as the height increases, the actual stiffness of the pillars decreases and when the length of the pillar passes a specific height, the heads of the pillars start to collapse over each other, while further increase in the length of the pillars results in their bundling [19,58,87]. Basically, lateral collapse occurs when the adhesive forces between the fibers become stronger than the forces required to bend the fibers [88].

Rather than the softness of the employed material, the lateral collapse of fibrillar structures is also dependent on the geometrical properties of the fibrillar structure. Glassmaker *et al.* [87] suggested an empirical equation (see Equation 2.2) which can be employed to estimate the critical values for the height of a circular pillar after which condensation might occur. For a specific material with Young's modulus of E and surface energy of γ, the maximum height (L_{max}) for pillars before they start to collapse in the lateral direction can be calculated by [18]

$$L_{max} = \left(\frac{\pi^4 Er}{2^{11}\gamma\,(1-\upsilon^2)}\right)^{\frac{1}{12}}\left(\frac{12Er^3\left(\frac{W}{2}\right)^2}{\gamma}\right)^{\frac{1}{4}}$$

Equation 2.2

where r is the radius of each pillar, W is the distance between two neighboring pillars, and υ is the Poisson ratio of the polymer. Technically, by making taller and thinner (*i.e.*, softer) pillars, adaptability of the fibrillar dry adhesive to the substrate will increase, but the chances of lateral collapsing will also enhance.

Many successful high AR fibrillar structures as gecko-inspired adhesives are made from carbon nanotubes (CNTs) [16,18,85,89-91]. Having Young's modulus in the range of 10^{12}

Pa, which is three orders of magnitude higher than that of the most rigid polymers, extremely high AR nanopillars were fabricated from both single-walled and multi-walled CNTs, attaining adhesion and friction forces even higher than those of a natural gecko [16,18,85,89-91]. On the other hand, with polymeric dry adhesives and using even the most rigid polymers, the highest theoretical achievable AR is limited to 10–20 [18]. As discussed, fibrillar structures with higher ARs tend to collapse and/or bundle, unfavorably reducing the effective contact area while enhancing the stiffness of the surface, which dramatically reduces the chances for generating dry adhesion [19,58,87].

However, efficient polymeric dry adhesives having lower AR pillars but with hierarchical levels on top or terminated at the top with a thin film of the same material have recently been reported [23,24,52,54,63,71,92]. A smaller scale of the hierarchical level allows the dry adhesive to conform to the roughness of the substrate upon contact, leading to enhanced adhesion strength (*i.e.*, adhesion force per unit surface area) [23]. On the other hand, compliant thin film-terminated fibrillar structures can enhance the adhesion and friction strengths by means of increasing the actual contact area while they make the fibrillar structure more robust [52,56].

In addition to AR and having a hierarchical (or thin-film terminated) feature on top of each fibril of a dry adhesive, some other factors (like contact shape, contact size, and slope of pillars) which can also affect the adhesion properties of a dry adhesive have also been considered in the literature [10,88,93]. More details on the equations on critical geometrical

and mechanical values of structural dry adhesive surfaces can be found in the literature [55,88,94].

2.3 Sources of the adhesion of geckos and synthetic dry adhesives

As discussed, the mechanism of dry adhesion of natural fibrillar adhesives, such as that of gecko foot pads, is basically relying on conformation of the flexible fibrils of the dry adhesive to the roughness of the substrate that they come into contact with; the tip or even the side of the micro/nanoscale hairs make contact with the substrate and adhere to it via certain types of interfacial forces [2,4,9,11,80,95,96]. But, in particular, what type of interfacial force causes each fibril of a dry adhesive to adhere to the substrate in contact? In the particular case of geckos, as the most widely-used and well-studied prototype in fabrication of synthetic dry adhesives (SDAs) [15-18,22], it has been illustrated that the adhesion forces, responsible for the adherence of the hierarchical fibrils of the animal's toe pads to the substrate that the animal is walking on or clinging to, are mainly vdW forces [2,3,5]. From this perspective and considering that vdW interactions are universal (*i.e.*, they exist upon contact of any two surfaces) [74], the adhesion of SDAs in dry conditions has also been studied according to efficiency of dry adhesives in generating effective vdW interactions upon contact [15-18,22].

The presence of vdW interactions upon contact between any two surfaces is natural [74]; even so, it is also known that upon the same contact, electric charges transfer from one

surface to the other, subsequently resulting in formation of an electrostatic interaction between the two surfaces [30,31]. Put otherwise, upon contact of any two materials, similar or dissimilar, electric charges transfer from one surface to the other, while some of the transferred charges eventually separate between surfaces during their detachment from each other [30,31,34,37]. As a matter of fact, separation of electric charges via this so co-called contact electrification (CE) phenomenon (also known as "surface charging") leads to development of a net negative charge on one surface and a net positive charge on the other, resulting in the development of an electric field between surfaces and consequently, an electrostatic interaction between them [32,33]. CE usually happens – more or less – upon contact of any two solid materials [30,31]; thus, its occurrence at any interface, including that of a dry adhesive, cannot be simply ruled out.

Not only can CE have an impact on the interfacial behavior of dry adhesives, but also its role can be very crucial. The possible effectiveness of CE and in turn, of the generated electrostatic interactions on adhesive properties of dry adhesives, is mostly because of the achievable magnitude of the electrostatic force arising from CE; that is, electrostatic forces caused by surface charging can be very large [29,32,33,38,97], much larger than vdW forces which are traditionally considered as the dominant interfacial forces at contact of dry adhesives. It is worthwhile mentioning that the work of adhesion (*i.e.*, adhesion force per unit area) stemming from CE-driven electrostatic interactions can even match the fracture energies of ionic-covalent materials [32,33]. From this perspective, it can be concluded that if surface charging at the surface of a dry adhesive happens in an effective manner, the

adhesive properties of the dry adhesive would be completely different from what has been conventionally considered according to the exclusive dominance of vdW interactions at the contact zone.

2.3.1 van der Waals interactions

The adhesive properties of geckos and SDAs are traditionally studied based on their efficiency in generating vdW interactions with the substrate they come into contact with [15-18,22]. These interactions are essentially arising from the shift in the orbital electrons of atoms and/or molecules to one side and, in turn, the change in their dipole moments. The electrostatic interactions between the generated dipoles, which can be either permanent, induced, or instantaneous, are essentially what are being called vdW interactions [74]. What mainly matters in case of a dry adhesive is the magnitude of the non-retarded vdW interaction force between the dry adhesive and the substrate which is brought into contact with that. To estimate the magnitude of the vdW interaction force, the modified Hamaker method as well as some particular contact mechanics theories can be employed, which will be discussed in the following subsections.

2.3.1.1 Hamaker method

Hamaker reported that summing up the interactions between all atom/molecule pairs of two macroscopic solid bodies in intimate contact allows one to estimate the magnitude of the vdW interaction energy between the two objects [98]. This assumption led to the

development of what is being called the "Hamaker method" where the magnitude of the vdW interaction force between two smooth solid bodies can be theoretically determined with a reasonable degree of accuracy [74]. However, the precision of the original Hamaker method in estimating the vdW force between two objects separated by another medium was an issue which had to be resolved. In this regard, efforts by Lifshitz [99] in later years helped developing the Hamaker theory by modifying what was originally called the "Hamaker constant" [74]. Doing so, a significantly more accurate form of the Hamaker method was developed, which is currently being applied as a conventional method in estimating the vdW force generated between a solid substrate, such as a dry adhesive, and an object in intimate contact.

According to the Hamaker method and in the general case of two smooth solid spheres (named phase 1 and phase 2 with radius of curvature R_1 and R_2, respectively) at a separation distance (D) (see Figure 2.3), by summing up the interactions between all atom pairs of the two bodies, the generated vdW interaction energy (V_{vdW}) can be calculated by [74]

$$V_{vdW} = -\frac{AR}{6D}$$

Equation 2.3

where A is the material-dependent Hamaker constant between phases 1 and 2, while R is the radius of the curvature of the interface ($1/R = 1/R_1 + 1/R_2$). In the Hamaker approach, the corresponding constant, A, can be estimated by [98]

$$A = \pi^2 C \rho_1 \rho_2$$

Equation 2.4

where C is the coefficient in the atom-atom pair potential, while ρ_1 and ρ_2 are the number of atoms per unit volume in phase 1 and phase 2, respectively.

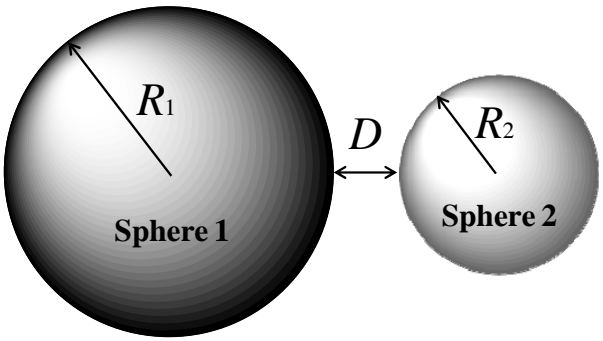

Figure 2.3. Two smooth elastic spheres with radius R_1 and R_2 at separation distance (D). The adhesion force developed between the spheres via vdW interactions can be theoretically estimated by the Hamaker method.

Even though the Hamaker method was practically accurate, eliminating the influence of the adjacent atoms on the interaction between any pair of atoms in the model led to some miscalculations in the magnitude of the vdW interaction energy, particularly when a medium other than vacuum was separating the two objects [74]. In this regard and based on Lifshitz's study where multi-body interactions were considered in the presence of a continuous separating medium [99], another form for the Hamaker constant (A_{132}) between phase 1 and phase 2, interacting across medium 3, was arrived at. The modified Hamaker constant can be determined from [74]

$$A_{132} \approx \frac{3}{4}kT\left(\frac{\varepsilon_1-\varepsilon_3}{\varepsilon_1+\varepsilon_3}\right)\left(\frac{\varepsilon_2-\varepsilon_3}{\varepsilon_2+\varepsilon_3}\right) + \frac{3h\nu_e}{8\sqrt{2}}\frac{(n_1^2-n_3^2)(n_2^2-n_3^2)}{(n_1^2+n_3^2)^{\frac{1}{2}}(n_2^2+n_3^2)^{\frac{1}{2}}\{(n_1^2+n_3^2)^{\frac{1}{2}}+(n_2^2+n_3^2)^{\frac{1}{2}}\}}$$

Equation 2.5

where k is Boltzmann's constant, T is the temperature, h is Planck's constant, and ν_e is the electron absorption frequency, which is typically around 3×10^{15} 1/s [74]. Here, ε_1, ε_2, and ε_3 are the corresponding dielectric constants of sphere 1, sphere 2, and medium 3, respectively, while n_1, n_2, and n_3 are the refractive indices of sphere 1, sphere 2, and medium 3, respectively. As a matter of fact, calculating the modified Hamaker constant – using Equation 2.5 – by knowing the electrical and optical properties of the materials in contact is very easy; doing so, practically accurate Hamaker constants can be obtained [74].

Using the modified form of the Hamaker constant (hereafter just called "Hamaker constant"), the vdW-driven force (F_{vdW}) interacting between phase 1 and phase 2 across medium 3 of known electrical and optical properties at the separation distance D (see Figure 2.3) can be calculated by

$$F_{vdW} = -\frac{A_{132}R}{6D^2}$$

Equation 2.6

In general, negative values obtained for F_{vdW} from Equation 2.6 demonstrate (by convention) the presence of attractive vdW interactions between the two objects, whereas positive values show the opposite. In fact, what signifies whether the vdW force between two solid objects is attractive or repulsive is essentially the value of the Hamaker constant. That is, in cases where the Hamaker constant is positive, the vdW interaction force is attractive and vice versa

[74,100]. As a matter of fact, systems in which vdW forces are repulsive are very rare; in general, for two particular objects, when the dielectric function of the separating medium falls between those of the solid bodies, then the vdW interactions will be repulsive. For instance, upon contact of α-alumina with Teflon AF through cyclohexane, where the dielectric constant of the separating medium ($\varepsilon_{cyclohexane}$ = 2.03) is between those of the α-alumina ($\varepsilon_{\alpha\text{-}alumina}$ = 10.1) and Teflon AF ($\varepsilon_{Teflon\ AF}$ = 1.93), *i.e.*, $\varepsilon_{Teflon\ AF} < \varepsilon_{cyclohexane} < \varepsilon_{\alpha\text{-}alumina}$, the corresponding Hamaker constant is negative [100]. Negative values of the Hamaker constant indicate the presence of repulsive vdW interactions between Teflon AF and α-alumina in cyclohexane [100]. Even so, upon contact of the same materials in air ($\varepsilon_{air} \approx 1$), where $\varepsilon_{air} < \varepsilon_{Teflon\ AF} < \varepsilon_{\alpha\text{-}alumina}$, the vdW interactions are attractive [100]. In this perspective, vdW interactions between two objects via air, as typically happens in tribological tests on dry adhesives, are normally attractive while the magnitude of the vdW force interacting between them can practically be estimated by using the modified Hamaker method [74].

2.3.1.2 JKR model

Besides the modified Hamaker method, the magnitude of the vdW interaction force between two macroscopic solid objects can also be determined by contact mechanics models. Among various models (such as Hertzian [101], Derjaguin-Muller-Toporov (DMT) [102], and Maugis [103] models), the Johnson-Kendall-Roberts (JKR) [104] model is indeed the most well-known and widely-applied theory for analyzing the vdW interactions of highly adhesive

and elastic systems (such as dry adhesives). More specifically, the JKR method considers only the presence of the short-range attractive forces within the area of contact between two elastic bodies; doing so, JKR can practically estimate the effect of vdW interactions on the shape of the contact zone as well as on the magnitude of the mechanical force (*i.e.*, pull-off force) required to separate the two contacting objects [104]. In this perspective, JKR model has been widely used to investigate the adhesion performance of most dry adhesives which are conventionally evaluated based on their effectiveness in generating vdW interactions upon contact [15-18,22].

The JKR model, like other well-known contact mechanics theories (*e.g.*, DMT and Maugis models), is essentially a modified form of the Hertzian model. The classical Hertzian model was originally developed to predict the size and shape of contact between two smooth and elastic but non-adhering bodies [101]. More specifically, the Hertzian theory considers the deformation of interface in the absence of surface forces and only takes the effect of an external applied load into consideration. Assuming that no surface forces exist upon contact of two smooth elastic spheres of radius R_1 and R_2, Hertz reported that the radius of the contact area (a_0) under the applied load of P_0 (see Figure 2.4) can be estimated by [101]

$$a_0^3 = \frac{R}{K} P_0$$

Equation 2.7

where R is the radius of the curvature of the interface ($1/R = 1/R_1 + 1/R_2$) and $K = 4/(3\pi\ (k_1 + k_2))$; k_1 and k_2 are the elastic constants of the sphere 1 and sphere 2, respectively. The elastic constants (k_1 and k_2) are defined as [101]

$$k_1 = \frac{1 - \nu_1^2}{\pi E_1}$$

Equation 2.8

and

$$k_2 = \frac{1 - \nu_2^2}{\pi E_2}$$

Equation 2.9

where ν_1 and ν_2 are the Poisson ratios of surfaces 1 and 2, respectively, and E_1 and E_2 are the corresponding values of Young's modulus.

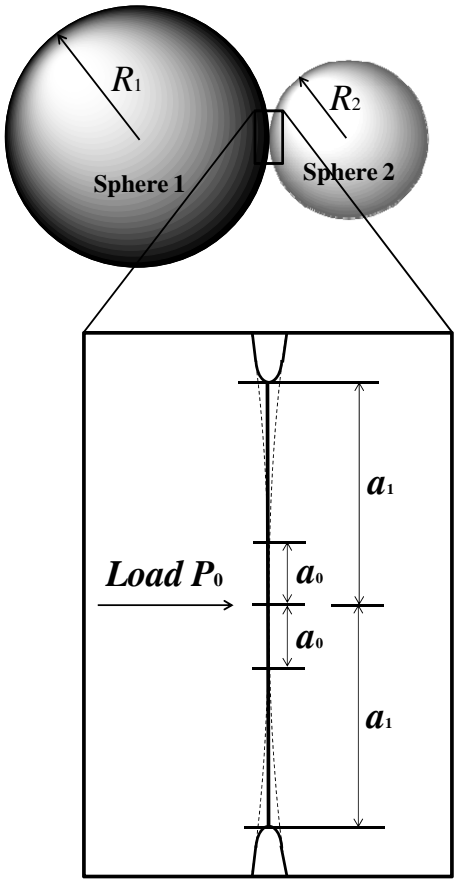

Figure 2.4. Two smooth elastic spheres with radius of curvature R_1 and R_2 in contact under load P_0. Contact radius a_0 is predicted by the Hertzian model considering that there is no interfacial interactions between the two spheres. Taking the effect of attractive interfacial forces into consideration, JKR model determines that the radius of contact would be a_1, where $a_1 > a_0$.

As illustrated, the Hertzian model solely takes the mechanical and geometrical properties of the surface into consideration in order to determine the properties of the contact. In this respect, it can be stated that the Hertzian model is essentially suitable for analyzing "non-adhering" contacts. However, over time and upon contact of different materials (*e.g.*, rubber and glass spheres), it was observed that due to the presence of surface forces, the actual apparent area of contact was larger than that predicted by the Hertzian theory, whereas finite contact area values even under zero load were detected [104]. Despite the wide application and success of the well-known Hertzian model, these observations urged the development of an alternative model which could also take into consideration the impact of the interfacial interactions. In this connection, the JKR theory was developed [104]. Considering only the contribution of short-range vdW forces within the area of contact while assuming infinite elastic stresses at the edge of the contact region, the developed JKR model has received wide acceptance amongst those (including dry adhesive scientists) who were looking for the contribution of vdW interactions at the interface. Having described the presence of short-range vdW interactions (within the contact zone), Johnson *et al.* [104] showed that the actual load (P_1) and the equilibrium contact radius (a_1) between two smooth elastic spheres of radius R_1 and R_2 is larger than those estimated by the non-adhering Hertzian model (see Figure 2.4).

The JKR theory, by applying a balance between the stored elastic energy, the mechanical energy of the applied load, and the surface energy, demonstrated that the actual load P_1 is different from the applied load P_0 considered by Hertz [101], defined as [104]

$$P_1 = P_0 + 3\gamma\pi R + \sqrt{6\gamma\pi R P_0 + (3\gamma\pi R)^2}$$

Equation 2.10

where γ is the interface energy or surface energy change per unit area for two perfectly smooth surfaces. The magnitude of the interface energy, which is basically dictated by the vdW interactions, can practically be determined by $\gamma = \gamma_1 + \gamma_2 - \gamma_{12}$, where γ_1 and γ_2 are the surface energies of phase 1 and phase 2, respectively, whereas γ_{12} is the interfacial energy which can be approximated by $\gamma_{12} = (\gamma_1.\gamma_2)^{1/2}$ [74]. Having the actual load from Equation 2.10, the JKR model defines the actual contact radius (a_1) (see Figure 2.4) as [104]

$$a_1^3 = \frac{R}{K}(P_0 + 3\gamma\pi R + \sqrt{6\gamma\pi R P_0 + (3\gamma\pi R)^2})$$

Equation 2.11

As a matter of fact, by assuming that there is no attractive force between phase 1 and phase 2 (*i.e.*, $\gamma = 0$), P_1 would be equal to P_0 (see Equation 2.10), whereas the JKR equation for the surface area (*i.e.*, Equation 2.11) reverts to the particular Hertzian model equation (Equation 2.7), which was developed for non-adhering systems. However, considering the presence of adhesive forces in the area of contact by the JKR model, it can be seen that even under zero applied load ($P_0 = 0$), the surfaces do not detach and there would be a finite contact area between them (*i.e.*, $a_1 \neq 0$). According to another point of view, upon detaching the substrates, the applied load, P_0, goes down to zero and from there, it becomes negative. The minimum of the applied – negative – force obtained at the very last stage of the detachment of the two substrates is in fact what is being called "pull-off force", normally used to evaluate the adhesive ability of a surface in contact.

To obtain the magnitude of the pull-off force required to detach the two spheres in contact, JKR assumed that the equation for the contact area (Equation 2.11) is valid only when $6\gamma\pi RP_0 \leq (3\gamma\pi R)^2$ and accordingly, $P_0 \geq -1.5\gamma\pi R$. In this respect, the JKR model indicates that the vdW-driven pull-off force (F_{vdW}), as the minimum applied negative force upon detachment of the substrates, can be simply estimated by [104]

$$F_{vdW} = -1.5\,\pi R\gamma$$

Equation 2.12

Here, same as with the Hamaker method, negative values of F_{vdW} obtained by Equation 2.12 correspond to attractive interaction forces.

The magnitude of the adhesion force developed by vdW forces between two smooth substrates can be estimated using Equation 2.12. However, in contact of non-atomically smooth substrates (as most real surfaces against which dry adhesives are typically tested), some modifications to the JKR model need to be applied. In particular, in contact of such an elastic solid surface as a dry adhesive with a rough substrate, the properties of contact are largely affected by the – repulsive – elastic energies associated with bending of the solid to conform to the roughness of the substrate [80,105]. Put otherwise, when a dry adhesive comes into contact with a rough substrate, there is an elastic energy required to bend the elastic surface to bring it into an intimate molecular contact with the substrate. The energy required in this regard essentially acts in competition with the achievable adhesion. Therefore, instead of the interface energy (γ) used in Equation 2.12, the effective interfacial energy per unit area (γ_{eff}) must be taken into account. Assuming a_1 as the nominal contact area and a as the real contact area, γ_{eff} can be therefore estimated by [105]

$$\gamma_{eff} = \frac{\gamma a - U_{el}}{a_1}$$

Equation 2.13

where U_{el} is the elastic – bending – energy necessary to make atomic contact at the interface. In fact, what Equation 2.13 essentially implies is that, in analysis of contact of a fibrillar adhesive with a not perfectly smooth surface using the JKR model, what needs to be looked after is the actual area of contact (a), but not the apparent area of contact (a_1) [105].

In general, the JKR model, same as the modified Hamaker method, can be applied to estimate the adhesion forces coming from vdW interactions between two solid objects. For the particular contact of a SDA with a substrate, both JKR and Hamaker methods have been widely used to determine the magnitude of the force required to separate the dry adhesive from the substrate (*i.e.*, adhesion force). Despite their advantages and disadvantages, what both models share conceptually is the fact that the magnitude of the vdW interaction force between two specific bodies is independent of the area of contact, while it is only affected by the geometry of the interface in addition to the nature of the materials involved.

2.3.2 Contact electrification and electrostatic interactions

Adhesive performance of geckos and also SDAs is conventionally evaluated based on their ability to generate efficient vdW interactions, whereas the effect of surface charging on their adhesive properties has received little attention in the literature [29,38,97]. Even so, it is known that upon contact of any two – dissimilar or, in certain cases, similar – materials,

electric charges separate within the contact zone [30,31,34,37,106], causing the formation of electrostatic interactions between the two substrates. In fact, in the presence of electrostatic interactions, the magnitude of the adhesion force required to separate the two touching substrates would be significantly different from that obtained in the absence of CE [32,33,107]. However, in studies on adhesive properties of dry adhesives, the effect of CE has been frequently ignored, perhaps because of poor understanding of the CE over the surface of insulating materials [30,31,34,37,106]. Another reason might be the lack of access to an appropriate technique readily capable of estimating the amount of the charge separation upon contact of dry adhesives in an accurate and practical manner.

In this respect, the principles of the CE phenomenon and its causes and limitations will be highlighted in the following subsection. An established theoretical method which can be employed to model the electrostatic adhesion of the macroscopic interfaces charged via CE will be introduced next. Then, the factors which can affect CE over the surface of insulators will be briefly discussed. Finally, the experimental techniques at hand capable of simultaneous measurement of the surface forces and surface electric charges developed upon contact will be presented and their applicability in analyzing the adhesion behavior of dry adhesives will be demonstrated afterwards.

2.3.2.1 Contact electrification

Lowell and Rose-Innes [31] in one of the most comprehensive review papers about CE have defined this incident as: "If two materials are brought into contact and then separated, they are found to be charged; this is the phenomenon of 'contact electrification'" [31]. The brief yet broad description of CE by Lowell and Rose-Innes [31] simply implies that CE is universal and therefore, can happen in contact of any two materials. In a broader perspective, CE may occur in three distinct types of contact: conductor–conductor, conductor–insulator, and insulator–insulator. In the current discussion, we are mainly focusing on those types of contact where an insulating material is involved, considering that fibrillar feature of gecko foot pads and also polymeric SDAs are mostly made up of such insulating materials as β-keratin and non-conductive polymers, respectively.

The history of CE over insulators is dated back to Thales of Miletus and his famous experiment of charging a piece of amber by rubbing against wool [30,31,34,37,106]. Despite its long history, the efforts to reveal the fundamentals and mechanisms of CE, specifically in case of insulators, are still continuing. The imprecise theoretical understanding of CE at insulating interfaces is mostly because of the vague definition of electron states for insulators and, before and beyond that, a lack of a general agreement on the mechanism of charge separation through CE for these materials [30,31,34,37,106,108-110].

Despite metals where electron states are simply defined based on their Fermi levels, a similar all-inclusive description for insulators has not been achieved yet [30,31,34,37,106,108-110]. Besides, it has been claimed that mechanisms other than transfer of electron, such as ion and

material transfer, might also be involved in separation of charges at insulating interfaces [30,31,34,37,106,108-110]. In fact, there is an ongoing controversy regarding the mechanism of charge separation across the interface where an insulator is involved. However, discussion about this topic is beyond the context of the current thesis. Herein, the CE phenomenon over insulators will be discussed and analyzed regardless of the electric charge transfer mechanism; what we are mainly concerned with here is only the idea that via CE, electric charges transfer across the interface, eventually leading to formation of electrostatic interactions between the contacted surfaces. For more details about the possible charge separation mechanism at insulating interfaces, the papers by McCarty and Whitesides [37] and Diaz and Guay [108] as well as that by Lowell and Rose-Innes [31] can be consulted.

Even though the understanding about surface charging at the surface of insulators is relatively superficial, it has been illustrated that insulating materials are excellent candidates for promoting adhesion via CE-driven electrostatic interactions [29,32,33,38,97,107]. More specifically, insulators are prone to get highly charged at their surface as surface charges via CE cannot efficiently transfer into their matrix [111,112], leading to accumulation of electric charges at the surface; by trapping excessive amounts of electric charges at the surface, insulators can generate enhanced electrostatic interactions through CE. To this day, promoting adhesion through surface charging of insulators has been successfully applied in various technologies as photocopying and laser printing [106], which essentially deal with charging of micron-sized particles. Even so, reports which have quantitatively discussed the magnitude of the electrostatic interaction force obtainable via CE over macroscopic-sized

insulators are rare [32,33,107]. The pioneering study in this regard is indeed the experiment carried out by Horn and Smith [32], whereby using the experimental technique developed by Smith [113] a year before, the adhesion force due to electrostatic interactions between two insulators (silica and mica; radius of curvature (R) ≈ 20 mm) charged via CE was quantified. The most striking finding of Horn and Smith's study was indeed the large magnitude of the work of adhesion which was obtained through CE-driven electrostatic interactions upon separation of silica and mica thin films from each other [32]. In particular, works of adhesion as large as 6.6–8.8 J/m^2 were detected, which are even comparable to the fracture energies of the contacting materials (8.7 J/m^2 and 2.0 J/m^2 for silica and mica, respectively) [32]. A year later, Horn *et al.* [33] performed a similar experiment – using the same experimental method – but on two identical insulating substrates (silica), where one was coated with a single chemisorbed monolayer of an amino-silane. In their paper, Horn *et al.* [33] also reported a surprisingly large work of adhesion (3.3 J/m^2) between the treated and untreated silica substrates [33].

Although the magnitude of the adhesion force obtainable via CE at the surface of macroscopic objects has not been reported frequently (perhaps due to difficulty of its characterization), it is expected that enhanced electrostatic interactions be achieved through CE at the interface where an insulator is involved. But, at the same time, it should be noted that any system with the intention of developing effective CE and subsequently, generating strong electrostatic interactions, requires specific material and geometrical properties; these specific requirements will be discussed shortly.

2.3.2.2 Simple capacitor model

Before introducing the factors which allow the occurrence of an effective surface charging at an insulator surface, a relatively reliable model describing the properties of the interfaces charged via CE needs to be demonstrated. In this regard, the common contact mechanics models, such as Hertzian, JKR, DMT, or Maugis cannot be helpful as they do not consider the occurrence of surface charging [107]. In addition, the trials to develop a reliable theoretical model capable of predicting the electrostatic adhesion properties of insulators charged via CE, which are mostly done for small (micron-sized) particles [114-117], are not that useful for the particular case of macroscopic-sized objects, such as dry adhesives. As a matter of fact, unpredictability of the magnitude of CE over the surface of insulators, as previously mentioned, is the main reason which has limited the accomplishments in this vein. Despite the restricted success and applicability of studies conducted so far, the so-called "simple capacitor model", which describes the electrostatic interaction force between two flat parallel sheets of a regular capacitor, is perhaps the most dependable method available for studying the CE-driven electrostatic interactions of macroscopic objects of specific geometries [29,32,33,38,107].

To look into the details of the simple capacitor model, the general case of two perfectly smooth spherical objects (named again phase 1 and phase 2 with radius of curvatures R_1 and R_2, respectively) in medium 3 at separation distance (D) needs to be considered (see Figure

2.5.A). In this model, it is assumed that the surfaces of both spheres are originally neutral. However, as illustrated in Figure 2.5.B, the CE principle implies that the spheres get subsequently charged once they are brought into contact by applying a load P_2. In the next step and during the separation of the spheres, the charges which are transferred during contact would subsequently separate between the two spheres throughout the interfacial fracture, leading to accumulation of a net negative charge over one surface and a net positive charge over the other. The charges separated upon detachment would ultimately build up an electric field between the two spheres and as a result, an electrostatic interaction force between them will be developed (see Figure 2.5.C).

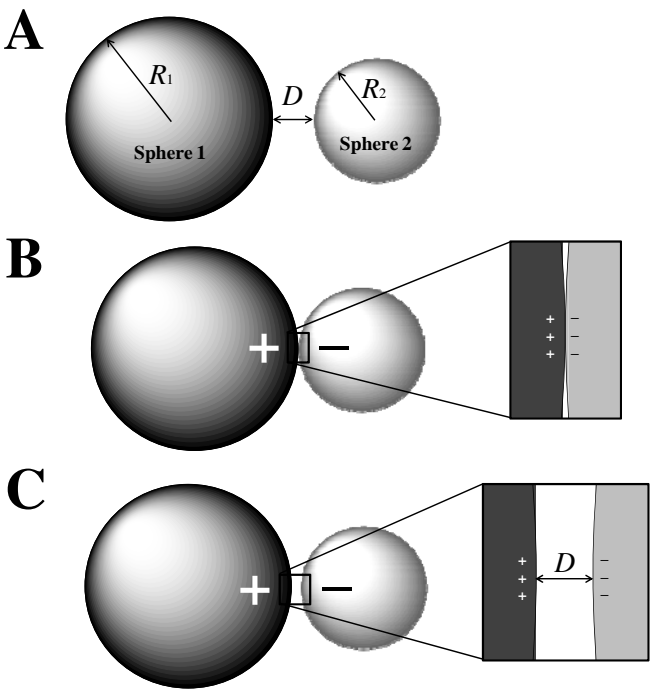

Figure 2.5. (A) Two spheres with radius of curvature R_1 and R_2 at separation distance (D). The surfaces of both spheres are electrically neutral. (B) The spheres are brought into contact by applying load P_2. CE implies that upon contact between the spheres, electric charges spontaneously transfer across the interface. (C) Electric charges transferred upon contact would separate during interfacial fracture when the spheres are detached from each other. Depending on the materials and conditions of experiment, one of the surfaces would get a net negative charge, whereas the other becomes positively charged, leading to formation of an electrostatic interaction between the two substrates.

Here, in order to estimate the magnitude of the generated electrostatic interaction force between the two spheres, the simple capacitor model requires that the interface between the two objects is considered as that between two parallel plates. In fact, this simplifying assumption is applicable only when the separation distance (D) is much smaller than the radius of curvature (R) of the interface (where $1/R = 1/R_1+1/R_2$) and the diameter of the contact area, which is reasonably the case in contact of macroscopic objects under low pressures (see Figure 2.5.C) [29,32]. Being so, the geometry of the system can resemble that of a parallel plate capacitor and, accordingly the electrostatic interaction force (F_{elc}) developed between the two spheres can simply be approximated by [97]

$$F_{elc} = -\frac{a\sigma^2}{2\varepsilon_0\varepsilon_r}$$

Equation 2.14

where σ is the surface charge density (assumed equal on both surfaces), a is the real area of contact (equal to the nominal area of contact (a_1) for perfectly smooth surfaces) under load P_2, ε_0 is the permittivity of free space, and ε_r is the relative permittivity of the separating medium.

Before applying Equation 2.14 to the analysis of CE at insulating interfaces, a few points need to be clarified at this stage. First, it should be noted that Equation 2.14 is approximate in the sense that it does not consider the surface deformations upon contact while equal charge densities are considered over the surfaces [32]. Besides, Equation 2.14 does not reflect the effect of the separation distance on the developed electrostatic force, which is reasonably

correct for small distances [107]. However, regardless of these assumptions, what the developed simple capacitor model clearly demonstrates is that, despite vdW interactions, the magnitude of the electrostatic force developed via CE is directly proportional to the actual area of contact. In addition, the simple capacitor model signifies that the electrostatic interaction force generated via CE is directly related to the power of two of the surface charge density (σ). That is, the higher the surface charge density is, the larger the electrostatic interaction forces obtained through surface charging would be.

In this regard, it can be concluded that in the case of dry adhesives, those capable of generating an enhanced actual area of contact while trapping a large amount of electric charges at their surface upon contact can promote adhesion through CE-driven electrostatic interactions. It is worthwhile recalling here that both prerequisites (*i.e.*, developing a large surface area and surface charge trapping) are the properties that all polymeric dry adhesive, more or less, have in common. Factors which can positively or negatively affect the magnitude of the surface charges that can be developed through CE over insulating materials – with the main focus on dry adhesives – will be briefly discussed in the following subsection.

2.3.2.3 Factors affecting contact electrification over insulators

In order to estimate the magnitude of the electrostatic adhesion obtainable via surface charging over insulators and particularly insulating dry adhesives, the amount of electric

charges which may be developed over their surface upon contact must be determined. Even so, estimating the magnitude of the surface charge density in case of insulators, in general, without doing real experiments, is almost impossible. As a matter of fact, the amount of electric charges coming from surface charging is dependent on many factors such as the nature of the contacting materials, possible partial discharge across the separating gap, applied pressure, surface topography, material strain, humidity, duration of contact, surface contamination, and temperature [30-33,35-37,44,45,47,48,106,118-121]. As the above mentioned factors may contribute irregularly depending on the specific system, predication of the magnitude and, sometimes even the sign of the electric charges that an insulator may gain upon its contact, is essentially not practical.

First and foremost, there is a big uncertainty about the effect of the insulating materials on both the extent of the developed charge and its type (*i.e.*, positive or negative). Although conductors can be sorted for their performance in CE according to their Fermi levels, there is no singular physical property which can be employed in the case of insulators to predict how much and what type of charge they will acquire through surface charging [30,31,37].

This shortcoming with respect to non-conductors can be partly overcome by using the so-called "triboelectric series", which can be applied to foresee the sign of the obtainable charge in CE. Even though not practically applicable in all cases, reliable triboelectric series (a representative of which is demonstrated in Table 2.1) can be employed to predict, in contact

of two particular substrates, which substrate would get the net negative charge and which would acquire the net positive charge [30,31,37,106,118].

Table 2.1. A triboelectric series consisting of only a list of non-metallic materials [122].

+	Glass
More positive	Mica
	Polyamide (Nylon6-6)
	Rock Salt (NaCl)
	Wool
	Fur
	Silica
	Silk
	Poly(vinyl alcohol) (PVA)
	Poly(vinyl acetate) (PVAc)
	Paper
	Cotton
	Wood
	Amber
	Poly(methyl methacrylate) (PMMA)
	Poly(ethylene terephthalate) (Mylar)
	Epoxy resin
	Natural rubber
	Polyacrylonitrile (PAN)
	Poly(bisphenol A carbonate) (Lexan, PC)
	Poly(vinylidene chloride) (Saran)
	Polystyrene (PS)
	Polyethylene (PE)
	Polypropylene (PP)
More negative	Poly(vinyl chloride) (PVC)
−	Polytetrafluoroethylene (Teflon, PTFE)

More specifically, materials closer to the top of a triboelectric series (*e.g.*, glass in Table 2.1) will characteristically develop a net positive charge when they are brought into contact with a material closer to the bottom of the table (*e.g.*, Teflon in Table 2.1), which would normally become negatively charged. These triboelectric series, which are basically empirical measures, cannot enlighten one much on the amount of the charge developing via CE. But, using them to predict the sign of developed charges is common, even without complete

acceptance among all scientists (for instance, controversial results have been reported from different groups for contact of similar pairs of materials [31], but of course, as usual, the reason might have been due to specific factor interactions that were neglected).

Other than the type of the materials involved at an interface, the partial discharge which may happen in cases where the surfaces get highly charged is another important factor that can significantly affect the CE over insulators and therefore, complicates the analysis [30-33,37,106,123]. In particular, if the charge densities developed via CE become high, an electrical breakdown would occur – across the separating gap – upon separation of the two contacted substrates. The electrical breakdown, which may give rise to formation of sparks at the contact zone, is basically the backflow of the electric charges to the original surface [30-33,37,106,123].

Although the charge backflow is hardly a predictable incident, for the cases where electron transfer is dominating the CE, it is reported that when the separating gap between the two surfaces (at a specific pressure) is smaller than the mean free path of the electrons in the separating medium (*e.g.*, ~0.5 μm for air), discharge cannot happen [32]. But, once the separation distance passes this limit, the electric field formed between the two substrates becomes large enough to cause a charge backflow [32,33]; therefore, the system can reduce its increased free energy in this way. As a matter of fact, in a gaseous medium like air, some of the initiatory electrons are amplified by ionizing collisions with the molecules of the separating medium, thus helping the backflow of the charges to the original surface [32].

Regardless of its causes and origin, what the backflow of electric charges primarily affects in the case of dry adhesives is the magnitude of the final charge density at the surface and, in turn, the extent of the adhesion force which can be obtained by them via CE [32,33,107]. More specifically, as partial discharge happens, the magnitude of the achieved surface charge density declines and therefore, the absolute value of the electrostatic force obtainable between the two substrates decreases [32,33].

The next factor which should be considered in the analysis of CE over insulators is the heterogeneous distribution of electric charges over these materials [35,51,106,124]. According to results from recent research on CE of some insulating polymers (*i.e.*, PDMS, PC, and Teflon), it was observed that CE can dramatically be influenced by the nanoscopic structure of the surface [35]. Baytekin *et al.* [35] reported that electric charges developed over an insulating surface via CE were distributed in heterogeneous nanoscopic regions of opposite charges (length scales ≈ 40–400 nm) [35]. Divergent distribution of the surface charges at nano-scale and even micro-scale, which has been reported by other groups [35,51,106,124], basically leads to larger "local charge density" (even 3 orders of magnitude larger) in comparison to what is being normally measured as "net charge density" [35].

At this point of the discussion, it is interesting to mention that the fibrils of polymeric dry adhesives are typically fabricated – or naturally exist – with the same micro/nanoscale periodicity as the charge distributions. Being so, it is expected that each fibril on both natural and synthetic dry adhesives deals with relatively larger surface charge densities in

comparison to what is assumed for a flat substrate. Put otherwise, considering that surface charges will also distribute, more or less, at the same length scales that fibrils of dry adhesives are, it is likely that the magnitude of charges that dry adhesive fibrils deal with upon their contact be larger than what is presumed as the net surface charge density.

The last but not least factor involved in CE of insulators in ambient conditions is humidity. Even though humidity can lead to formation of capillary bridges through condensation of water vapor at the contact zone and, in turn, motivation of capillary forces [13,125], it can also affect the CE at the surface of insulators [36,37,106]. In fact, studies on the effect of humidity on charge transfer upon contact have led to controversial conclusions; while some claimed that presence of water at the contact zone can promote the CE phenomenon, others have reported that water may negatively affect that. Even so, recent results from a careful study carried out by Baytekin *et al.* [36] revealed that CE is not necessarily dependent on the presence of water at the contact zone, while it can be affected by that. In particular, by sustaining a water-free environment in a very controlled manner, their study revealed that CE will happen even in the absence of water; even so, the presence of water can help stabilize the surface charges developed at the contact zone via CE [36].

Other than the aforementioned factors, there are additional ones such as applied pressure, material strain, surface topography, duration of contact, surface contamination, and temperature, which may also influence CE [30-33,35-37,44,45,47,48,106,118-121]. Even though they have also been studied by various groups to date, same as the factors exemplified

in the current discussion, a complete understanding of the effects of these factors on CE at the surface of insulators is also still elusive. The controversy in the science of CE over insulators has certainly held scientists back with respect to an all-inclusive system description, which can be practically used to study and accordingly describe common engineering and scientific systems such as adhesive contacts of natural and synthetic dry adhesives. As a matter of fact, due to the unpredictability of surface charging in the case of insulators, the real value of the electric charge density which may separate in contact of an insulator with another material should necessarily be determined in an experimental manner. Experimental techniques available to measure the magnitude of the surface charge as well as capable of measuring the surface forces in parallel will be introduced in the following subsection.

2.3.2.4 Experimental techniques for analyzing contact electrification

Identification and estimation of surface charges may be performed via various experimental techniques ranging from conventional methods using a Faraday cup/electrometer set to more recent approaches using solution chemistry [31,42]. Measuring the magnitude of surface charges from CE allows one to determine the electrostatic force developed between the contacted substrates. The available experimental methods for measuring the magnitude of surface charges coming from surface charging will be presented herein. In addition, the applicability of surface charge measurement methods for the case of dry adhesives will be discussed in detail.

In general, the experimental methods which can be employed to measure the magnitude of the charge accumulated at a surface via the CE phenomenon naturally fall into two distinct divisions: *in-situ* and *ex-situ* methods. The latter, which may not be very suitable for analysis of CE at the surface of dry adhesives, are those methods where the surface charge density is measured after the separation of the two substrates which were brought into contact earlier. In conventional *ex-situ* methods, the surface charge density of the samples – either touched or rubbed against each other – is measured after their separation from each other by using commercially available sensitive electrometers (*e.g.*, model 6517 from Keithley Instruments Inc.) [31,35,36,44-46]. In these methods, the sample charged via CE is placed inside a classical Faraday cup or simply on a metal sheet connected to an electrometer. Here, the electric charges at the surface of the sample induce the opposite charge on the metal sheet or the Faraday cup wall, while the induced charges are subsequently measured by the electrometer connected to the system.

Despite the simplicity and accuracy of conventional *ex-situ* methods, they might not be quite suitable for estimating the charges developing via CE over dry adhesives. More specifically, *ex-situ* methods, as their name indicates, are only applicable to the cases where the charged sample can be physically transferred – from the charging spot to the surface charge measurement setup – to measure its surface charge density. However, in the case of dry adhesives, transferring the dry adhesive from its original place, where the adhesion or friction tests were carried out, may result in large degree of inaccuracy in measuring the developed

surface charge, as the area of contact in regular indentation and friction tests can be as low as a square millimeter. For instance, in a characteristic adhesion test on a typical dry adhesive with an elastic modulus of 100 kPa and Poisson's ratio of 0.5 (*i.e.*, $R_1 = \infty$, $E_1 = 100$ kPa; $\nu_1 = 0.5$) in contact with a hemispherical glass probe of 1 cm in radius ($R_2 = 1$ cm; $E_2 = 75$ GPa; $\nu_2 = 0.2$) under a moderate preload of 10 mN ($P_0 = 10$ mN), the area of contact is ~0.6 mm^2, according to Equation 2.7. Here, considering that a typical charge density obtained upon contact through CE is 1.0×10^{-4} C/m^2 [31], the geometrical area implies that the sample acquires a charge of approximately 0.6×10^{-10} C at its contact zone. The charge amount of 0.6×10^{-10} C is extremely small and can even be generated from the touch of tweezers used to transfer the sample. Thus, in the case of SDAs, measuring the surface charge after conducting regular adhesion or friction tests, using the current conventional *ex-situ* methods, may involve a large degree of inaccuracy.

Aside from the conventional *ex-situ* methods mentioned, there is another type of *ex-situ* method which has recently been developed by Liu and Bard [42]. In their study, Liu and Bard characterized and quantified the electrons accumulated over Teflon after rubbing that with various materials including glass, Lucite (PMMA), metal, and Nylon. In their method, the charged Teflon samples were subsequently immersed in different solutions such as a $CuSO_4$ aqueous solution. In the particular case of the $CuSO_4$ solution, for instance, the electrons which were separated upon contact reduced the Cu^{2+} ions into pure Cu according to $Cu^{2+} + 2\bar{e} \rightarrow Cu$ [42]. The pure copper instantaneously deposited at the sample surface. The presence of the copper on the sample was characterized by energy-dispersive X-ray (EDX)

spectroscopy, whereas its amount was tracked by monitoring the changes in optical absorbance of Cu^{2+} in the original $CuSO_4$ solution before and after immersing the Teflon samples. The results obtained by optical absorbance tests were further confirmed by dissolving the deposited copper in concentrated nitric acid. The concentration of the dissolved copper in the acid was subsequently determined using the optical absorbance of Cu^{2+} in the acid [42]. Knowing the amount of copper that was deposited on the sample and considering that the deposited copper was coming from $Cu^{2+} + 2\bar{e} \rightarrow Cu$, Liu and Bard succeeded to determine the amount of electric charges (*i.e.*, electrons) that were developed over Teflon via surface charging [42].

Even though the original idea of Liu and Bard [42,43,50] regarding the chemical reactions via transfer of electrons was later challenged by Baytekin *et al.* [45], the applicability of this method to measure surface charges has not been disputed. However, it should be noted that the sensitivity of the reported chemical *ex-situ* method is even lower than that of the conventional *ex-situ* methods, which limits its application in analysis of CE over SDAs. To be more specific, the developed chemical-based *ex-situ* methods require the immersion of multiple samples (up to ~40) of a large surface area (1–3 cm^2 each) into solutions [29,42,43,45,50]. However, since the areas of contact in regular tribological tests are normally very small (maybe less than a square millimeter, as described earlier), it can be seen that the chemical-based *ex-situ* methods might not be a good option for measuring surface charges developing over dry adhesives through CE.

The difficulty in measuring the surface charge in adhesion tests by available *ex-situ* techniques can be overcome with what has been called *in-situ* methods. *In-situ* methods, preferable yet often tedious in their current form, are those which can simultaneously measure the magnitude of surface charges and interfacial interaction forces. The method developed by Smith [113] and used later by Horn and Smith [32] and Horn *et al.* [33] is perhaps the best, if not the only reliable, of *in-situ* methods.

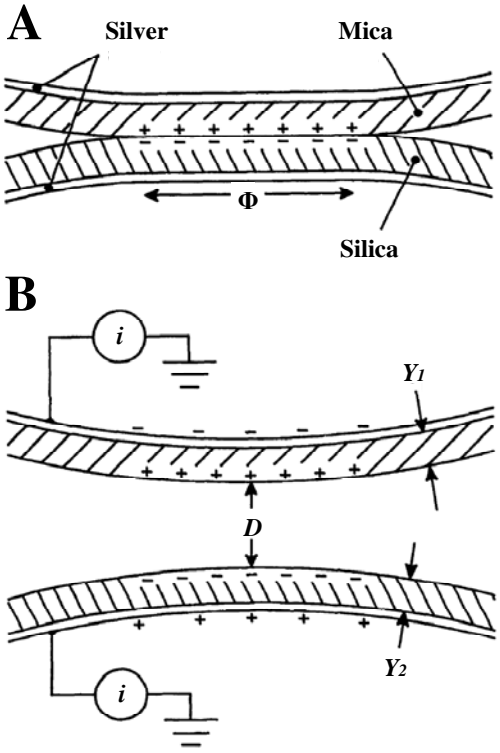

Figure 2.6. Schematic of the *in-situ* system employed by Horn and Smith [32] to simultaneously measure the surface charge densities and interfacial interaction forces upon contact between mica and silica thin films (thickness = Y_1 and Y_2, respectively). Backs of both thin films were coated with a thin layer of silver. The contact diameter (Φ) was typically 100 μm while the radius of curvature of the contact interface was ~20 mm. (A) Upon contact between the thin films, silica obtained a net negative charge, whereas mica became positively charged. (B) The charges transferred through contact, eventually separated upon detachment of the thin films from each other. The image charges on the backing silver layer (induced by the front surfaces) were subsequently measured by integrating the current *i* which was flowing to each grounded electrode as the solids were separated to the separation distance *D* [122].

In experiments by Horn and Smith [32], they mounted two near-atomic smooth thin films of silica and mica on two crossed cylinders (~16.3 and 21.3 mm in radius, respectively) with their cylindrical axes at right angles (see Figure 2.6). To measure the separation distance as well as the force existing between the two substrates, the cylinders were mounted on a surface force apparatus (SFA). As a matter of fact, by employing a SFA to perform tribological tests, the magnitude of the total interfacial force existing between two solid objects can be determined with a large degree of accuracy. However, to determine the sign and magnitude of the surface charges developed upon contact, thin layers of silver were originally coated at the back of the silica and mica thin films. The charges developed upon contact of silica and mica consequently induced the image charge in the backing silver layers, which were simultaneously measured by electrometers connected to the system [32].

The correlation between the electrostatic interaction force (F_{elc}) developed via CE by the charges separated and the surface charge density (σ) at the separation distance (D) was accordingly analyzed by the modified simple capacitor model as [32]

$$F_{elc} = -\frac{a\sigma^2}{2\varepsilon_0}\left(\frac{B}{B+D}\right)^2$$

Equation 2.15

where a is the (real) area of contact, ε_0 is the permittivity of free space, and $B \equiv Y_1/K_1+Y_2/K_2$; Y_1, Y_2 and K_1, K_2 are the thickness and relative dielectric constants of the two substrates, respectively. Using Equation 2.15, Horn and Smith constructed a plot (Figure 2.7) showing the effect of surface charge on the developed electrostatic adhesion strength (*i.e.*, adhesion force per unit area), as the two substrates were separated from each other [32].

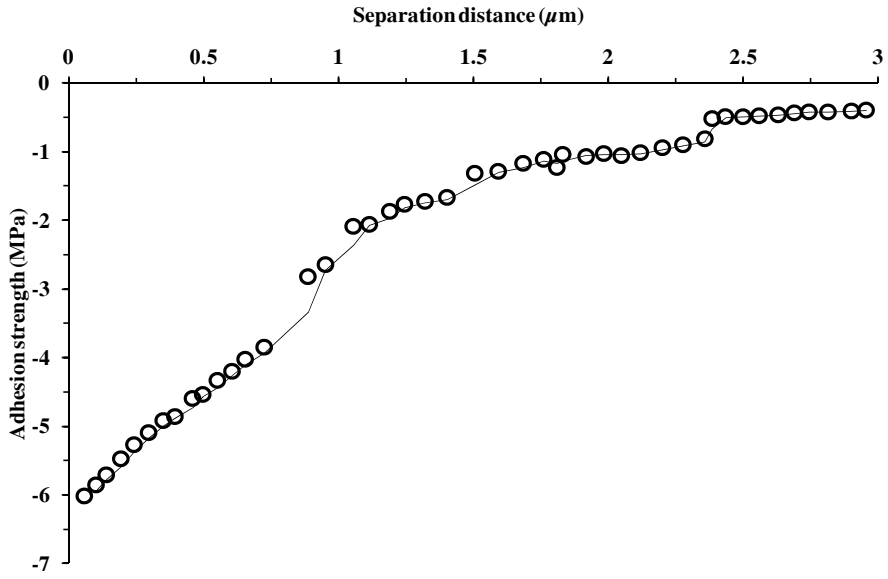

Figure 2.7. The electrostatic force per unit surface area (*i.e.*, adhesion strength) vs. separation distance measured upon detachment of mica and silica thin films which were charged via CE. Negative values correspond to attraction [122].

In fact, the developed *in-situ* method by Smith [113] has been successfully employed in different studies on simultaneous measurement of interfacial forces as well as the CE-developed electric charges at the contact of different sets of materials [32,33]. Even so, application of the current *in-situ* method in case of dry adhesives requires some modifications to the system, as a fibrillar dry adhesive cannot be made as a thin film (as the films shown in Figure 2.6). More specifically, the *in-situ* method can still be applied for a contact of a substrate with a dry adhesive if the substrate is made as a thin film, similar to the thin films of Figure 2.6; doing so, the charges developed on the surface of the substrate upon its contact with the dry adhesive can be measured. Then, considering the reasonable approximation that the amount of charges the dry adhesive obtains via contact (*e.g.*, +10 C) is the same but opposite in sign than the charges developed over the substrate (*i.e.*, –10 C)

[32,45], the amount of charge developed over the dry adhesive after contact (and by some modifications, even during contact) can be determined.

2.3.3 Comparison between van der Waals and electrostatic interactions

The contribution of vdW interactions in interfacial forces at a contact between two macroscopic objects, specifically those at intimate contact, is indisputable [74]. Besides, it is known that in the same contact, electric charges separate across the contact interface, helping the formation of electrostatic interactions at the contact zone [30,31,34,37,106]. However, finding the exact share of each of vdW and electrostatic interactions in the net interfacial force forming between two macroscopic solid objects is not simple. With respect to this, the general properties of vdW interactions, including the effective range and strength plus material and load dependency, will be compared herein with those of electrostatic interactions, in an effort to shed more light on their possible input in the total obtainable interfacial force at macroscopic interfaces.

In a comparison between vdW and electrostatic interactions, at first one should remember that these two types of interfacial forces are essentially similar in their nature. That is, electrostatic interactions are basically attractive or repulsive interactions between such permanent charges as ions or electrons, while vdW interactions are the same interactions but between the atomic/molecular dipoles which naturally exist – or may be induced – in materials. Even though similar in nature, vdW and electrostatic forces also have several

significant dissimilarities in the origin of their formation and also their contribution in the ultimate interfacial force between two substrates in contact.

At an interface between any two contacted surfaces, the permanent, induced, or instantaneous dipoles close to the interface interact with each other via electrostatic interactions, resulting in attractive or repulsive forces of the so-called vdW type between the two substrates. Since the atomic and/or molecular dipoles naturally exist while they can also be induced even in such totally neutral atoms as those of helium, vdW interactions are always present at the contact between any two surfaces [74]. But, despite these vdW interactions, the development of electrostatic interactions between two electrically neutral surfaces is impossible unless electric charges – in the form of electrons, ions, and/or pieces of charged materials – transfer from one surface to the other. As a matter of fact, charge transfer happens as soon as two surfaces are brought into contact, whereas the magnitude of the transferred charges is dependent on many distinct factors, such as those discussed in subsection 2.3.2.3. But, as part or all of the electric charges which are transferred upon contact eventually separate during detachment of the two touched surfaces, an electric field at the contact zone forms and as a result, electrostatic interactions between the two substrates will develop [31,32]. Therefore, it can be stated that formation of electrostatic interactions at a surface of an electrically neutral substrate, such as a dry adhesive, requires that electric charges are formed at the surface through surface charging. However, in contrast to electrostatic interactions, vdW forces are naturally present at an interface between any two surfaces, no matter whether electrically neutral or charged.

Indeed, one of the main aspects in the contribution of vdW interactions is their predominance; they exist in contact of any two surfaces. In fact, what does not allow vdW interactions to cause the adherence of everything that exists in the world together is one of their inherent properties: vdW interactions are relatively short-range. More specifically, vdW interactions between atoms and molecules of two contacted surfaces require that the surfaces are brought into ultimate contact as vdW interactions can act only in distances around 10 nm down to interatomic separation distances of ~0.2 nm [74]. Being so, it is experienced that real surfaces do not spontaneously stick to each other given that their natural roughness does not allow the formation of intimate contact. In contrast to short-range vdW forces which require intimate contact, CE-driven electrostatic interactions are considered long-range forces, which are effective in scales of even a few micrometers [32,33]. The longer effective range of electrostatic interactions is simply due to the fact that they deal with significantly larger charges – such as electrons – instead of molecular and atomic dipoles which cause the vdW interactions.

Another important effect of the larger electric charges involved in electrostatic interactions is on the magnitude of the electrostatic forces, normally larger than that of the vdW forces. For example, in a characteristic contact between silica and mica thin films (R = 1.5 cm) at the typical interatomic separation distance of ~0.2 nm, the vdW force interacting between the two substrates is $\sim 5.6\times10^{-3}$ N, according to Equation 2.6, where the Hamaker constant can be considered as $\sim 9\times10^{-20}$ J [107]. However, for the same contact, CE-driven electrostatic pull-

off forces as large as $70\pm25\times10^{-3}$ N have been reported [107], which are almost 8–17 times larger than what can be obtained through vdW interactions.

As discussed in subsections 2.3.1.1 and 2.3.1.2, the magnitude of the vdW force obtainable during contact between two perfectly smooth substrates is independent of the applied preload and is only governed by the properties of the materials. During contact, however, CE-driven electrostatic interactions are load-dependent as the magnitude of the electrostatic force generated via CE is dependent on the area of the contact (see Equation 2.14 in subsection 2.3.2.2). According to this and in order to give a better insight into the contribution of the adhesive vdW and electrostatic forces interacting between two substrates in contact, the work of adhesion, as an area-dependent variable showing the adhesive ability of a unit area of a surface, needs to be determined. As a case in point, Horn and Smith [32] found that the electrostatically-driven work of adhesion between silica and mica thin films in contact ($R \approx$ 20 mm) is about 6.6–8.8 J/m^2 [32]. However, knowing from the Hamaker method (Equation 2.6) that the vdW-originated pull-off force between the same thin films is $\sim7.5\times10^{-3}$ N and recalling the JKR model (Equation 2.12), it can be stated that the vdW-driven work of adhesion in the same contact would be only $\sim8.0\times10^{-2}$ J/m^2. In fact, the work of adhesion caused by CE-originated electrostatic interactions between silica and mica thin films is approximately 100 times larger than that obtainable through vdW interactions.

In general, electrostatic forces developed through CE can generate significantly larger adhesion forces in comparison to vdW interactions. Even so, the role of electrostatic

interactions in the adhesion of dry adhesives (which are commonly composed of insulating materials, thus showing great propensity to getting charged at the surface) has not yet received sufficient attention in the literature.

Chapter 3. Fabrication of Bi-level Teflon AF Nanopillars and their Adhesion in Dry and Wet Conditions

3.1 Introduction

Gecko lizards have an amazing aptitude to stick readily and rapidly to almost any surface and are well adapted to both dry and wet conditions [2-5,126,127]. The superior adhesive ability of gecko has been attributed to the fine hierarchical structure of their foot pads containing millions of finger-like spatulas mainly made up of β-keratin [20,21], a rigid non-sticky material. Synthetic polymeric gecko-inspired dry adhesives have been fabricated from different polymers such as polydimethylsiloxane (PDMS), polyurethane (PU), and polypropylene (PP) [18,79]. The limited success of polymeric gecko-inspired adhesives are mainly because of the difficulty of generating high aspect-ratio (AR) and high density micro/nanoscopic hierarchical structures (or fibrils) which, unlike the fibrils of gecko toe pads, bundle or collapse owing to the self-adhesion between micro/nanofibrils [128,129].

We have speculated that the extremely low surface energy and the exceptional mechanical strength of amorphous fluoropolymer Teflon AF can make it an excellent alternative material to produce high AR and high density nanoscopic structure for fabrication of gecko-inspired adhesives. Fluoropolymers are well-known for their non-reactive surfaces with limited van der Waals (vdW) interactions [122], which make them ideal candidates for fabrication of "releasing" and "anti-fouling" surfaces. However, they have the capability of producing

strong electrostatic interactions in contact with positively polarizable materials. Therefore, the incorporation of a fluoropolymer in a specially designed nanostructure based on the hierarchical structure of a gecko foot pad can result in fabrication of a novel dry adhesive with interesting adhesion properties. For the first time, we fabricated high AR Teflon AF nanopillars terminated with a "fluffy" top layer [97], which meet most of the design criteria for the development of gecko-inspired dry adhesives [18]. These nanopillars are shown to have an exceptional capacity to generate strong adhesion in both dry conditions and surprisingly under water (~70% of their dry adhesion strength).

3.2 Experimental

3.2.1 Materials

Teflon AF 1600 was purchased from DuPont. Anodic aluminum oxide (AAO) membranes (Anopore Inorganic Membrane; 0.2 μm pore size, 25–50% porosity, 60 μm in thickness) were purchased from Whatman, Inc. All other chemicals and solvents were from common suppliers and used without further purification. DI-water (resistivity > 10MΩ.cm @ 25 °C; total organic carbon (TOC) < 50 ppb) was obtained on a RiOs-DI Clinical system (Millipore Corporation).

3.2.2 Methods

For the fabrication of Teflon AF nanopillars, the replica-molding technique was applied. Initially, the AAO membrane was placed on a hotplate which was covered with aluminum foil. A stainless steel cylinder with inner diameter of ~19 mm was placed on the mold. Then, ~0.2 g Teflon AF was placed inside the cylinder with a stainless steel piston over it; a 5 pound weight was placed over the piston (see Figure 3.1).

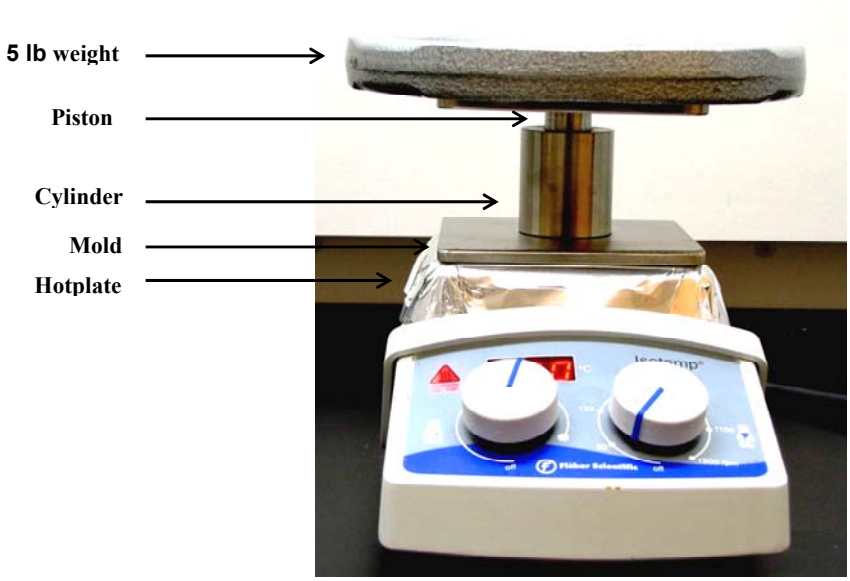

Figure 3.1. The set-up used for fabrication of Teflon AF hierarchical nanopillars. The mold was placed on the aluminum foil over the hotplate and the cylinder from its square base was placed over the mold. The whole setup was heated up to 300 °C and the temperature was held constant for 5 h.

The mold and the polymer were heated up gradually to 300 °C and then the temperature was kept constant for 5 h. It should be noted that since the heat exchanging surface area was high, the actual temperature at which the polymer was processed must have been lower than the preset temperature. At the end, while the mold and the polymer were kept under pressure, the setup was cooled down to room temperature by an air stream. After cooling, the sample was

removed from the hotplate. Following that, the sample, while still connected to the cylinder, was immersed in 1.25 M NaOH solution while stirring. After 6 h, the sample was removed from the cylinder and transferred to a fresh 1.25 M NaOH solution; it should be noted that according to the literature, Teflon AF is completely resistant to NaOH [25]. After 18 hr, the sample was removed from the solution, rinsed with DI-water, and then dried with an air stream. Complete drying was achieved by vacuum drying at the ambient temperature overnight. Rearrangement of nanopillars during drying made the appearance of fabricated samples turn opaque from transparent (see Figure 3.2). An interesting characteristic of Teflon AF nanopillars was the formation of three distinct drying zones during drying.

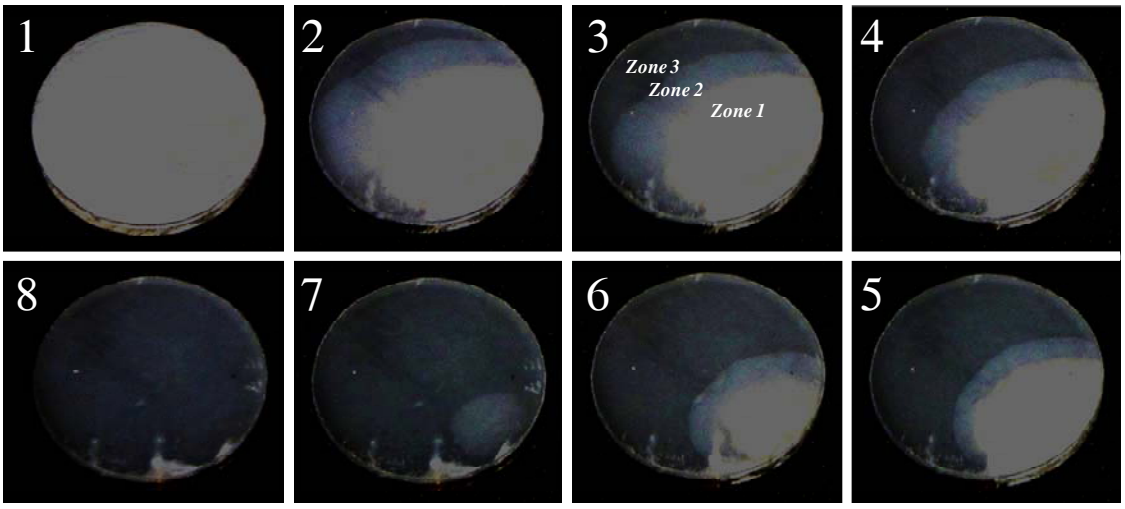

Figure 3.2. Sequential optical images of a sample (~19 mm in diameter) from wet to dry states (1→8) during drying. Drying of nanopillars caused the appearance of nanopillars to turn opaque (image 8) from the original transparent form (image 1). It can also be seen that in intermediate stages of drying (2–6), three distinct drying zones exist. Zone 1 belongs to a completely wet area, while Zone 2 consists of a partly dried area in which the top terminating nanostructure has been dried. The completely dried nanopillars, both trunks of nanopillars and top terminating nanostructure, form Zone 3.

For fabrication of the flat Teflon AF (control) samples, the polymer particles were placed on a clean silicon wafer and an aluminum foil-covered microscope glass slide (with a 200 g weight over it) was placed on them. The temperature increased gradually to 300 °C and after 5 h, the whole setup was cooled down by an airstream. Finally, the sample was manually peeled off from the silicon wafer. The contact angle of water over the flat control sample was ~107°.

3.2.3 Characterization

A home-built setup equipped with a GSO-25 Load Cell (0–25 g, Transducer Techniques, Inc.) and MFA-CC Miniature Linear Stage (0–25 mm range, 0.0175 μm resolution, Newport Corporation) was used to perform indentation (adhesion) tests. Loading was carried out at the constant speed of 1 μm/s until reaching the nominal preloads of 5, 10, 20, and 50 mN. However, the data analysis was carried out based on actual normal force measurement. After keeping the force constant for 30 s at the desired preload, the unloading step with the same speed of 1 μm/s was performed until the probe completely detached from the sample surface. The probe used for indentation tests was a 6±0.01 mm in diameter hemisphere fused silica UV grade (SiO_2) tip (ISP Optics Corp.). The probe was glued to the probe stub by an ethyl cyanoacrylate (ECA) based glue (Instant Krazy Glue). Before conducting the adhesion tests, the probe was completely washed with ethanol, acetone, and DI-water and was grounded afterwards to remove any possible charge from the surface. Scanning electron microscope (SEM) images were taken by a LEO FE-SEM 1530 (Carl Zeiss NTS) operating at 5 kV.

3.3 Results and discussion

Teflon AF is a copolymer of 2,2-bistrifluoromethyl-4,5-difluoro-1,3-dioxole (PDD) and tetrafluoroethylene (TFE). It has both the expected properties of amorphous and perfluorinated polymers. Teflon AF with Young's modulus of ~1.6 GPa and critical surface energy of 15.7 mJ/m^2 has a very low dielectric constant (ε=1.93), the lowest of any known solid organic polymers [25]. The hierarchical Teflon AF nanopillars were fabricated by replica-molding with an AAO membrane as the mold. Uniform nanoscale pores, absence of lateral crossover between individual pores, and high AR of the pores are the main advantages of this class of membranes for fabrication of high aspect-ratio nanopillars [130]. Figures 3.3.A and 3.3.B show SEM images of the fabricated nanopillars (200 nm in diameter and ~16 μm in height; AR of 80) which have been successfully terminated by a finer nanostructure at the tip. It should be noted that sample surfaces were homogenously patterned (see Figure 3.3.A) but in order to show the structure of the terminating layer, Figure 3.3.B was taken from a defect in a sample. Figure 3.3.C schematically shows the fabrication procedure in which the polymer was placed over the mold and the whole system was heated up to 300 °C. After 5 h, the setup was cooled down and the mold was dissolved in NaOH for 24 h and the samples were air dried afterwards.

The choices of common materials, including the mold and the polymer, and also the fabrication techniques used for fabrication of dry adhesives had limited the fabrication of

hierarchical and high AR nanostructures [18,58,79,129]. The problem was overcome in our research because of the very low surface energy of Teflon AF, its rigidity, and its hydrophobic nature, which reduced the risk of destructive collapsing at the tip of the pillars during drying of samples.

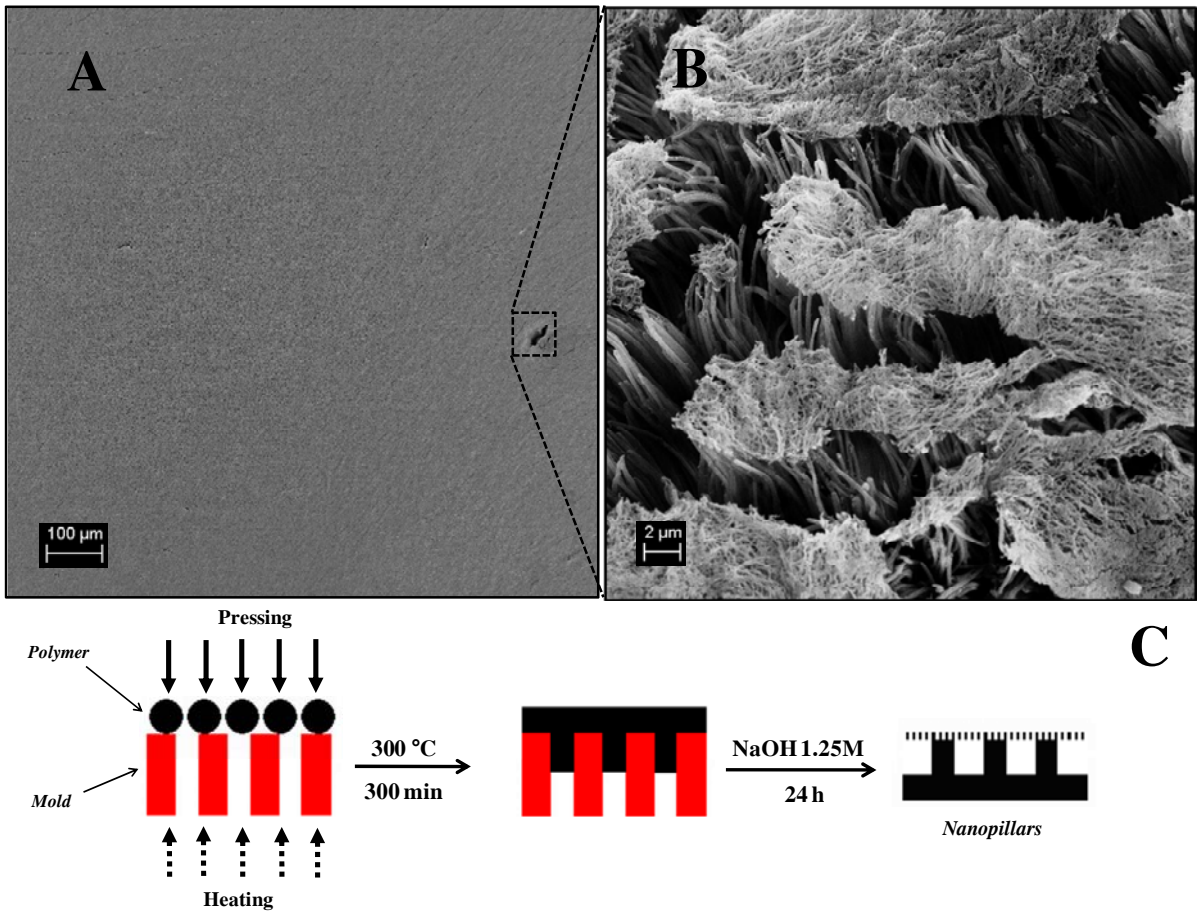

Figure 3.3. (A) SEM image (top-view) of the Teflon AF hierarchical nanopillars terminated at tips with a fluffy nanostructure. (B) SEM image (45°-view) of the trunk of Teflon AF nanopillars terminated with a fluffy nanostructure. (C) Schematic illustration of the replica-molding process.

Generally, collapsing and self-sticking of high AR nanopillars occur during drying of samples due to capillary forces [86]. In our system, there was no noticeable collapsing and

self-sticking. The characteristics of fabricated hierarchical nanopillars during drying were monitored by taking images of the surface during this step (Figure 3.2). It should be noted that rather than the abovementioned parameters, the terminating nanostructure itself also hindered the self-sticking of nanopillars at the pillars tip. This hierarchy level is one of the advantages of this system over previously reported dry adhesives in that it can hinder the self-sticking of nanopillars at the pillar tip during fabrication while it enhances the ability of the dry adhesive to generate strong adhesion in both dry conditions and under water.

The (adhesive) performance of the fabricated bi-level nanopillars under normal forces was characterized by indentation tests where a hemispherical fused silica probe (6 mm in diameter) was pressed to the sample surface until it reached the desired preload ranging from ~5 mN to ~50 mN. The probe was held at the predefined preload for 30 s and then it was unloaded. Both loading and unloading were carried out at a constant speed of 1 μm/s and indentation tests were performed both in air and under water. The tests were accomplished in six distinct experiments and results are presented in Figures 3.4 and 3.5 in terms of penetration depth and pull-off force, respectively, at different preloads; error bars indicate the standard deviation.

Figure 3.4 shows the measured ultimate penetration depth of the probe upon loading for different preloads in air and under water. There was little penetration on the flat control surface due to the high elastic modulus of Teflon AF; however, there was significant penetration of probe into the nanopillars, suggesting a very low effective elastic modulus.

Generally, the effective elastic modulus (E_{eff}) of nanopillars can be calculated by Equation 2.1. Considering E = 1.5 GPa, μ = 0.35, θ = 89 °, and 25% porosity in the mold, which results in $D = 8\times10^{12}$ pillars/m^2, the theoretical effective elastic modulus of the nanopillars, excluding the hierarchy level, would be 1.72 MPa. This very low elastic modulus due to extremely high AR of the nanopillars meets the structural need of low modulus fibrillar structure for an effective dry adhesive. It is interesting that the penetration depth under water was always larger than that in dry conditions, perhaps due to hydrophobic attractions between the Teflon AF nanopillars, resulting in more resistance to the normal loads under water [97].

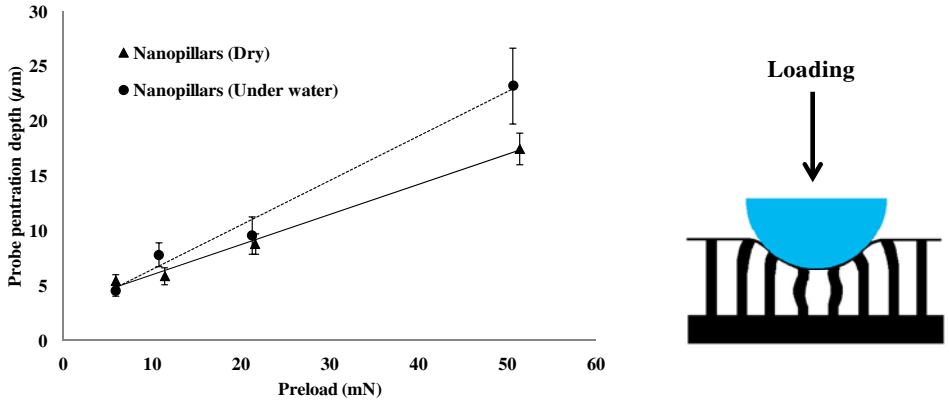

Figure 3.4. Plots of probe penetration depth vs. preload in indentation tests for Teflon AF nanopillars in dry condition and under water. The right panel is a schematic of the deformations of the Teflon AF nanopillars during loading.

Figure 3.5 shows the pull-off force (*i.e.*, maximum adhesive force upon separation of the probe and the sample) for nanopillars, which is much higher compared to that of the flat Teflon AF control surface.

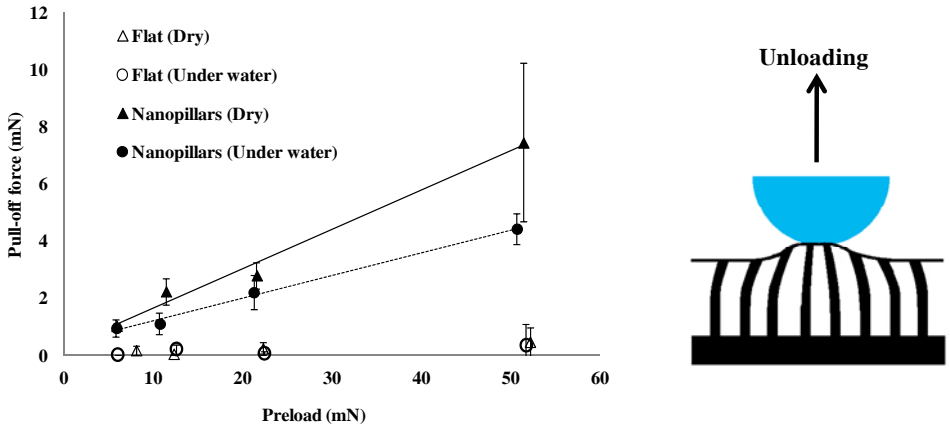

Figure 3.5. Plots of pull-off force vs. preload for flat Teflon AF surface and Teflon AF nanopillars both in dry condition and under water. The right panel is a schematic of the nanopillars elongation during unloading.

The high pull-off forces for the nanopillars are attributed to the enhanced conformability and compliance of the nanopillars to the probe, due to the reduced effective modulus of the surface and the dissipation of stored elastic energy during deformation and detachment of individual nanopillars, as illustrated schematically in Figure 3.5 [18,24,128]. However, owing to the fact that fluoropolymers, specifically Teflon AF, cannot efficiently generate strong vdW interactions, we suspect that, in addition to special structural properties of the fabricated nanopillars, contact electrification (which comes from electrical charge separation following contact between two materials) [30,31] significantly contribute to adhesion enhancement in our system. In particular, for a flat smooth substrate in contact with a probe of radius of curvature R, the pull-off force (F_{vdW}) coming from vdW interactions can be estimated according to the Johnson-Kendall-Roberts (JKR) theory (Equation 2.12). Assuming that the fused silica probe and flat Teflon AF surfaces are smooth and considering

the surface energies of fused silica and Teflon AF as 75 mJ/m^2 [131] and 15.7 mJ/m^2 [25], respectively, the theoretical pull-off force (coming from vdW forces) for the contact of Teflon AF and fused silica would be approximately 0.8 mN. Although Teflon AF is not a very efficient in generating vdW interactions, which is typical for a fluoropolymer, Teflon AF has a very low dielectric constant and is subject to generating electrostatic interactions upon contact with the surface of positively polarizable materials such as silica, leading to enhanced electrostatic-generated pull-off forces [97].

The magnitude of the electrostatic force between two macroscopic charged surfaces can be calculated by modeling charged surfaces as infinite parallel plates, while the separation distance is much smaller than the radius of curvature of the probe (see Chapter 2, subsection 2.3.2.2). Doing so, it is known that the electrostatic force is directly proportional to the contact area which is much higher for nanopillars compared to a flat surface and it consequently increases by increasing the preload, as was observed in our experiments.

Although the fabricated nanopillars generated considerable adhesion in dry conditions, they have another remarkable behavior. They can generate high pull-off forces under water (on average ~70% of the dry adhesion), which is a rare behavior among previously reported dry adhesives. Generally, the functionality of synthetic dry adhesives (SDAs) dramatically diminishes under water due to the presence of a water layer at the interface [39]. To the best of our knowledge, there are only two versions of gecko-inspired adhesives which can operate both in dry condition and under water based on combination of metal coordination bonds, *pi*

electron interactions, and covalent bonds in the first case [39], and suction cup effects in the other [40]. Taking into consideration that none of these mechanisms exist in our system and knowing that vdW and also electrostatic interactions dramatically diminish under DI-water, the high adhesion of Teflon AF nanopillars in water would be very surprising. The hydrophobic nature of Teflon AF (water contact angle ≈ 107°), which can lead to trapping of air in the terminating nanostructure at the pillars tip might be the main reason for the remarkable adhesion of our hierarchical nanopillars under water [97]. The trapped bubbles can neck and bridge between the probe and the nanopillars upon unloading, which consequently generates long-range attraction upon separation of the probe and enhance the pull-off force. In our experiments, we noticed that air bubbles were generated from the nanopillars when immersed in water. Although the visible bubbles were removed carefully, micro/nanoscopic bubbles can still be trapped in the terminating nanostructure at the pillar tips, thus giving rise to long-range attraction between the probe and nanopillars upon unloading of the probe.

3.4 Summary

In summary, high aspect-ratio, high density gecko-inspired polymeric dry adhesives have been fabricated using a non-sticky fluoropolymer (Teflon AF) by replica-molding with a nanoporous anodic aluminum oxide membrane as the mold. The top terminating layer with a "fluffy" nanostructure which has been generated concurrently with the nanopillars in the replica-molding process is a unique feature. It effectively hindered the self-sticking of high

aspect-ratio, high density nanopillars and due to the rigidity of the polymer and its low surface energy delivered superior conformability to substrate surfaces. These Teflon AF hierarchical nanostructures were shown to have the capacity to generate strong adhesion in dry conditions while they can also operate under water with ~70% of their dry adhesion strength. The following chapters will focus on determining the mechanism of the formation of the top terminating layer and on quantifying the different sources of adhesion responsible for the remarkable properties of the fabricated bi-level Teflon AF nanopillars.

Chapter 4. Modifying the Structural Properties of Bi-level Teflon AF Nanopillars and their Electrostatic Interactions

4.1 Introduction

In this chapter, by exploring further and modifying our recently developed fabrication method, we report on the fabrication of nanopillars with different aspect-ratios (ARs) of 27.5 to 225 with terminating layers of different topographical properties. By means of the peculiar terminating nanostructure which held the nanopillars away from each other at their tips, for the first time, extremely high AR nanopillars (up to AR of 185) were fabricated without noticeable collapse at the tip or bundling.

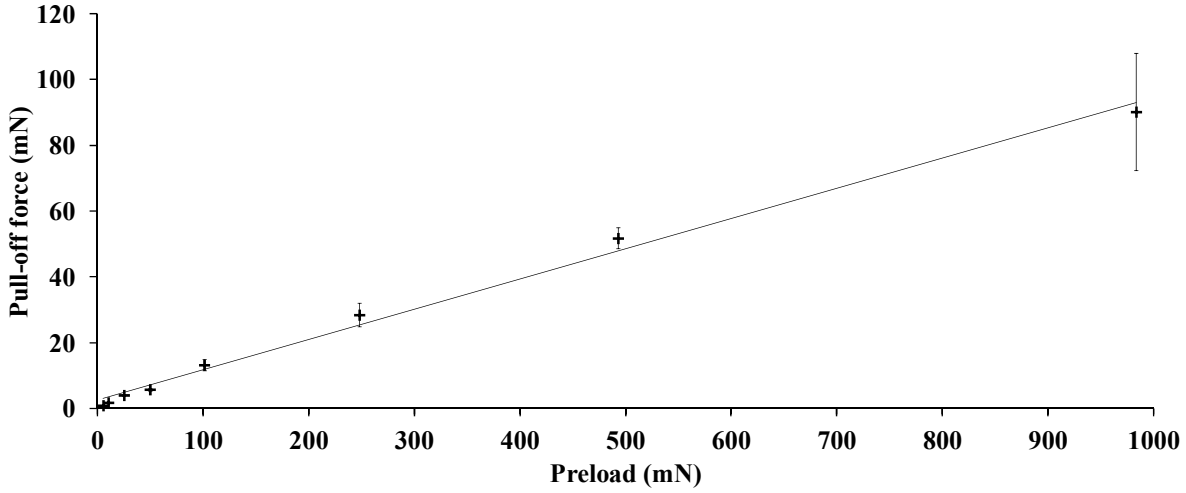

Figure 4.1. Changes in pull-off force vs. preload for bi-level Teflon AF nanopillars of 80 μm tall (AR = 80) in contact with the hemispherical fused silica probe.

The adhesive and frictional properties of the fabricated nanopillars of different geometrical properties were investigated under various loads. The unique electrostatically-driven

adhesion of the current system resulted in enhanced adhesion and shear strengths (up to 1.6 N/cm^2 and 12 N/cm^2, respectively), which not only matched those of the gecko foot pad, but also surpassed them by ~60 and 20%, respectively. The large strength of the long-range electrostatic interactions which were developed through contact electrification (CE) helped the bi-level nanopillars of specific AR and topographical properties to generate extremely large adhesion forces, even up to ~100 times larger than those attainable by short-range van der Waals (vdW) interactions (see Figure 4.1).

4.2 Experimental

4.2.1 Materials

In this research, nanopillars with different heights and hierarchy features were fabricated from Teflon AF by using anodic aluminium oxide (AAO) membranes as the mold. AAO membranes (0.2 μm pore diameter, 60 μm thick, pore density 25–50 %) were purchased from Whatman Inc. Teflon AF 1600, a copolymer of tetrafluoroethylene (TFE) (35 mol%) and 2,2-bistrifluoromethyl-4,5-difluoro-1,3-dioxole (PDD) (65 mol%), was purchased from DuPont. Sodium hydroxide (NaOH; ≥97.0%; Caledon Laboratories Ltd.), copper(II) sulfate pentahydrate ($CuSO_4.5H_2O$; ≥98.5%; VWR International LLC), and nitric acid (HNO_3; 68.0–70.0%; Thermo Fisher Scientific Inc.) were used without further purification. All other common solvents were used as received. The probe used in tribological tests was a fused silica (SiO_2) hemisphere (8±0.01 mm in diameter) from ISP Optics Corp. Deionized (DI)-

water with a nominal resistivity of >10 MΩ cm @ 25 °C and total organic carbon (TOC) of <50 ppb was obtained on a RiOs-DI Clinical system (Millipore Corporation).

4.2.2 Sample preparation

For fabrication of Teflon AF nanopillars, initially, a hotplate was covered with aluminium foil and an AAO membrane as the mold was placed on top of it with the hierarchical level [130] facing up. Then, a stainless steel cylinder with an inner diameter of ~19 mm was placed over the mold. Teflon AF (~0.2 g) was placed inside the cylinder and a stainless steel piston with a 5 lb weight over it was placed on the polymer granules inside the cylinder (for more details regarding the setup used in this chapter, subsection 3.2.1 can be consulted). Temperature was increased to the desired value (*i.e.*, 270, 300, 330 or 360 °C); after 24 h, the hotplate was turned off and the whole setup was cooled down overnight while the sample and the mold were kept under pressure. Subsequently, the sample, while it was still connected to the cylinder, was immersed in 1.25 M NaOH solution. After 6 h, the sample was removed from the mold and immersed in a fresh solution for another 18 h. Finally, the sample was removed from the solution, washed with DI-water, and air dried afterwards. Complete drying was achieved by vacuum drying at room temperature overnight.

For fabrication of flat Teflon AF samples, a bare silicon wafer was placed over a hotplate and Teflon AF granules were placed in an orderly fashion over that. The silicon wafer and polymer granules were covered with a glass Petri dish to hinder the adsorption of excessive

air dust on the polymer surface. The temperature was gradually increased to 340 °C; after 9 h and when there were no visible bubbles in the polymer sheet, the hotplate was turned off and the whole setup was cooled down to room temperature by an air stream. Subsequently, while the polymer sheet was still connected to the silicon wafer, it was immersed in 1.25 M NaOH solution. As soon as the polymer sheet detached from the silicon wafer, it was removed from the solution and immersed in a fresh solution for another 4 h. Finally, the sample was removed from the solution and washed with DI-water and dried afterwards with an air stream.

4.2.3 Characterization

Indentation and load-drag-pull (LDP) tests were carried out to characterize the adhesive and frictional properties of the fabricated hierarchical nanopillars, respectively. In preparation for indentation and LDP tests, each sample was glued to a microscope glass slide using an ethyl cyanoacrylate-based glue (Krazy Glue Corp.) and dried under vacuum at ambient temperature overnight. The fused silica probe, which was used in indentation and LDP tests, was glued to the corresponding probe bases using the same ethyl cyanoacrylate-based glue (Krazy Glue Corp.). Before performing each test, the probe was washed three times with acetone, ethanol, and DI-water and was grounded to remove any possible charge from its surface.

Indentation tests were carried out to study the adhesion properties of the fabricated

nanopillars as well as those of the flat Teflon AF surface (control sample). Indentation tests (under preloads lower than 50 mN) were completed on a home-built setup which was equipped with a GSO-25 Load Cell (0–25 g, Transducer Techniques, Inc.) and a MFA-CC Miniature Linear Stage (0–25 mm range, 0.0175 μm resolution, Newport Corporation) which were monitoring the normal force and the probe displacement, respectively. The preloads were set to nominal values of 5, 10, 25, and 50 mN (on average, actual preloads of 6.32±0.74, 11.44±0.86, 26.14±0.75, and 50.85±0.83 mN, respectively). Indentation tests at elevated preloads were performed on a Universal Material Tester (UMT) from the Center for Tribology, Inc. (CETR). The loadcell used was a Dual Friction/Load Sensors (Medium Range; DFM-1, 0.1–10 N range, 0.5 mN force resolution). The applied preloads were set to nominal values of 100, 250, 500, and 1000 mN (on average, actual preloads of 99.5±1.0, 247.0±1.5, 492.5±1.0, and 982.0±1.5 mN, respectively). All indentation tests were carried out under ambient conditions (temperature, T = 24±1 °C; relative humidity (RH) = 23±1 %). Each point of the indentation test results represents the average from six distinct experiments, while the error bars indicate the corresponding standard deviation. In the indentation tests, the hemispherical fused silica probe (8 mm in diameter) was pressed at a constant speed of 1 μm/s on the sample surface until the normal force reached the maximum preset force of the so-called preload. After holding the probe for 30 s at the specific preload, it was pulled up at a constant speed of 1 μm/s until it completely detached from the substrate.

The frictional properties of the hierarchical nanopillars as well as those of the flat control samples were characterized by LDP tests. In these tests, a hemispherical fused silica probe (8

mm in diameter) was pressed to the sample surface at a constant speed of 1 μm/s (loading step) until the normal force reached the desired preload. After holding the probe for 30 s, it was subsequently dragged over the sample surface at a constant speed of 10 μm/s (dragging step), while the normal force was kept identical to that of the corresponding preload; then, after dragging the probe for a 500 μm distance, the probe was instantaneously moved upward at a constant speed of 1 μm/s (pulling step) until it completely detached from the surface. LDP tests were performed on a UMT machine from CETR. The loadcell used for LDP tests was a 2-axis Friction/Load Sensor (FVL, 1.0–100 mN range, 10 μN force resolution), which simultaneously and independently measured friction force and normal load. The preloads were set to nominal values of 5, 10, 17.5, and 25 mN (on average, actual preloads of 4.89±0.01, 9.79±0.01, 17.14±0.01, and 24.50±0.01 mN, respectively). The same as the indentation tests, LDP tests were carried out under ambient conditions (T = 24±1 °C; RH = 23±1 %); each point again represents the average from six distinct experiments (and error bars show the standard deviation).

In order to determine the actual surface area delivered for contact by each sample, static water contact angle measurement tests were carried out. Water contact angle measurement tests were performed by placing 6 water droplets of ~5 μl in volume on the sample surface to the closest proximity at a rate of 15 mL/min on different spots. The static water contact angle was measured by analyzing the image of each water droplet using a MATLAB code. Scanning electron microscope (SEM) imaging and energy-dispersive X-ray (EDX) spectroscopy were performed on a LEO FE-SEM 1530 (Carl Zeiss NTS) operating at 5 kV.

In preparation for SEM imaging, each sample was coated with a thin (~10 nm) gold layer deposited on the samples by a Desk II cold sputtering instrument from Denton Vacuum, LLC. For SEM imaging after the LDP tests, samples were immersed in acetone for ~24 h. Then, samples detached from glass slides were washed with DI-water and dried afterwards with an air flow before further analysis with SEM. Ultraviolet-visible (UV-Vis) spectroscopy was performed on a UV-2501PC spectrometer (Shimadzu Corporation) to monitor the changes in Cu^{2+} concentration in aqueous copper sulfate solutions, while inductively coupled plasma optical emission spectrometry (ICP-OES) was carried out on a Prodigy spectrometer from Teledyne Leeman Labs to investigate the Cu^{2+} concentration in concentrated nitric acid.

4.3 Results and discussion

4.3.1 Fabrication of bi-level nanopillars

High AR Teflon AF nanopillars terminated with a fluffy nanostructure on top were fabricated by infiltration of the polymer melt into an AAO membrane as the mold. As schematically shown in Figure 4.2.A, the polymer granules were placed over the AAO membrane having pore diameter of ~200 nm and length of 60 μm. The polymer and the mold were heated up to the desired temperature and a constant pressure was applied over the polymer granules to assure the homogenous penetration of the polymer melt into nanopores. During a 24 h processing period, the polymer melt penetrated the nanopores of the mold up to a specific depth depending on the temperature. Particularly, the infiltration depth of the polymer melt

and, accordingly, the height of the fabricated nanopillars were controlled by setting the processing temperature to 270, 300, 330, or 360 °C in order to fabricate nanopillars with heights of approximately 5.5, 16, 37, or 45 μm, respectively (see Figure 4.2.A and Table 4.1).

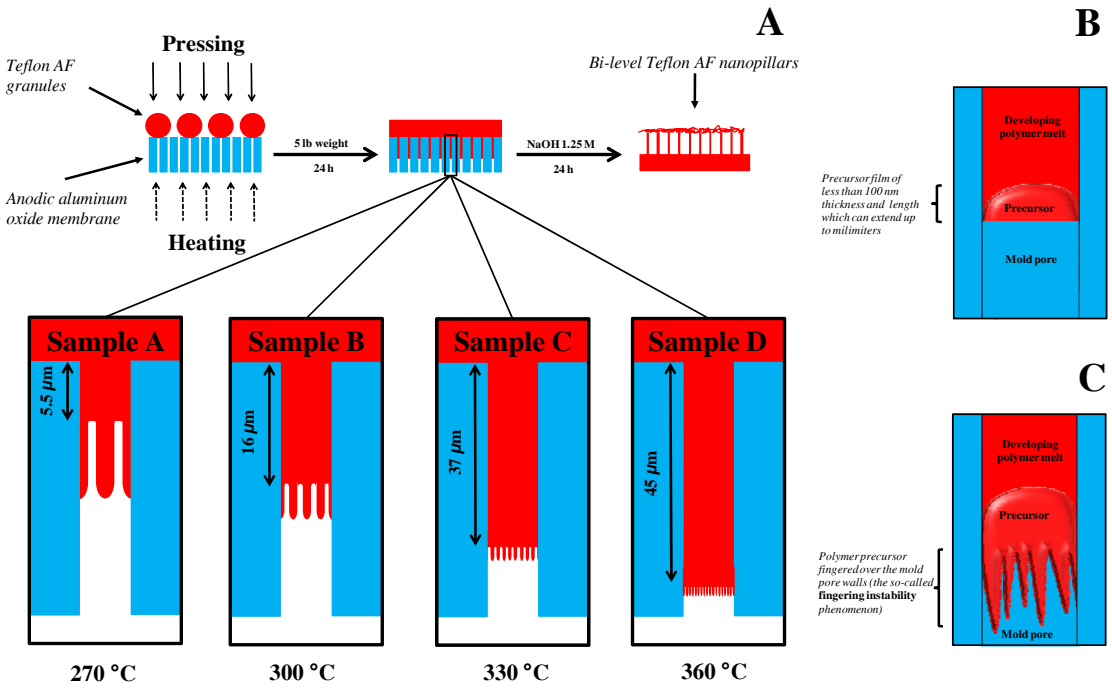

Figure 4.2. (A) Schematic of the fabrication procedure and the effect of the processing temperature on the polymer penetration depth as well as the size and density of the brush-like structure that was formed at the forehead of the developing polymer melt; (B) Formation of a precursor at the forehead of the developing polymer melt in anodic aluminum oxide membrane pore of 200 nm in diameter; (C) Thermocapillarity-driven stresses at the contact line of the precursor led to fingering of the precursor over the pore walls, resulting in formation of a fingerlike structure at the front of the developing polymer melt.

At temperatures lower than 270 °C, the polymer did not effectively penetrate the mold while the highest applied temperature of 360 °C was considered as the onset decomposition temperature for Teflon AF [25]. Since the applied pressure was constant for all samples, the relative penetration depth (h) of the polymer melt in an AAO membrane nanopore at time t

can be calculated by the well-known Washburn equation [132]

$$h = \sqrt{\frac{R(\gamma_A - \gamma_{AP})t}{4\eta}}$$

Equation 4.1

where R is the hydraulic radius (*i.e.*, the ratio between the volume of the polymer melt in the nanopore and the contact area of the polymer melt with the pore wall), γ_A the surface energy of alumina, $\gamma_{AP} \approx (\gamma_P \times \gamma_A)^{1/2}$ the alumina/polymer melt surface tension, and η the viscosity of the polymer melt (γ_P is the polymer melt surface tension). Knowing that by increasing the temperature both the polymer surface tension (γ_P) and its viscosity (η) decline, raising the temperature resulted in deeper penetration of the polymer melt and, consequently, fabrication of taller pillars at the constant processing time of 24 h, as shown in Figure 4.2.A.

Even though fabrication of taller pillars for adhesive applications has always been encouraged, increasing the length of nanopillars enhances the chance of lateral collapsing and bundling of nanopillars [17-19,86,87]. As the height increases, the stiffness of the pillars decreases and after a specific height (L_{max}), the heads of the pillars start to collapse over each other, while further increase in the length of the pillars results in their bundling [17-19,86,87]. The maximum achievable AR for polymeric structures before the start of lateral collapsing has been estimated to be 10–20 [18]. Considering that the Young's modulus (E) of Teflon AF is 1.5 GPa and its surface energy (γ) is 15.7 mJ/m^2 [25], the maximum height for Teflon AF nanopillars before they start to collapse in the lateral direction can be calculated by Equation 2.2. Allowing for r = 100 nm, W = 100 nm, and υ = 0.5, the maximum length (L_{max}) for Teflon AF nanopillars before the nanopillars start to collapse in the lateral direction

would be ~2.2 μm, which dictates a maximum AR of 11. However, one of the advantages of our dry adhesive fabrication method over previously reported techniques was its ability for hindering the lateral collapse and bundling of high AR nanopillars by means of the unique sheet-like nanostructure keeping the tips of nanopillars away from each other.

In order to look into the mechanism behind the fabrication of the fluffy nanostructure terminating the nanopillars at the tip, first the mechanism of the polymer melt infiltration into AAO nanopores should be discussed. In general, the penetration of a polymer melt in AAO nanopores can take place via two distinct mechanisms, the so-called “capillary infiltration” or “precursor wetting infiltration”, depending on the wettability of the polymer melt [133-135]. The wettability of a polymer melt over the AAO pore walls can be quantified by the spreading coefficient (*SC*), which essentially calculates the energy difference between a bare solid surface and a solid surface covered with the polymer melt. $SC \geq 0$ determines the "complete wetting" regime, in which the polymer melt spontaneously spreads over the solid surface. In this regime, a thin (typically <100 nm) precursor film with a length of up to millimetres will form ahead of the developing polymer melt [133-135]. However, $SC < 0$ illustrates the "partial wetting" regime in which the polymer melt partially spreads over the solid surface and reaches an equilibrium shape with a finite contact angle with the solid surface. In this case, the "capillary infiltration" mechanism operates and accordingly, due to capillary forces, the polymer penetrates inside the nanopores and consequently makes nanopillars with a head bulging outward [133-135]. The spreading coefficient of Teflon AF melt over AAO membrane pore walls can be calculated by $SC = \gamma_A - (\gamma_{AP} + \gamma_P)$ [135].

Considering the surface energy of alumina as 0.8–2.5 J/m^2 [136], and that of Teflon AF as 15.7 mJ/m^2 [25], the spreading coefficient for the current system at room temperature would be between 0.67 and 2.29. Therefore, knowing that *SC* would increase by increasing temperature [135], at all processing temperatures of 270–360 °C, the spreading factor for the current system was much larger than zero (*i.e.*, $SC > 0$), which dictates the penetration of the polymer in the mold via the so-called precursor wetting infiltration. In other words, upon infiltration of Teflon AF melt into AAO nanopores, due to the large difference in surface energy of the polymer melt and the mold, a thin nanoscopic precursor film was formed at the forehead of the developing film (see Figure 4.2.B).

However, what really helped the fabrication of the terminating nanostructure over nanopillars was fingering of the polymer precursor film over the AAO pore walls. Put otherwise, at the current length scale where gravitational forces are negligible in comparison to interfacial forces, the thermocapillarity-driven stresses at the contact line of the precursor film resulted in its fingering over the solid surface to form a fingerlike structure at the head of the developing polymer melt (see Figure 4.2.C). As shown in Figure 4.2.A, temperature was increased to reduce the size (length and width) of the hierarchical brushes while enhancing their density. It should be noted that perhaps due to the characteristically rough alumina surface, the actual density and size of the brushes were not as well-defined as those shown in Figure 4.2.A (compare with Figure 4.3) [26]. However, after solidification of the polymer and dissolving the mold in NaOH solution, the fingerlike nanostructure was instantly collapsed during the drying step (see Figure 4.2.A), resulting in formation of a fluffy

nanostructure on top of the base nanopillars of ~200 nm in diameter. As drying continued, the sheet-like nanostructure with sufficiently high density, held the tip of the base nanopillars away from each other and consequently hindered the lateral collapse at the tips during the drying step.

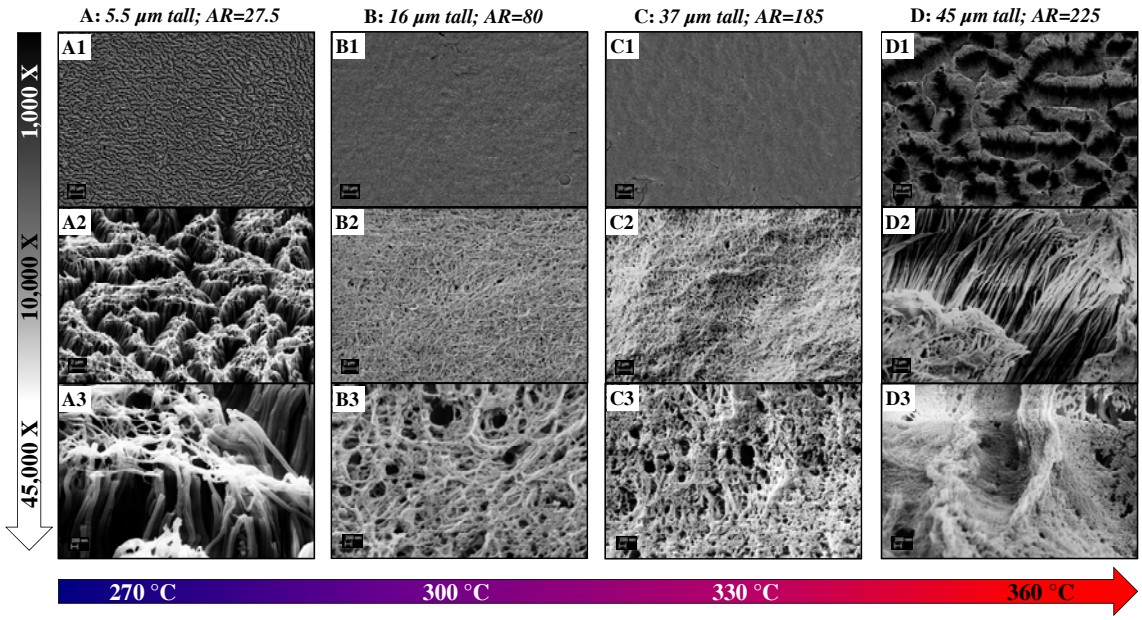

Figure 4.3. SEM images of double-level Teflon AF nanopillars; nanopillars with different heights of approximately (A) 5.5 μm, (B) 16 μm, (C) 37 μm, and (D) 45 μm have been fabricated by setting the temperature to 270, 300, 330, and 360 °C, respectively. The applied pressure and processing time for all samples are the same (~5 lb weight and 24 h processing time). The arrow at the left shows the direction toward which the magnification increases from 1,000 X (top row) to 45,000 X (bottom row), while the middle row shows the samples at 10,000 X magnification. The arrow at the bottom shows the direction toward which the temperature increases from 270–360 °C in 30 °C steps. The top row shows the top-view of the samples while the rest of images are from a 45°–view.

As can be seen in Figure 4.3.A, due to the low density of the terminating layer, the self-sticking characteristic of high AR nanopillars led to the lateral collapse of the shorter Teflon AF nanopillars at their tips (*i.e.*, ~5.5 μm; AR = 27.5), which formed an island-like structure at the surface. However, the high density of the hierarchical level on top of the mid-sized nanopillars (*i.e.*, 16 and 37 μm tall nanopillars) hindered the collapse at the tips and bundling

(see Figure 4.3.B and 4.3.C); the novel sheet-like feature of the top layer helped the fabrication of extremely high AR fibrillar structures up to an AR of 185 without self-mating at the tip or bundling. However, for taller pillars (~45 μm in height, AR = 225), although the terminating nanostructure was very dense, the self-sticking of pillars at the walls led to the bundling of pillars into an island-like structure, but this time at the cost of shrinkage of the top layer (see Figure 4.2.D).

4.3.2 Adhesion and friction of bi-level nanopillars

In order to characterize the adhesive and frictional properties of the fabricated dry adhesives, indentation and LDP tests were carried out on nanopillars of different topographical properties as well as on flat control samples. In an indentation test, a hemispherical fused silica probe (8 mm in diameter) was pressed on the sample surface (loading step) until the normal force reached the maximum preset force (the so-called preload). Then, the probe was pulled upwards (unloading step) until it completely detached from the substrate. Upon detaching the probe from the sample, their adhesion developed forces in the direction opposite to that of unloading. The maximum of this force detected at the final stages of detachment (the so-called pull-off force) was used to illustrate the adhesive ability of each sample. The schematic of an indentation test and typical force traces (*i.e.*, normal force vs. displacement) for all samples are presented in Appendix A.

In LDP tests which were carried out to characterize the frictional properties of the fabricated

nanopillars, after pressing the hemispherical fused silica probe to the sample (loading step), the probe was subsequently dragged over the sample surface for a 500 μm distance (dragging step); then, the probe was instantaneously moved upward (pulling step) until the probe completely detached from the sample. The corresponding normal and lateral forces during all loading, dragging, and pulling steps were recorded and used for analyzing the tribological properties of the samples in the lateral direction. The schematic of an LDP test on bi-level nanopillars is shown in the Appendix A. Before analyzing the indentation and LDP results, we need to study first the contribution of forces (*i.e.*, vdW and electrostatic forces) interacting at the interface of Teflon AF and the fused silica probe.

4.3.2.1 Adhesive forces at Teflon AF surface

The non-retarded vdW force contribution to the adhesive forces between the hemispherical fused silica probe (phase 1) in contact with Teflon AF (phase 2) via air (medium 3) can be estimated by $F_{vdW} = -A_{132}d'/12D^2$ [74], where A_{132} is the material-dependent Hamaker constant between phases 1 and 2 interacting across the medium 3, d' the diameter of the hemisphere, and D the separation distance. According to Lifshitz theory, the Hamaker constant (A_{132}) for the current system would be ~5.64×10^{-20} J at 298 K (see Appendix A for details of its calculation). Therefore, for a typical cut-off distance of ~0.2 nm, the absolute value of the vdW force interacting between a fused silica probe (d' = 8 mm) and Teflon AF surface is ~1.14 mN. The adhesion force generated by vdW forces can also be predicted by the Johnson-Kendall-Roberts (JKR) model (see subsection 2.3.1.2) which considers only the

presence of short-range vdW interactions within the area of contact [104]. According to this theory, the pull-off force (F) detected upon detaching two surfaces is independent of the applied preload and can be calculated by $F = -0.75\pi d' \Delta\gamma$ [104], where $\Delta\gamma \approx \gamma_1 + \gamma_2 - (\gamma_1 \times \gamma_2)^{1/2}$ while γ_1 and γ_2 are the surface energies of fused silica (75 mJ/m^2) [131] and Teflon AF (15.7 mJ/m^2) [25], respectively. Hence, according to the JKR model, for a hemispherical fused silica probe (8 mm in diameter) in contact with Teflon AF, the pull-off force of 1.06 mN is attainable, which is fairly close to that predicted by calculating the Hamaker constant (*i.e.*, 1.14 mN).

Since vdW forces are short-range, it should be noted that the abovementioned adhesive forces at the surface are achievable only via an ultimate contact between two substrates. Due to the high rigidity of Teflon AF (Young's modulus = 1.5 GPa) [25], the actual area of the contact for the nominally flat surface is negligible [6,67]. However, in order to quantify the available surface area delivered by nanopillars of different topographical properties, the static contact angle of water on all samples was measured (see Table 4.1).

Table 4.1. Geometrical and physical properties of bi-level Teflon AF nanopillars and flat control sample with the respective processing temperatures.

Sample	**Pillar diameter** (nm)	**Pillar height** (μm)	**AR**	**Processing temperature** (°C)	**Effective elastic modulus**[a] (MPa)	**Static water contact angle**[b] (degrees)	**Percentage surface fraction (f×100)** (%)
Flat	—	—	—	340	—	105±3	91-100
A	200	5.5	27.5	270	14.57	165±1	4-5
B	200	16	80	300	1.72	146±2	20-25
C	200	37	185	330	0.32	117±5	62-82
D	200	45	225	360	0.22	158±4	6-13

[a] Details regarding the calculation of this parameter can be found in Appendix A.
[b] Measured value ± one standard deviation.

Taking into account that Teflon AF is a hydrophobic polymer and water cannot fill the surface defects, the measured apparent contact angle (θ^*) can be used to approximately calculate the surface fraction of the solid (f) available for contact by the Cassie-Baxter equation

$$cos(\theta^*) = f(1 + cos(\theta)) - 1$$

Equation 4.2

where θ is the water contact angle on a flat Teflon AF surface (104°) [25]. According to the percentage surface fraction ($f \times 100$) of each sample, it can be seen in Table 4.1 that by decreasing the size of the top level and enhancing its density (Figure 4.2.A), the percentage area fraction has increased from 4–5% for sample A, which had an island-like structure (Figure 4.3.A), to 62–82% for sample C with a fluffy sheet-like surface feature (Figure 4.3.C), leading to an enhanced actual surface area of pillars with a smaller size of the top level. Even though sample D had the smallest feature size, pillar bundling led to shrinkage of the terminating level (Figure 4.3.D), which again decreased the percentage area fraction to 6–13% and, consequently, led to a smaller contact area (upon contact). It can be seen that even in the best case scenario, the fabricated nanopillars cannot develop an intimate contact with the smooth fused silica probe in order to develop optimum vdW interactions (1.06–1.14 mN). However, as shown in Figure 4.1 for typical cases, the adhesion forces detected for the compliant Teflon AF nanopillars can reach remarkably large values (~100 mN), while they became enhanced linearly by increasing the preload, both suggesting the existence of a source of adhesion other than vdW interactions. Even without these experiments and calculations, it is well established that fluoropolymers like Teflon AF fail to generate

effective vdW interactions, which along with their surface nonreactivity make them ideal candidates for fabrication of non-sticky and releasing surfaces [137,138].

However, Teflon AF as a fluoropolymer can generate large electrostatic interactions since it is a very efficient material for electron trapping and storing [139], which makes it subject to getting charged at its surface upon contact with other materials via CE. In order to get an idea about the charge storing capacity of Teflon AF upon its contact with fused silica and, accordingly, its potential for generating electrostatic interactions with the probe used in indentation and LDP tests, a separate series of experiments was carried out. Based on the method employed by Liu and Bard [42], who characterized and quantified the electrons accumulated over a Teflon surface after contact with different materials including glass, Lucite, or metal, the surface of five thin (typically < 200 μm) flat Teflon AF sheets (5×20 mm^2) was rubbed with the same fused silica probe used in indentation and LDP tests for ~20 s. Following the rubbing by the fused silica probe, Teflon AF sheets were immersed in a $CuSO_4$ aqueous solution, in which the separated electrons reduced the Cu^{2+} ions into pure Cu ($Cu^{2+} + 2\bar{e} \rightarrow Cu$), which was instantaneously deposited at the sample surface. Figure 4.4.A shows the EDX spectrum of the Teflon AF surface after copper deposition, while Figure 4.4.B represents the changes in optical absorbance of Cu^{2+} in 4 mL of 1 mM $CuSO_4$ solution before and after immersing 5 pieces of the flat Teflon AF sheets in the solution. In order to measure the surface charge density, the deposited copper on Teflon AF sheets was subsequently dissolved in concentrated nitric acid for further analysis with ICP-OES, which indicated a surface charge density of ~7.7×10^{-3} C/cm^2 according to the geometric area. The

measured charge density of ~7.7×10^{-3} C/cm^2 was close to that measured for Teflon after rubbing with Lucite (*i.e.*, 0.1×10^{-3} C/cm^2) [42], while it was relatively larger compared to typical values for other polymers [31].

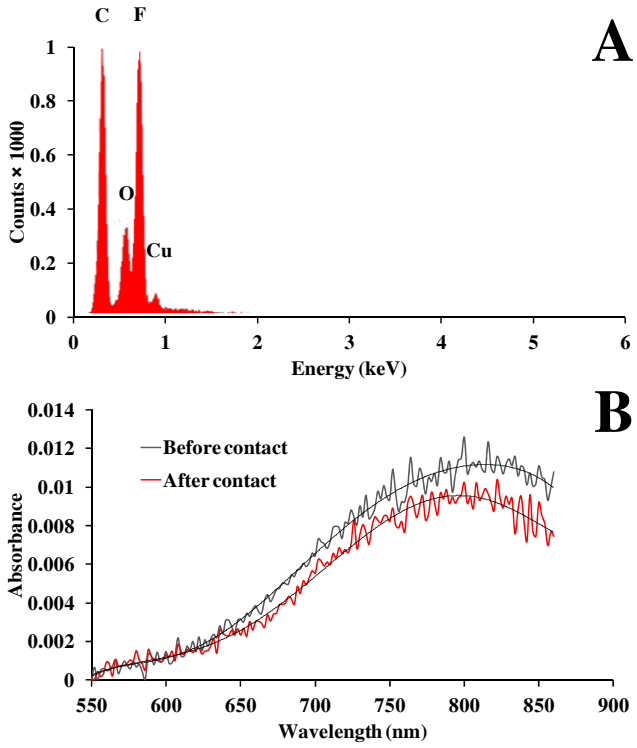

Figure 4.4. (A) EDX spectrum of flat Teflon AF surface after deposition of Cu on the surface by reducing Cu^{2+} ions from 1 mM $CuSO_4$ aqueous solution using the electrons accumulated at the surface after rubbing the Teflon AF surface with a hemispherical fused silica probe. (B) Optical absorbance of 1 mM $CuSO_4$ aqueous solution before and after immersing 5 pieces of charged flat Teflon AF samples (5×20 mm^2) in a 4 mL solution.

Accordingly, in the subsequent section and through the analysis of all indentation and LDP test results, the contribution of the relatively weaker vdW forces at the surface will be neglected, whereas the adhesive and frictional properties of the fabricated nanopillars will be discussed only in regard to their ability to generate electrostatic interactions as the dominant

forces in the current system [29].

4.3.2.2 Adhesion and friction tests

The data obtained in indentation tests, which were carried out to study the adhesive properties of the bi-level Teflon AF nanopillars as well as those of the flat control samples, are shown in Figure 4.5. Figure 4.5.A shows the pull-off forces generated under different preloads for nanopillars of distinct topographical properties (samples A to D; see Table 4.1 and Figure 4.3). In order to study the electrostatic forces operating between bi-level Teflon AF nanopillars in contact with the fused silica probe, they can be modelled as infinite parallel plates (see subsection 2.3.2.2) when considering that the separation distance (typically < 5 μm) is much smaller than the radius of the curvature of the probe (8 mm) and the diameter of the contact area (250–400 μm), and assuming that no deformation occurs upon contact while the charge densities at the surfaces are uniform and equal [32,107]. Hence, the magnitude of the electrostatic force (F_{elc}) can be calculated by Equation 2.14. Although Equation 2.14 is approximate, it clearly shows that in the case of charged surfaces, the operating electrostatic force is dependent on the surface charge density while it is directly proportional to the contact area (and, accordingly, to the applied preload). Although the influence of the latter factor (*i.e.*, enhancement in the surface area) on adhesive properties of the samples will be fully discussed shortly, the role of the former was not explored in detail in that measuring the surface charge density in the current system is not practical and, if possible, it would not be very accurate (see Appendix A for more details) [29].

It can be seen in Figure 4.5.A that for the tallest nanopillars (sample D; ~45 μm tall), under all applied preloads, negligible pull-off forces were detected (comparable to those of the flat control sample), which were attributed to the collapse and bundling of the nanopillars and accordingly the very small actual area of contact [19,58,87]. However, for one level shorter pillars (sample C; ~37 μm tall) which did not collapse because of the presence of the terminating layer on top, considerable pull-off forces were detected while still lower than those for sample B (~16 μm tall). Although sample B had lower surface area available for contact in comparison to sample C, it showed a remarkably superior adhesion performance especially at elevated preloads (see Figure 4.5.A), most likely due to a lower chance of buckling during loading because of their lower height compared to 37 μm tall pillars [19,53,58,87]. As the height decreased further (sample A, ~5.5 μm tall), it was observed that the pillars showed remarkable adhesive properties at low preloads while at higher preloads, their efficiency in generating adhesion compared to more flexible taller pillars was lower, as expected [53]. Basically, pillars having lower ARs have larger values of the effective elastic modulus (see Table 4.1) and consequently, at an identical preload, there is a smaller number of pillars at the contact zone compared to higher AR pillars, which decreases the actual contact area and consequently the generated pull-off forces [18,19,128].

It should be mentioned that only the pull-off force values in the preload range of 5–50 mN are reported in Figure 4.5.A in that the nanopillars showed their best performance (*i.e.*, highest pull-off force per unit surface area) in this range. In other words, it was observed that

by enhancing the preload, the achieved pull-off force values went through a maximum and beyond that they started to slightly decline (see Appendix A). The maximum achievable adhesion strength (pull-off force per unit surface area) and its corresponding preload for each sample are presented in Figure 4.5.B (see Appendix A for more details).

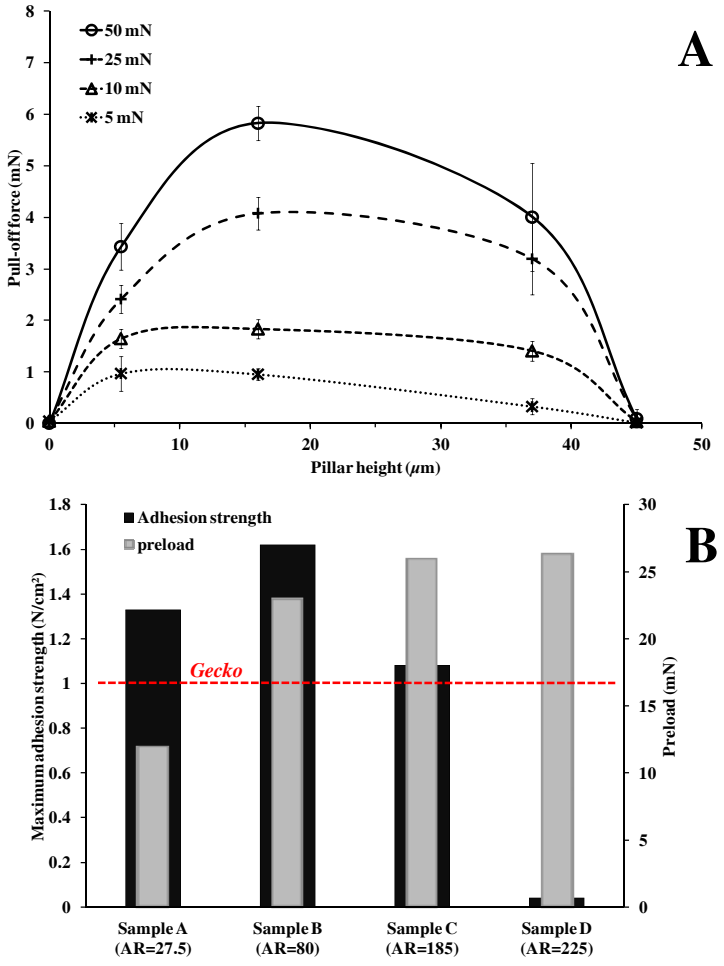

Figure 4.5. Indentation test results. (A) Pull-off force for flat control samples and double-level nanopillars of 200 nm in diameter with different heights of ~5.5, 16, 37, and 45 μm at nominal preloads of 5, 10, 25, and 50 mN. (B) The maximum achievable adhesion strength (pull-off forces per unit surface area) for the same nanopillars. The dashed red line shows the normal adhesion strength of natural gecko foot hair.

It was observed that the shortest nanopillars (5.5 μm tall) showed very high achievable

adhesion strength of ~1.3 N/cm^2 at a very small preload of ~12 mN, while for samples with larger pillar heights and smaller top layer feature sizes, the maximum adhesion strengths were achievable at higher preloads. By increasing the height to 16 μm, the adhesion strength was elevated to the remarkable value of ~1.6 N/cm^2 which was still attainable at the relatively small preload of ~23 mN. Enhancing the height to 37 μm for sample C lowered the efficiency of the dry adhesive most probably due to the elevated chance of buckling during the loading step [19,53,87], as well as the large possibility of the damage of its relatively smaller-sized top level at higher preloads. As mentioned, even though the tallest nanopillars (45 μm tall) had the smallest hierarchy feature size, due to collapsing of pillars and their bundling, they could not conform to the probe during loading, leading to a weak adhesion performance in comparison to other nanopillars [19,53,58,87].

The frictional properties of the fabricated nanopillars as well as those of the flat control samples were studied by LDP tests (see Figure 4.6). Figure 4.6.A shows typical friction traces (force vs. time) from LDP tests on 37 μm tall double-level nanopillars (sample C) and a flat control sample; the plot shows both the changes in the normal force (F_z) and the lateral force (F_x) from ~10 s before the start of dragging to ~10 s after unloading, while the preload was set to a nominal value of 10 mN. It can be seen in Figure 4.6.A that at the start of the dragging of the probe over the nanopillars, a rapid and substantial decrease in the absolute value of the normal force was detected. It seems that due to enhanced compliance of the nanopillars in the lateral direction compared to the normal direction, the normal force was suddenly released and a significant decline in the absolute value of the normal force was

detected, as previously reported and discussed for micron-sized fibrillar structures [68,69]. This incident was not observed for the flat control sample (Figure 4.6.A and Appendix A for more details). Nonetheless, since the LDP instrument was operating at a constant normal force mode, the loading force was recovered within a few seconds after the start of dragging (Figure 4.6.A).

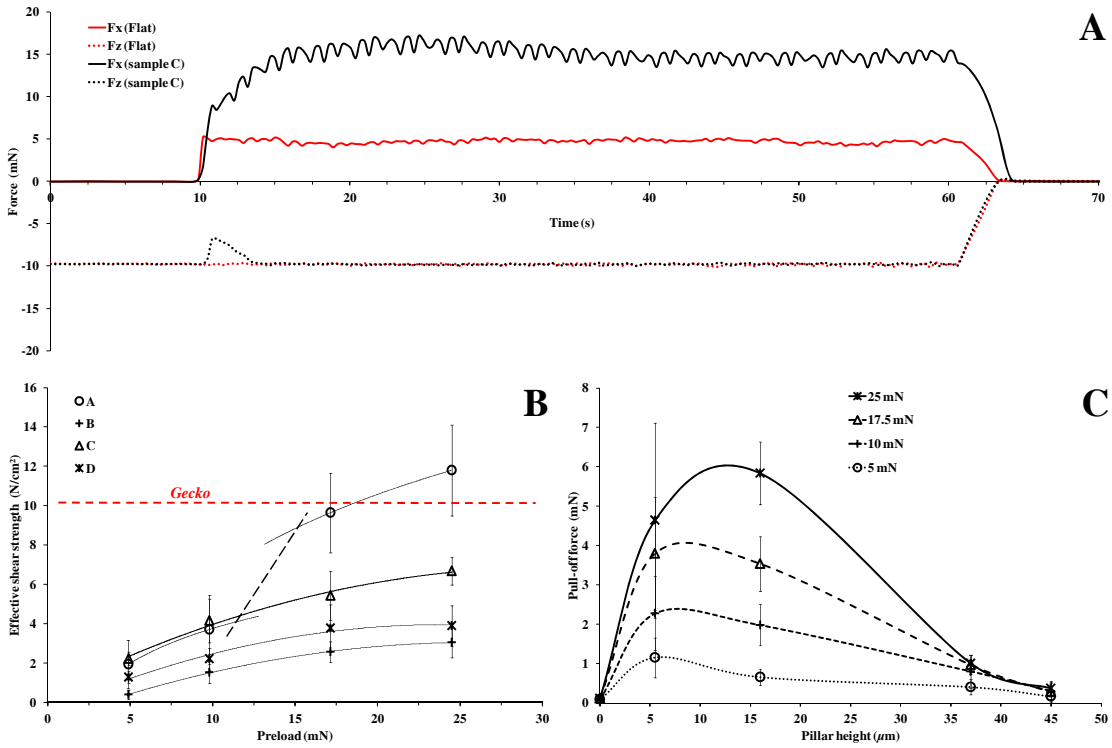

Figure 4.6. LDP test results. (A) Typical friction traces (force vs. time) for 37 μm tall double-level nanopillars and a flat control sample; changes in the normal force (F_z) and the friction force (F_x) are shown for ~10 s before the start of dragging to ~10 s after the unloading at a nominal preload of 10 mN. (B) Effective shear strength at the start of the dragging step in LDP tests for the flat control sample and nanopillars of 200 nm in diameter with different heights of ~5.5, 16, 37, and 45 μm at nominal preloads of 5, 10, 17.5, and 25 mN. The red dashed line shows the shear strength of natural gecko reported in the literature. (C) Pull-off force values measured upon unloading in the same LDP tests for the same samples.

It was also observed that during the rest of the dragging step, due to the characteristic stick-

slip phenomenon, the friction force significantly fluctuated in a periodic manner [107,140], while its average value (almost three times larger for the 37 μm tall nanopillars in comparison to the flat control sample) slightly deviated as the probe was dragged further over the nanopillars. The stick-slip phenomenon, which was more significant for nanopillars, is due to local surpassing of the adhesive force to the applied lateral force, resulting in periodic fluctuations in the measured friction force [107,140].

Similar to a gecko, an effective dry adhesive should be able to generate strong shear strength, preferably higher than that of normal adhesion [7,90]. The friction force (F_x) measured in LDP tests can be related to shear strength (S) by $F_x = S + \mu F_z$ [6], where μ is the Coulomb friction coefficient (≈0.35) and F_z the applied normal force. While the first term (*i.e.*, shear strength, S) comes from interfacial adhesion demonstrating the shear performance of the surface, the second (μF_z) represents the load-dependent friction force, which relies on the properties of the bulk material. In view of that and in order to have a better insight into the shear performance of the nanopillars, the load-dependent friction force was subtracted from the measured friction force (F_x) and the term "shear strength coefficient" or "effective shear strength", as $\tau = S/a_{con}$, was defined (a_{con} is the apparent contact area). While the value of τ for a flat surface is almost zero, due to the high rigidity of Teflon AF and consequently negligible actual contact area [6,67], the corresponding effective shear strengths for different nanopillars were significantly high, as shown in Figure 4.6.B.

Basically, a fibrillar adhesive capable of generating effective sidewall contact can exhibit

elevated shear performance, which would improve via the enhancement in the actual contact area at higher preloads, accordingly improving the shear strength at higher normal forces [67,68,90]. Due to the geometrical properties of the shortest nanopillars (*i.e.*, low density of the hierarchical level), only these nanopillars can make an effective sidewall contact with the fused silica probe (see Figure 4.3.A), most likely leading to their observed improved actual shear strength which reached the value of ~12 N/cm^2 at a 25 mN preload (Figure 4.6.B), about 20% higher than that of a natural gecko (*i.e.*, 10 N/cm^2) [2]. As observed in SEM images taken from the area where each LDP test was carried out (typical SEM images are shown in Figure 4.7), the trunks of the nanopillars were entirely aligned in the direction of the probe displacement (Figure 4.7.A), signifying the efficient sidewall contact with the probe. However, the changes in shear strength of the shortest nanopillars (5.5 μm tall) by increasing the preload took place in two distinct regimes; this incident was previously reported for other nanopillars as well [64]. Comparing the probe penetration depth (see Appendix A) with the size of the nanopillars shows that in the first regime (low preloads), the penetration depth is smaller than the size of the nanopillars. On the other hand, in the second regime (higher preloads), the probe penetration depth is larger than the height of pillars, consequently involving the backing layer in supporting the applied load. Therefore, the change in the shear strength enhancement regime was attributed to the extra buckling of nanopillars when the probe penetration depth was larger than the pillar height, which significantly enhanced the actual contact area due to lowering the tip contact and enhancing the sidewall contact [53,87].

Nonetheless, as can be seen in Figures 4.7.B and 4.7.C, for mid-sized nanopillars, the elevated density of the nanostructure terminating the nanopillars at the top hindered the sidewall contact of the nanopillars with the fused silica probe. However, it seems that a sheet-like structure of the top layer, which resembles the thin film-terminated fibrillar interfaces previously used as dry adhesives [52,56], helped the mid-sized nanopillars to still generate elevated shear strength values (up to ~3 and 7 N/cm^2 for samples B and C, respectively).

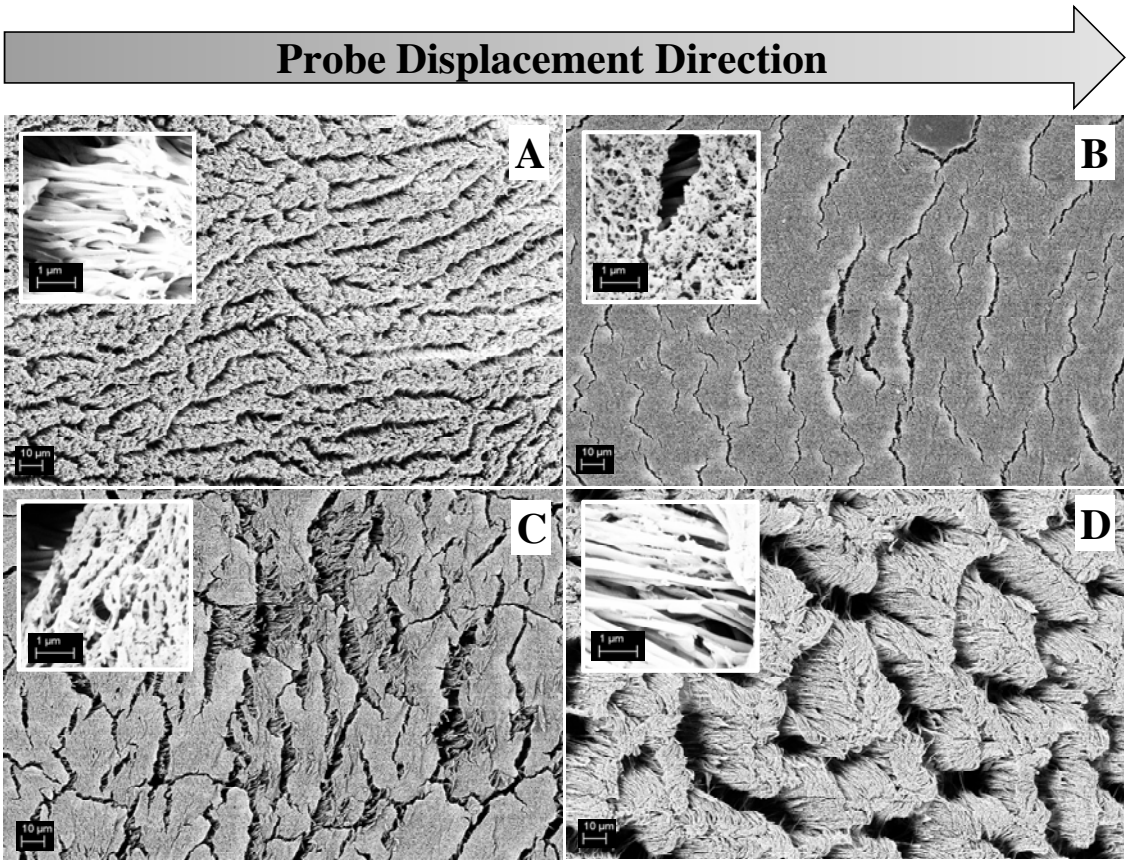

Figure 4.7. SEM images taken after LDP tests carried out on (A) 5.5 μm tall nanopillars (AR = 27.5), (B) 16 μm tall nanopillars (AR = 80), (C) 37 μm tall nanopillars (AR = 185), and (D) 45 μm tall nanopillars (AR = 225) at a nominal preload of 10 mN. The dragging speed for all samples was set to 10 μm/s; the top arrow shows the direction along which the probe was dragged over the samples.

In comparison to these nanopillars, the bundled 45 μm tall nanopillars (sample D) reached a relatively moderate effective shear strength (up to ~4 N/cm^2), most likely due to their ability to generate minor sidewall contact with the probe (see Figure 4.7.D), although they still had a low actual surface area because of the bundling effect [19,87].

However, at the end of the dragging step and during the last stage of unloading, the same way as in the indentation tests, adhesion of nanopillars to the probe led to large pull-off force values as presented in Figure 4.6.C. As expected, the trends of the pull-off force changes at different preloads measured after the LDP tests are almost the same as for the indentation tests. However, the magnitudes of the pull-off forces for all samples (with the exception of sample C) were significantly higher than those measured in indentation tests (compare with Figure 4.5.A). The increase in the pull-off force after dragging was anticipated in that upon sliding the probe over nanopillars, the nanopillars bent and conformed to the probe (see Figure 4.7), leading to an enhancement in the actual surface area upon contact and, consequently, elevated pull-off forces [69]. Besides, during the dragging step, charges can separate more effectively via sliding [31], more likely leading to higher surface charge densities and consequently enhancement in pull-off force (Figure 4.6.C). However, regarding sample C as the tallest unbundled nanopillars with the smallest top layer feature size, it seems that the plastic deformation of the second level, as evident in Figure 4.7.C, has decreased the available surface area after the LDP tests, accordingly leading to smaller detected pull-off forces for the 37 μm tall nanopillars. It can be seen that, despite other samples, the small-

sized hierarchal level of these nanopillars was ruptured in many parts during the dragging step, which reduced the actual surface area and consequently lowered the measured pull-off force of sample C in comparison to that of indentation tests. Nevertheless, it should be noted that for all samples, the measured pull-off force values after the LDP tests were still much lower than the generated friction forces, helping the strong binding in the lateral direction and easy detachment in the normal direction [7].

4.4 Summary

Upon infiltration of Teflon AF melt in the mold, fingering of the polymer melt over anodic aluminium oxide nanopore walls enabled the fabrication of a novel hierarchical level at the forehead of the polymer melt developing in the mold. The collapse of the hierarchical level after removal of the mold and during the drying step resulted in the formation of a dense sheet-like nanostructure on top of nanopillars, which hindered their collapse at the tip. The height of the nanopillars as well as the size and density of the top layer were controlled by adjusting the processing temperature. Due to the presence of the top fluffy layer with an adequate density, extremely high aspect-ratio nanopillars were fabricated, which up to an aspect-ratio of 185 neither collapsed at the tip nor bundled. Despite the very low surface energy of the polymer and its limited van der Waals interactions, its potential to get charged at its surface via contact electrification resulted in an electrostatically-driven adhesion of the fabricated nanopillars. The exceptional geometrical properties of the fabricated nanopillars along with the ability of the polymer to generate excessive electrostatic interactions helped

the fabricated nanopillars to generate strong adhesion and friction strengths up to ~1.6 and 1.2 times those of natural gecko in normal and shear directions, respectively.

Chapter 5. Modifying the Terminating Nanolayer of Bi-level Teflon AF Nanopillars and Studying their Adhesion Properties

5.1 Introduction

As discussed in the previous chapter, fabrication of bi-level Teflon AF nanopillars, which was carried out via replica-molding, was dependent on the formation of a nanoscopic precursor film of the polymer melt confined within vertically-aligned anodic aluminum oxide (AAO) nanochannels used as the template. More specifically, upon infiltration of the polymer melt into the AAO nanochannels, a thin nanoscopic precursor film was formed ahead of the advancing polymer melt. Due to its special interfacial interactions, the precursor film of the polymer destabilized and ruptured to form an exceptional brush-like nanostructure at the forehead of the advancing polymer melt. Put otherwise, inherent thermocapillarity-driven stresses at the contact line of the Teflon AF precursor film with the AAO pore walls led to its fingering over the substrate, which in turn, gave rise to the growth of a unique brush-like nanostructure ahead of the developing polymer melt. Having a very small and soft feature, the fingered brush-like nanostructure instantaneously collapsed after removal of the mold, resulting in the formation of a special (fluffy) sheet-like nanostructure on top of the base nanopillars of extremely high AR.

At that point, we succeeded in modifying the geometrical properties of the top terminating nanolayer by changing the size and the density of the fingered hierarchical nanostructure (at

the forehead of the developing polymer melt). Modifying the structure of the fingered nanostructure was in fact achieved by adjusting the processing temperature; increasing the processing temperature – from 270 to 360 °C – enhanced the density of the brush-like nanostructure, while it decreased its size (*i.e.*, length and width of each fingered fibril). Even so, the changes in the structural feature of the advancing brush-like nanostructure (and as a result, that of the top terminating nanolayer) were inevitably tied with the variation of the penetration depth of the polymer and so, the height of the fabricated nanopillars. In other words, changing the processing temperature, aside from helping to modify the structure of the top terminating nanolayer, also led to changing the penetration depth of the polymer melt into AAO nanochannels and in turn, the height of the base nanopillars. With respect to the fabrication of an efficient dry adhesive, however, the simultaneous change in both the feature of the fingered hierarchical nanostructure and the penetration depth of the polymer is not favored in the sense that it limits the control over the geometry of the final nanostructure and consequently, its adhesive properties [16-18,22,79].

In this regard and in order to achieve an effectual control over the geometrical properties of bi-level Teflon AF nanopillars, in the current chapter, we report on a novel fabrication technique, which allowed us to efficiently control the geometry of the fingered brush-like nanostructure, but this time, independent of the penetration depth of the polymer melt. The method developed in here basically relies on concurrent heating and cooling of the polymer melt from opposite sides. Similar to conventional infiltration systems (like the one that we previously applied for fabrication of bi-level Teflon AF nanopillars) [29,86,133,134], the

polymer was heated above its glass transition temperature of 160 °C [25], which made possible the efficient penetration of the polymer melt into the AAO nanochannels up to a specific depth. However, in an innovative way, the polymer was concurrently cooled down from the top for the duration of its infiltration into the mold. Simultaneous cooling of the polymer allowed the control over the thermocapillarity-driven stresses of the Teflon AF precursor film confined within the AAO nanochannels and in that regard, over the geometrical properties of the fluffy nanostructure terminating the nanopillars at the tip. Even though changing the cooling temperature (from –20 to 40 °C in 20 °C steps) effectively altered the structural feature of the top terminating nanolayer, interestingly, varying the cooling temperature did not – noticeably – affect the penetration depth of the polymer and accordingly, the height of the base nanopillars. So, regardless of the value of the cooling temperature and by keeping the heating temperature constant at 300 °C, nanopillars of almost identical heights (~25 μm) were prepared.

The height of the fabricated nanopillars was measured from scanning electron microscope (SEM) images taken from the cross-section of each sample. The structural properties of the nanolayer terminating the nanostructure at the top of the base nanopillars were quantified using water contact angle measurements and atomic force microscopy (AFM). Following that, the effects of the structural properties of the fabricated nanopillars on their adhesive and frictional performance were investigated by indentation and friction tests. It is worthwhile mentioning that the exceptional electrostatic-based adhesion of bi-level nanopillars allowed

them to achieve remarkable adhesion and shear strengths, up to ~2.1 and 13.0 N/cm^2, respectively.

5.2 Experimental

5.2.1 Materials

The polymer used for fabrication of the bi-level nanopillars was Teflon AF 1600 (DuPont), which is a copolymer of tetrafluoroethylene (TFE) (35 mol%) and 2,2–bistrifluoromethyl–4,5-difluoro–1,3-dioxole (PDD) (65 mol%). The mold used for fabrication of the nanopillars was anodic aluminum oxide membrane (Whatman Inc.) with a pore diameter of 200 nm and a pore length of 60 μm (pore density = 25–50 %). Aqueous solution of sodium hydroxide (NaOH; ≥97.0%; Sigma) was used to dissolve the membrane after solidification of the polymer in the mold. All other common solvents were used without further purification. The hemispherical fused silica (SiO_2) probe (8 mm in diameter) used in tribological tests was purchased from ISP Optics Corp. The tip used for AFM imaging was a silicon crystal tip (PPP–NCL; thickness: 7.0±1 μm; length: 225±10 μm; width: 38±7.5 μm; radius: 10 nm), obtained from NANOSENSORS.

5.2.2 Fabrication of bi-level Teflon AF nanopillars

Bi-level Teflon AF nanopillars were fabricated by infiltration of the polymer melt into vertically-aligned AAO nanochannels. As shown in Figure 5.1, the polymer granules were

placed over an AAO membrane with nanochannels of 200 nm in diameter and 60 μm in length. For fabrication of nanopillars of identical heights, the AAO mold and the polymer were heated from the bottom at the constant heating temperature (T_H) of 300 °C. On the other hand, to independently control the topography of the nanostructure which was terminating the base nanopillars at the tip, the polymer was concurrently cooled down from the top by adjusting the cooling temperature (T_C) at –20, 0, 20, and 40 °C in order to fabricate samples A, B, C, and D, respectively. After 6 h of processing, the temperature of the whole system was brought to room temperature; subsequently, the mold was dissolved in 1.25 M NaOH solution and the sample was air dried afterwards (see the Appendix B for more details regarding the fabrication of nanopillars as well as that of flat control samples).

5.2.3 Characterization

The surface energy of the polymer melt at various temperatures, ranging from ~260 to 360 °C with ±0.5 °C resolution, was determined by the Axisymmetric Drop Shape Analysis (ADSA) approach using a home-built setup under atmospheric pressure. Details regarding the ADSA method applied and the equilibrium surface tension values measured can be found in Appendix B. SEM images from top and cross-section of the fabricated nanopillars were taken by a ULTRA FE-SEM (Carl Zeiss NTS) operating at 5 kV. In preparation for SEM imaging, each sample was coated with a thin (~10 nm) gold layer by a Desk II cold sputtering instrument (Denton Vacuum, LLC).

To determine the roughness of the fluffy nanostructure terminating the nanopillars at the tip, AFM images were taken from a 5×5 μm^2 area from each sample using a PicoScan atomic force microscope (Molecular Imaging) in the tapping-mode (resonance frequency = 170–180 kHz). Analysis of AFM images was performed with WSxM software from Nanotec Electronica S.L. Each roughness value cited in this report is the average value determined from three distinct scans, while the deviations signify the corresponding standard deviations.

Static water contact angle measurement tests were carried out on all samples to investigate the actual surface area delivered for contact by each sample. A characteristic water contact angle measurement test comprised placing of a ~5 μL water droplet volume on the sample surface to the closest proximity at a rate of 15 mL/min. Using a MATLAB code, the static contact angle of the droplet was measured by analyzing the image of each water droplet taken ~20 s after complete drop of the droplet on the sample. Each point on water contact angle results represents the average from five individual experiments, while the error bars signify the corresponding standard deviation.

The adhesive and frictional properties of the samples were characterized by indentation and load-drag-pull (LDP) tests (*i.e.*, friction tests), respectively. Indentation and LDP tests were performed on a Universal Material Tester (UMT) machine from the Center for Tribology, Inc. (CETR). The load cell used for both indentation and LDP tests was a 2-axis Friction/Load Sensor (FVL, 1.0–100 mN range, 10 μN force resolution), which simultaneously and independently measured friction force and normal load. Indentation and

LDP testes were carried out at ambient conditions (temperature, T = 24±1 °C; relative humidity (RH) = 23±1 %) and each point in the collected data represents the average from at least five independently replicated experiments, while the error bars indicate the corresponding standard deviation. In preparation for indentation and LDP tests, each sample was glued to a glass slide using an ethyl cyanoacrylate-based glue (Krazy Glue Corp.) and dried under vacuum at room temperature overnight. The hemispherical fused silica probe was also glued to the corresponding probe bases using the same glue. Before performing indentation and LDP tests, the probe was washed three times with acetone, ethanol, and deionized (DI)-water, and was subsequently grounded to remove any possible charge from its surface. The indentation and LDP results for flat control samples were retrieved from the results reported in Chapter 4. More details regarding indentation and LDP tests can be found in Appendix B.

5.3 Results and discussion

5.3.1 Fabrication of bi-level Teflon AF nanopillars

Fabrication of bi-level Teflon AF nanopillars was carried out by concurrent heating and cooling of the polymer melt upon its infiltration into vertically-aligned AAO nanochannels. Before looking into the particular effects of the cooling and heating temperatures on structural and topographical properties of the fabricated nanopillars, the dynamics of Teflon

AF infiltration into AAO nanopores and the mechanism of the formation of the terminating nanostructure on top of Teflon AF nanopillars should be discussed first.

5.3.1.1 Polymer infiltration mechanism and formation of the terminating layer

In general, a polymer can penetrate an AAO nanochannel via two distinct regimes of the so-called "capillary infiltration" or "precursor wetting infiltration", depending on the difference between the surface energy of the polymer melt and that of the nanochannel wall [133-135]. This energy difference can be quantified by the spreading coefficient, $SC = \gamma_A - (\gamma_{AP} + \gamma_P)$ [135], where γ_A is the surface energy of the AAO pore wall, γ_P the polymer melt surface tension, and $\gamma_{AP} \approx (\gamma_A \times \gamma_P)^{1/2}$ the pore wall/polymer melt surface tension. At low temperatures where $SC < 0$ (non-wetting regime), the polymer melt penetrates the nanopores by capillary forces via the so-called "capillary infiltration" mechanism. In this regime, the polymer melt develops an acute contact angle with the pore wall and accordingly, nanopillars with a head bulging outwards would be obtained [133,135]. However, at elevated temperatures where $SC \geq 0$, the effective mechanism is "precursor wetting infiltration", in which the polymer melt wets the solid surface and spontaneously spreads over it. In the precursor wetting infiltration regime, a thin (typically < 100 nm) precursor film with a length of up to millimeters forms ahead of the developing polymer melt. The formation of the precursor film, in turn, leads to formation of nanopillars with a head curving inward or, in the extreme case, nanotubes [133,135].

With respect to our system and considering the surface energy of alumina as 0.8–2.5 J/m^2 [136], while that of the Teflon AF as ~7.8 mJ/m^2 at 300 °C (see Appendix B for polymer surface energy vs. temperature results), the spreading coefficient would be between 0.71 and 2.35; that is, infiltration of the Teflon AF melt into the AAO nanochannels took place via the precursor wetting infiltration mechanism and a thin nanoscopic precursor film advanced ahead of the developing polymer melt.

It is worthwhile recalling that formation of a precursor film ahead of a polymer melt is not restricted to Teflon AF, since it has been reported for several polymers processed at elevated temperatures into AAO nanopores [133-135]. Even so, it has been only in the case of Teflon AF precursor films that the films can get destabilized and subsequently, ruptured to form a brush-like nanostructure ahead of the developing polymer melt. More specifically, at the current length scale where the effect of gravitational forces can be neglected in comparison to that of interfacial forces [135], the thermocapillarity-driven stresses at the contact line of the advancing Teflon AF precursor film with the pore walls resulted in its instability and, accordingly, fingering of the polymer film over the AAO pore walls. As illustrated in Figure 5.1, rupture and fingering of the polymer precursor film gave rise to formation of a unique brush-like nanostructure ahead of the developing polymer melt. After removal of the mold – by dissolving that in NaOH solution – and upon drying of the sample, the fingerlike nanostructure instantly collapsed, which resulted in the development of an exceptional fluffy nanostructure on the top of the base nanopillars. Instantaneous formation of the sheet-like nanolayer on top, in fact, hindered the collapse of the base nanopillars at the tip during the

drying step, allowing the formation of extremely high aspect-ratio (*i.e.*, 125) Teflon AF nanopillars without collapsing at the tip or bundling.

5.3.1.2 Effects of heating and cooling temperatures

Knowing that a precursor film can form and subsequently, finger ahead of the Teflon AF melt (as discussed earlier), the polymer and the mold were concurrently heated and cooled from opposite sides (see Figure 5.1).

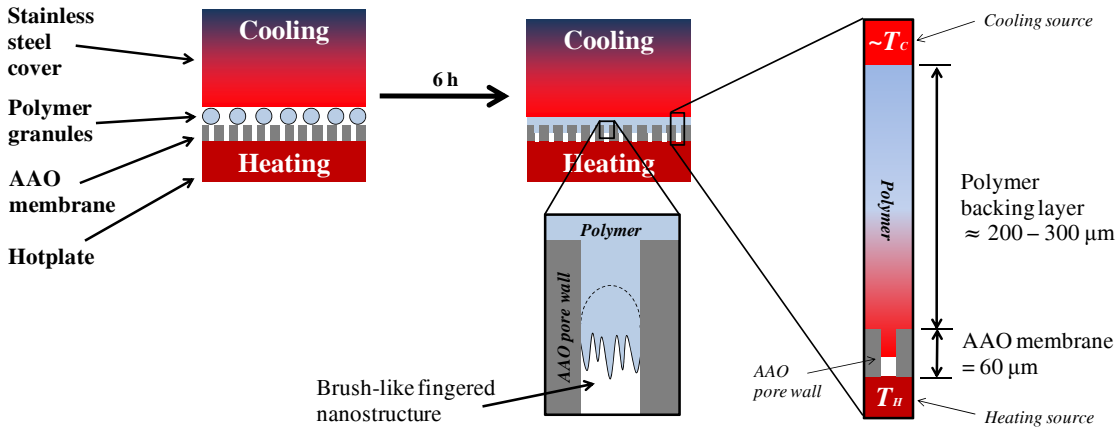

Figure 5.1. Schematic of the fabrication of bi-level Teflon AF nanopillars by infiltration of the polymer melt into vertically-aligned AAO nanochannels. The heating temperature was kept constant at 300 °C to keep the penetration depth of the polymer melt and, accordingly, the height of the fabricated nanopillars constant. On the other hand, the geometrical properties of the brush-like nanostructure at the forehead of the advancing polymer melt and, in turn, the structural properties of the fluffy nanostructure at the tip of the nanopillars, were tailored by adjusting the cooling temperature at -20, 0, 20, and 40 °C.

Doing so, the instabilities of the advancing precursor film and, in view of that, the profile of the nanostructure terminating the base nanopillars at the tip, were modified. In particular, by keeping the heating temperature constant (at 300 °C) while lowering the cooling temperature (from 40 to –20 °C in 20 °C increments), the interfacial instabilities of the precursor film

were ‘excited’ and, therefore, terminating nanostructures with relatively smaller feature sizes were obtained at lower cooling temperatures (see Figure 5.2). Even though adjusting T_C allowed the efficient modification of the geometrical properties of the top terminating nanolayer, interestingly, the infiltration depth of the bulk of the polymer and, as a result, the height of the base nanopillars, did not change distinctly through variation of the cooling temperature. In particular, samples A, B, C, and D (which were fabricated at the cooling temperatures of –20, 0, 20, and 40 °C, respectively) had the base nanopillars of almost similar (~25 μm) height (see Table 5.1). In this respect, prior to discussing the effects of the cooling temperature on geometrical properties of the top terminating nanostructure, we first explain why changing T_C did not affect the infiltration depth of the polymer and consequently, the height of the fabricated nanopillars.

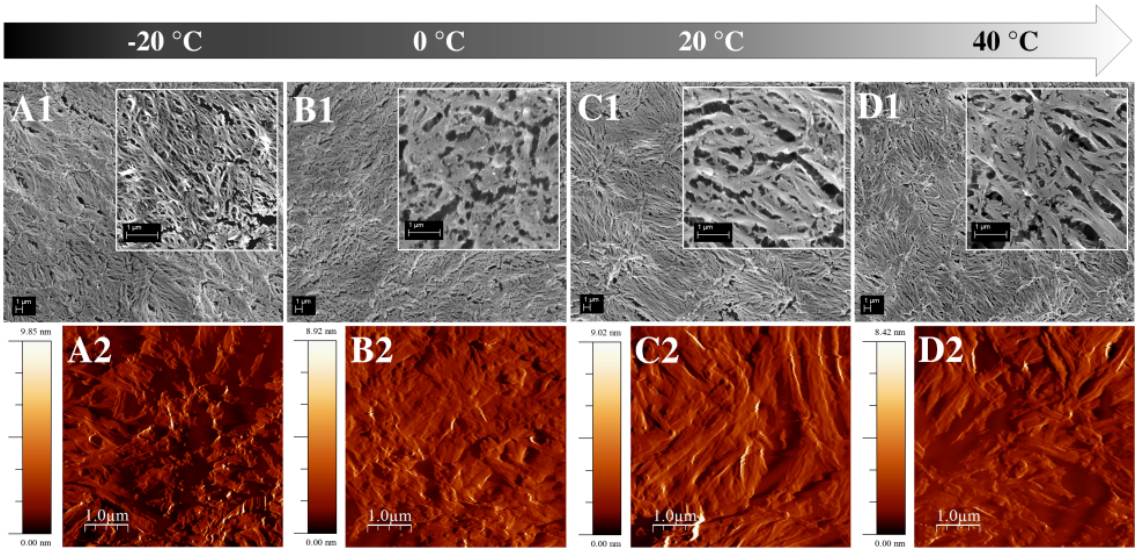

Figure 5.2. Top row shows the SEM images of the top-view of Teflon AF nanopillars processed at the heating temperature of 300 °C and the cooling temperature of (A1) -20 ˚C, (B1) 0 ˚C, (C1) 20 ˚C, and (D1) 40 ˚C. The corresponding amplitude AFM images for the same samples are shown in A2 to D2, respectively.

In general, the penetration depth of a polymer into an AAO nanochannel (at a constant processing period) is only changing with the temperature of the polymer inside the nanopore. More specifically, the relative penetration depth (h) of the polymer melt into an AAO nanochannel can be determined by Equation 4.1 [132]. As temperature affects both the surface energy and viscosity of the polymer melt (*i.e.*, γ_P and η, respectively), Equation 4.1 essentially demonstrates that for a certain processing period (*i.e.*, constant t), the temperature of the polymer is the only parameter controlling its penetration depth. Therefore, at a constant processing time (as in the current system), the higher the polymer temperature is, the deeper the polymer goes into the nanochannels and as a result, nanopillars of larger heights will be obtained [29,135]. It is worthwhile to recall that the increase in the height of Teflon AF nanopillars by increasing the processing temperature has been reported in Chapter 4, where Teflon AF was processed in AAO at various processing temperatures ranging from 270 to 360 °C to fabricate nanopillars of ~5.5 to 45 μm tall.

However, in the current experiments where the polymer was processed at various cooling temperatures (see Table 5.1), it was observed that the height of the fabricated nanopillars were almost similar, regardless of the change in the cooling temperature. According to Equation 5.1, this observation essentially suggests that cooling temperature did not – effectively – affect the temperature of the polymer melt confined within AAO nanochannels. In order to explain the independence of polymer temperature on the temperature of the cooling source (*i.e.*, T_C), first a discussion is needed of what factors are basically altering the temperature of the polymer melt inside AAO nanochannels.

Table 5.1. Geometrical and physical properties of bi-level Teflon AF nanopillars and flat control samples with the particular processing temperatures.

Sample	Pillar diameter (nm)	Pillar height (μm)	AR	Heating temperature (°C)	Cooling temperature (°C)	Static water contact angle (degrees)	Percentage surface fraction (f×100) (%)	Roughness average (R_a) (nm)
Flat	—	—	—	340	—	105 ± 3	91–100	—
A	200	25	125	300	-20	154 ± 3	13 ± 3	55 ± 8
B	200	25	125	300	0	152 ± 1	15 ± 1	60 ± 1
C	200	25	125	300	20	150 ± 5	18 ± 5	67 ± 3
D	200	25	125	300	40	147 ± 3	22 ± 3	73 ± 6

The temperature of a polymer melt confined within an AAO nanochannel, changes in general via two heat exchanging mechanisms: conduction through the polymer plus convection via air [141]. Even so, it has been reported that the effect of convection through air on the temperature of the polymer in an AAO nanochannel can be neglected when compared to conduction through the polymer [141]. Conduction through the polymer melt, on the other hand, naturally falls into two distinct categories: conduction in the "lateral direction" ($\perp$) via the pore wall and conduction in the "normal direction" ($\parallel$) through the nanopore. However, in the current system, due to the small diameter yet large length of the AAO nanochannels, the heat exchanging term of the normal direction ($\parallel$) along the pores can be reasonably neglected in comparison to the conduction term of the lateral direction ($\perp$) with the pore walls. Put otherwise, inside the narrow (200 nm diameter) but long (60 μm long) AAO pore, the conduction in the lateral direction with the highly conductive nanochannel wall (thermal conductivity ($k_{alumina}$) ≈ 16 W/m.K @ 300 °C) [142] is more influential on the temperature of the bulk of the polymer melt than conduction along the pore through the insulating polymer

($k_{Teflon\ AF}$ ≈ 0.42 W/m.K @ 300 °C) (see Appendix B for details on the thermal properties of the polymer).

Therefore, it can simply be stated that the "temperature of the polymer melt" confined within the nanopores was mainly varied by the "temperature of the pore wall" (*i.e.*, AAO membrane). As a matter of fact, this can completely explain why cooling temperature did not significantly affect the temperature of the polymer melt, seeing that the temperature of the mold was effectively set by the temperature of the heating source, but not the cooling source. Otherwise stated, the AAO mold was in direct contact from the bottom with the heating source while, from the top, it was always insulated from the cooling source by an insulating polymer layer of typically a few hundreds of micrometers (~200–300) in thickness (see Figure 5.1). Hence, recalling that the relatively thin AAO mold (60 μm thick) was made up of a material at least forty times more conductive than the polymer, it can be stated that the temperature of the mold and, as a result, that of the polymer melt restricted in the mold were mainly affected by the temperature of the heating source (T_H), while they were practically independent of the temperature of the cooling source (T_C). So, by setting the heating temperature at the constant value of 300 °C and regardless of the changes in the cooling temperature, nanopillars of about 25 μm tall were fabricated (as measured from SEM images taken from the cross-section of the samples).

Although changing the cooling temperature did not noticeably affect the penetration depth of the polymer and as a result, the height of the fabricated nanopillars, it effectively helped to

modify the structural properties of the fluffy nanostructures which were terminating the Teflon AF nanopillars at the tip. Otherwise stated, cooling the polymer from the top and, accordingly, generating a temperature gradient across the setup helped the control over the instabilities of the precursor film, which was advancing ahead of the polymer melt confined within AAO nanochannels. More specifically, it appears that increasing the temperature gradient, by lowering T_C and keeping T_H constant, led to formation of precursor films of seemingly smaller thickness. As previously determined for the case of thermocapillarity-controlled dynamics of planar thin films, those with smaller thickness (which are naturally less stable) are normally split up into features of smaller sizes [26,28]. According to this point of view, it seems that by enhancing the applied temperature gradient (*i.e.*, lowering T_C), precursor films of smaller thickness and consequently, more vulnerable to thermocapillarity-driven instabilities, were developed. Less stable advancing precursor films expectedly ruptured into fibrils of smaller sizes and as a result, terminating nanostructures of smaller feature sizes were fabricated at lower cooling temperatures (see Figure 5.2 and Table 5.1).

The structural properties of the top terminating nanostructure of Teflon AF nanopillars of distinct geometrical properties (samples A–D; see Figure 5.2 and Table 5.1) were analyzed by both water contact angle measurements and AFM imaging. In the first test series, static water contact angle on all samples was measured in order to demonstrate the actual fraction of the surface covered with the polymer (see Table 5.1). Put otherwise, in case of a hydrophobic material like Teflon AF, as water cannot fill the defects over the surface, the magnitude of the actual water contact angle (θ^*) can be used to determine the fraction of the

surface covered with the polymer (*f*). In this perspective, by using the Cassie-Baxter equation, $\cos(\theta^*) = f(1 + \cos(\theta)) - 1$ [27], where θ is the water contact angle on a flat Teflon AF surface (*i.e.*, 104°) [25], the percentage surface fraction ($f \times 100$) of each sample (*i.e.*, the fraction of the surface available for contact) was calculated (see Table 5.1 and Figure 5.3).

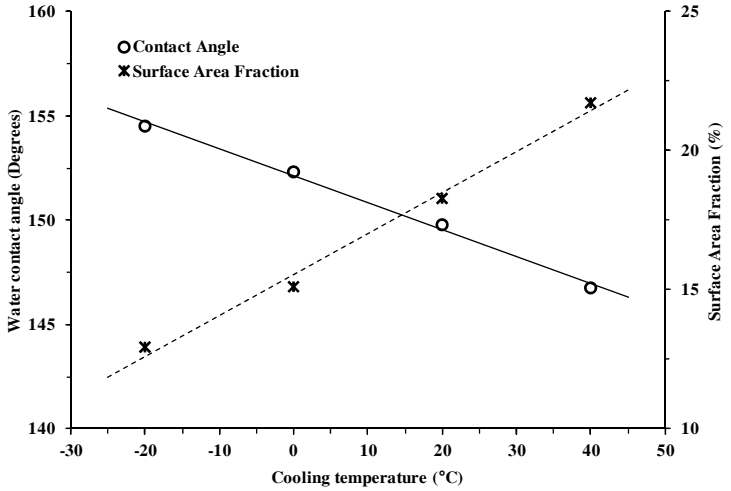

Figure 5.3. Water contact angle and the percentage surface area fraction for bi-level Teflon AF nanopillars of various geometrical properties processed at different cooling temperatures of -20, 0, 20, and 40 ˚C.

As illustrated in Figure 5.3 and Table 5.1, by increasing the cooling temperature from –20 to 40 °C, the percentage area fraction over bi-level Teflon AF nanopillars was enhanced from ~13% for sample A, with the smallest terminating nanolayer feature sizes, to ~21% for sample D with the largest ones. From another perspective, the samples processed at lower cooling temperatures had a smaller area available for contact and vice versa.

Next, in order to look into the roughness of the terminating nanostructure on top of the base nanopillars, AFM tests were performed on all samples (A–D). For the sake of visual clarity,

only amplitude images obtained in the AFM tests are shown in Figure 5.2 (bottom row). But the roughness results reported in Table 5.1 were extracted from the corresponding topography images taken in the AFM tests (see Appendix B for the characteristic topography images). As demonstrated in Table 5.1, samples processed at lower cooling temperatures had typically smaller roughness average (R_a) values in comparison to those processed at higher cooling temperatures. That is, bi-level Teflon AF nanopillars which were processed at smaller T_C values possessed terminating nanolayers of smaller thickness and, most likely, of softer structure, as will be discussed in detail in the upcoming subsection.

It is worthwhile mentioning that the applied novel approach toward changing the topography of the top terminating nanostructure of bi-level Teflon AF nanopillars is crucially relying on the particular design of the setup and, in particular, the presence of a stainless steel (SS) cylinder above the polymer melt (see Appendix B for details on the setup used). More specifically, the cooling source was in contact with the polymer through a 6 cm long SS cylinder. Here, cooling the polymer through such a highly conductive material as SS ($k_{SS} \approx$ 15 W/m.K) [143], which removed the heat from the polymer melt very effectively, energized the instabilities of the advancing precursor films, thus leading to formation of terminating nanolayers of smaller profiles at lower cooling temperatures. It is also worthwhile to mention that the samples processed in ambient conditions (24±1 °C) without the SS cylinder on top (*i.e.*, cooling was carried out by convection through non-flowing air), possessed more of a flat sheet-like nanolayer on top of the base nanopillars (see Appendix B for typical SEM images). That is, it was the effective cooling through the top via the SS cylinder, which

'excited' the instabilities of the advancing polymer precursor film, thus allowing control over the topography of the fluffy terminating nanostructure at the tip of the nanopillars.

5.3.2 Adhesion of Teflon AF nanopillars

To investigate the adhesive properties of the bi-level Teflon AF nanopillars of distinct geometrical properties (samples A–D; Table 5.1), indentation tests were carried out. A characteristic indentation test consisted of pressing a hemispherical fused silica probe (8 mm in diameter) on a sample surface until the normal force reached the desired preload. Following the loading, the probe was pulled up until it completely detached from the sample (unloading). Typical adhesion traces (force vs. displacement) are cited in Appendix B.

The maximum of the normal force detected upon detaching the probe from the samples (the so-called pull-off force) was used to determine their adhesive ability. The pull-off forces detected for flat control samples were expectedly negligible (typically, 0.04±0.02 mN), while they were also independent of the applied preload [29]. The low adhesion of flat Teflon AF samples to the fused silica probe as well as its preload-independency were due to the very small actual area of contact because of the high Young's modulus of the polymer (1.6 GPa) [6,25,29,67]. However, significant pull-off forces were detected for bi-level Teflon AF nanopillars of special geometrical properties. The absolute values of the measured pull-off forces and the corresponding adhesion strengths (*i.e.*, pull-off force per unit surface area),

achieved under various nominal preloads of 5, 10, 25, and 50 mN for nanopillars of various topographical properties (samples A–D), are plotted in Figures 5.4.A and 5.4.B, respectively.

Conventional analysis of the adhesion developed via contact electrification, as the dominant adhesion mechanism in the current system, requires some simplifying assumptions regarding the geometry of the contact. Specifically, to analyze the adhesion in the contact of the fused silica probe and Teflon AF nanopillars charged via CE, the geometry of the system needs to be simplified by considering the two surfaces as two infinite parallel plates; this simplification was applied to the current system as the separation distance (typically < 5 μm) was much smaller than the radius of curvature of the probe (8 mm) and the diameter of the contact area (160–600 μm) [32,107]. Doing so, the pull-off force ($F_{pull\text{-}off}$) generated upon detachment of the probe from the nanopillars can be calculated by Equation 2.14. One should bear in mind that Equation 2.14 is approximate in the sense that it considers no deformation at the surface, and equal and uniform charges over both surfaces. Even so, Equation 2.14 clearly demonstrates that the achieved pull-off force in the current electrostatically-charged system is directly proportional to the – actual – area of contact, and dependent on the power of two of the surface charge density. The influence of the contact area on adhesive properties of Teflon AF nanopillars will be fully discussed shortly. However, the role of the latter factor (*i.e.*, surface charge density) will not be analyzed since measuring the surface charge density in the current system is not feasible and, even if possible, it would have a high degree of uncertainty (error), hence inaccuracy.

Returning to Figure 5.4.B, it can be seen that sample A (processed at T_C = –20 °C) showed very good performance at the lowest applied preload, while beyond that, its efficiency declined considerably. As speculated from the AFM tests and also later evidenced from analysis of the penetration depth of the probe into Teflon AF nanopillars (see Appendix B), sample A had a much softer structure in comparison to other samples. In fact, the very soft structure of sample A led to its efficient performance at the lowest applied preload of 5 mN (where it reached the adhesion strength of ~0.8 N/cm^2). However, it seems that the deformation of the small and soft nanostructure of this sample considerably limited its efficiency under higher pressures (see Figure 5.4.B) [19,53,87]. Typically, in case of fibrillar adhesives, there is a specific preload (the so-called saturation preload) beyond which the efficiency of the dry adhesive starts to decline, because of the reduction in the actual area of contact due to the elevated chance of deformation [19,53,87]. In the case of the electrostatic-based adhesion of the bi-level Teflon AF nanopillars, enhancing the applied load increased the area of contact (see Appendix B), which should have led to much larger pull-off forces at elevated preloads [122]. However, as the soft terminating nanostructure of sample A was vulnerable to deformation under larger pressures, it appears that the performance of sample A weakened at preloads larger than 5 mN because of the decline in the actual area of contact under elevated preloads [19,53,87].

Nonetheless, Figure 5.4.A indicates the superlative performance of both samples B and C (processed at T_C = 0 and 20 °C, respectively); having a relatively more robust terminating nanostructure with larger available area of contact in comparison to sample A (see Table 5.1

and Figure 5.3), samples B and C reached very large pull-off forces even at the higher applied preloads [52,56].

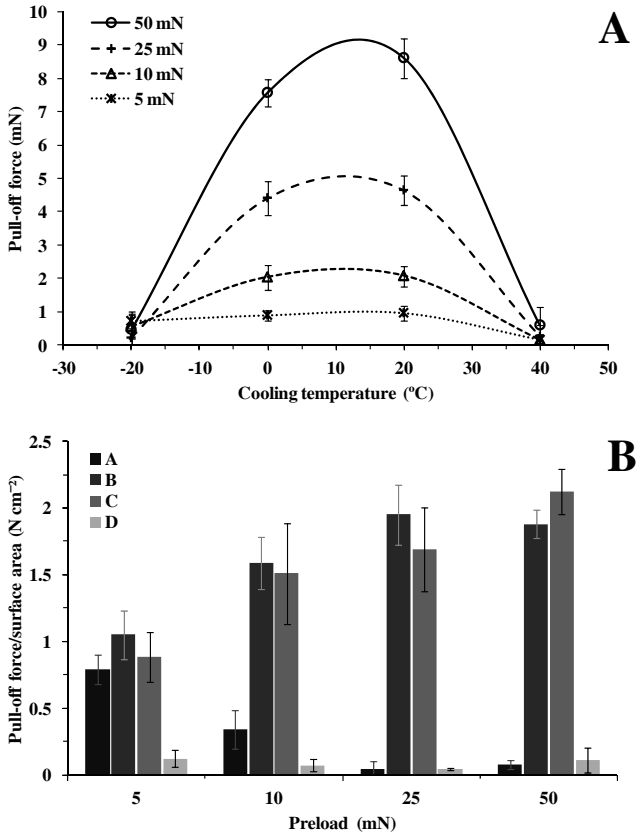

Figure 5.4. Indentation test results. (A) Pull-off force values generated under different preloads (nominally 5, 10, 25, and 50 mN) for bi-level Teflon AF nanopillars processed at various cooling temperatures of -20, 0, 20, and 40 °C (samples A, B, C, and D, respectively). (B) The maximum achieved adhesion strength (pull-off force per unit surface area) at various preloads for samples A-D.

In particular, sample B reached the remarkable adhesion strength of ~1.9 N/cm^2 under the applied preload of 25 mN, while its adhesion strength showed a decline at the highest preload of 50 mN. On the other hand, it seems that in the applied preload range of 5–50 mN, sample C with a relatively denser and more robust fluffy nanolayer, had not reached the saturation preload and, astonishingly, achieved the superior adhesion strength of ~2.1 N/cm^2 (pull-off force = 8.6 mN) at 50 mN preload. Recalling the highest normal adhesion strength that bi-

level Teflon AF nanopillars are achieved thus far (*i.e.*, 1.6 N/cm^{-2}) (see Chapter 4), it can be seen that both samples B and C has performed very effectively in generating strong adhesion forces in normal direction.

However, for the Teflon AF nanopillars of sample D (processed at T_C = 40 °C), negligible pull-off forces were detected under all applied preloads (see Figure 5.4.A). Basically, the advantage of film-terminated fibrillar interfaces over singular fibrillar ones arises from their relatively more robust structure with an enhanced actual area of contact [52,56]. Although these properties contributed toward the striking performance of samples B and C, as discussed earlier, it seems that the denser and, therefore, tougher terminating nanostructure of sample D negatively affected its performance; that is, due to the very rigid structure of the terminating nanolayer of sample D (see Appendix B), its efficient conformal contact with the probe was not feasible, thus leading to the very small adhesion strengths of sample D under all applied preloads (see Figure 5.4.B).

5.3.3 Friction of Teflon AF nanopillars

The next series of tests were load-drag-pull (LDP) tests which were performed to study the frictional properties of bi-level Teflon AF nanopillars of distinct geometrical properties (samples A–D; Table 5.1). In a typical LDP test, the same fused silica probe used in indentation tests was pressed on a sample surface (loading step) until the normal force reached the required preload value of nominally 5, 10, 17.5, and 25 mN. While keeping the

normal force identical to the applied preload, the probe was subsequently dragged over the sample for a 500 μm distance (dragging step). At the end of the dragging track, the probe was instantaneously moved upwards (unloading step) until it completely detached from the surface. The characteristic friction traces (force vs. time) from LDP tests on Teflon AF nanopillars (sample B, processed at T_C = 0 °C) as well as on a flat control sample are plotted in Figure 5.5.A.

5.3.3.1 Dragging step

At the start of the dragging step (in the case of bi-level Teflon AF nanopillars), a rapid substantial decrease in the absolute value of the normal force was detected (see Figure 5.5.A). In fact, the superior compliance of Teflon AF nanopillars in the lateral direction, in comparison to that in the normal direction, resulted in the release and, consequently, a sharp decline in the absolute value of the normal force at the start of the dragging step [68,69]. However, following the drop in the loading force, the normal force was gradually restored back to the original preload as the LDP instrument was operating in the constant-force mode (see Figure 5.5.A). Passing the onset of the dragging and throughout the rest of the dragging path, the friction force fluctuated in a periodic manner due to the characteristic "stick-slip" phenomenon [107,140]. In general, the stick-slip occurs when the adhesive forces surpass the applied lateral force, leading to periodic oscillations of the measured friction force in the course of dragging [107,140]. That is, the adhesion of Teflon AF to the fused silica probe led to a limited local enhancement in the friction force, which was released shortly after the probe moved further across the surface. Finally, it is worthwhile mentioning that the stronger

adhesion of Teflon AF nanopillars in comparison to that of the flat control samples resulted in significantly more pronounced stick-slip behavior of Teflon AF nanopillars, as is evident in Figure 5.5.A.

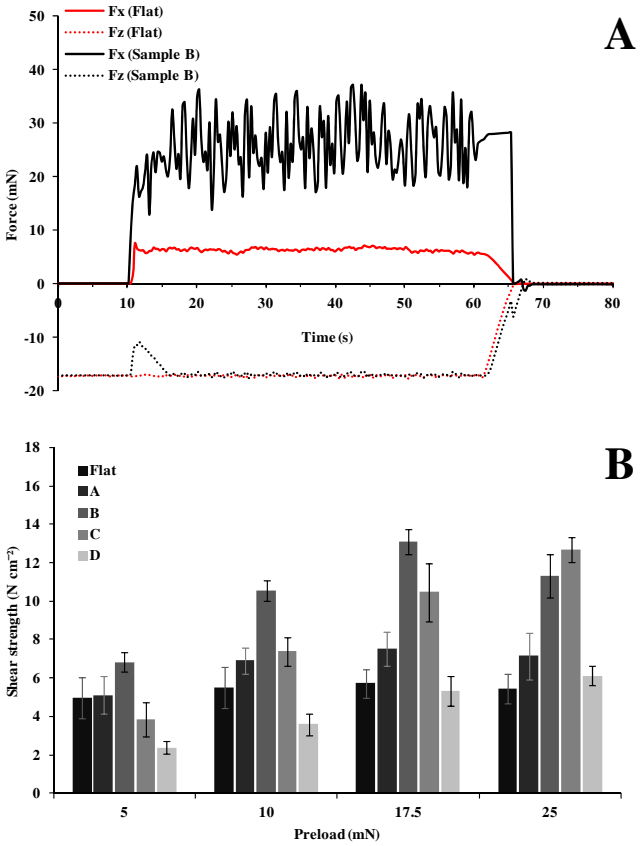

Figure 5.5. LDP test results. (A) Characteristic friction traces (force vs. time) for bi-level Teflon AF nanopillars (sample B; processed at T_C = 0 °C) and a flat control sample; the normal force (F_z) and the friction force (F_x) changes are shown from ~10 s before the start of dragging to ~10 s after the unloading at a nominal applied preload of 17.5 mN. (B) Shear strength (friction force per unit surface area) at the start of the dragging step in LDP tests for the flat control samples and bi-level Teflon AF nanopillars processed at various cooling temperatures of -20, 0, 20, and 40 °C (samples A, B, C, and D, respectively) under nominal preloads of 5, 10, 17.5, and 25 mN.

Returning to the onset of the dragging step, as the decisive spot indicative of the static frictional properties of a dry adhesive, the shear strengths (*i.e.*, friction force per unit surface

area) for bi-level Teflon AF nanopillars (samples A–D) as well as for flat control samples were calculated (Figure 5.5.B). In general and with regard to an effective dry adhesive resembling the frictional adhesion of a gecko toe pad [7], one expects very large shear strengths, higher than the adhesion strength, which assists the strong shear attachment (yet yields easy normal detachment) [90].

As illustrated in Figure 5.5.B, the shear strength developed by flat control samples was almost constant (~5.3 N/cm^2), independent of the applied preload. In general, the friction force (F_x) measured in a LDP test is affected by both adhesive and frictional properties of the surface. In other words, $F_x = S + \mu F_z$ [6], where S is the effective shear coefficient, μ is the Coulomb friction coefficient, and F_z is the applied normal force. In fact, the former term (S) is relying on the interfacial adhesion demonstrating the shear performance of the surface, whereas the latter one (dry friction, μF_z) signifies the load-dependent friction force, which depends on the properties of the bulk material. In this perspective, the shear strength represented in Figure 5.5.B can be defined as $F_x/a_{con} = S/a_{con} + \mu F_z/a_{con}$, where a_{con} is the apparent area of contact. In the case of flat Teflon AF, the first term of the so-called "effective shear strength" ($\tau = S/a_{con}$) is almost zero, because of the rigidity of Teflon AF (Young's modulus = 1.6 GPa) [25] and the negligible actual area of contact [6,67]. On the other hand, the second term ($\mu F_z/a_{con}$) for the flat Teflon AF is constant (~5.3 N/cm^2), since the coefficient of friction is constant (~0.35 for Teflon AF), while the contact area (a_{con}) is a linear function of the normal force (F_z) [29]. Otherwise stated, the shear strength measured

for flat Teflon AF was independent of the applied preload (Figure 5.5.B) since the adhesive properties of flat Teflon AF were not changing with the applied preload [6,67].

However, the shear strengths detected for bi-level Teflon AF nanopillars were significant and preload dependent. For instance, the achieved shear strength for sample A (processed at T_C = –20 °C) at the smallest applied preload was limited and comparable to that of the flat control samples. Unlike the flat control samples, it showed an increasing trend as the preload was enhanced (Figure 5.5.B). In fact, under larger preloads, the area of contact was larger, which led to enhanced electrostatic interactions [107,122]. Teflon AF nanopillars of sample A achieved elevated shear strengths under elevated preloads in that electrostatic interactions (being the major source of adhesion in their contact with the fused silica probe), are an increasing function of the preload. It should be mentioned that not only sample A, but also the rest of the bi-level Teflon AF nanopillars (samples B–D) showed an increasing behavior by enhancing the applied normal force (Figure 5.5.B). However, only for sample A and B, beyond the applied preload of 17.5 mN, did the achieved shear strength slightly decline. The maximum achieved shear strength for sample A and B was ~7.6 and 13.0 N/cm^2, respectively, which both were achieved at the applied preload of 17.5 mN. As already mentioned, for a fibrillar interface, having inferior efficiency beyond a specific preload (the so-called saturation preload) is typical [19,53,87].

Even though sample B also showed the same shear strength saturation as sample A, the denser and more robust terminating nanostructure of sample B has led to its superior shear

strengths (under all preloads) in comparison to sample A [29]. In a broader perspective, the variations in the shear strengths of the fabricated nanopillars (see Figure 5.5.B) were only coming from the difference in their effective shear strength (τ) in that the friction term ($\mu F_z/a_{con}$) was necessarily independent of the applied preload. In this regard, the superior shear performance of sample B, which reached the very high shear strength value of 13.0 N/cm^2, was attributed to the better adhesive properties of this sample in comparison to those of sample A with smaller actual area of contact and significantly softer terminating nanostructure. Even though the achieved adhesion strength of ~13.0 N/cm^2 for sample B was smaller than the remarkable adhesion strength value of ~17.0 N/cm^2 which we reported previously for bi-level Teflon AF nanopillars of special geometrical properties (see Chapter 4), the shear performance of sample B was still significant!

As illustrated in Figure 5.5.A, the next two samples (samples C and D, processed at T_C = 20 and 40 °C, respectively) did not show the sign of preload saturation up to the highest applied preload, in fact due to their relatively denser and, hence, stronger fibrillar structure (see Table 5.1). Even so, under most applied preloads, the performance of these two samples (C and D) was not as striking as that of sample B. This ineffectiveness, which was more pronounced under lower loads, was attributed to their relatively tougher terminating nanostructure which can cause a decrease in compliance under low preloads [29]. However, having the same preload-dependent efficiency as other samples, samples C and D reached remarkable shear strength values under elevated preloads. For instance, sample C reached the quite significant shear strength of ~12.7 N/cm^2 under the nominal preload of 25 mN.

Actually, the efficient and preload-dependent friction of bi-level Teflon AF nanopillars mainly arose from the alignment and compliance of the upper level, as was observed in SEM images taken from the dragging area [23,29,90]. As representatively shown in Figure 5.6, the top terminating nanostructure, as well as the base Teflon AF nanopillars, were entirely aligned in the direction of dragging.

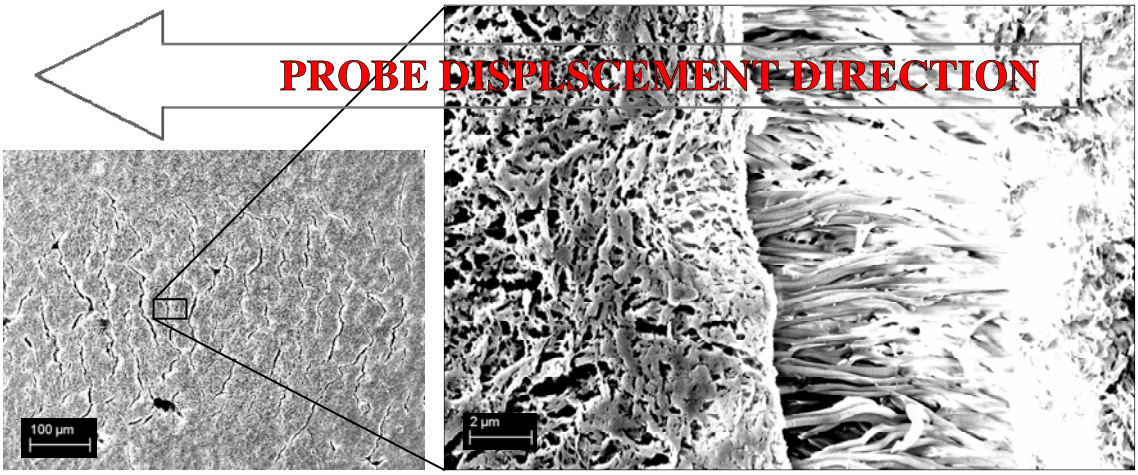

Figure 5.6. Typical SEM images taken after LDP tests carried out on bi-level Teflon AF nanopillars (sample C; processed at T_C = 20 °C) at a nominal preload of 25 mN. The probe was dragged over the nanopillars for a 500 μm distance with the constant speed of 10 μm/s.

The alignment and compliance phenomenon, which was more pronounced under elevated preloads, allowed the intimate contact of the bi-level Teflon AF nanopillars with the probe to generate enhanced shear strengths, particularly under elevated preloads [23,29,90]. In addition to the significant alignment of the nanopillars in the direction of dragging, separation of electric charges in LDP tests through the dragging step is more efficient in comparison to that achieved in indentation tests [31], resulting in accumulation of electric

charges at the interface in LDP tests. In fact, both the alignment phenomenon and effective charge separation through dragging led to the superior performance of bi-level Teflon AF nanopillars in the shear direction in comparison to that in the normal direction (compare Figure 5.4.B with Figure 5.5.B), which is an important advantage for an effective dry adhesive of tailored properties [23,29,90]. That is, the strengths achieved in LDP tests were much larger than those acquired in indentation tests (compare Figure 5.4.B with Figure 5.5.B), which is favorable in the sense that it results in strong shear binding yet easy normal detachment, thus resembling the frictional adhesion of a gecko foot pad [7,23,29,90].

5.3.3.2 Unloading step

As represented for sample B in Figure 5.5.A, at the end of the dragging course and upon unloading the probe from the Teflon AF nanopillars, the absolute value of the normal force increased substantially in a few sudden steps. The rapid increase(s) in the normal force, observed upon unloading the fused silica probe from the bi-level Teflon AF nanopillars in the LDP tests, led to lower pull-off forces for almost all samples in comparison to those achieved in the indentation tests (see Appendix B).

In the representative case of sample B (see Figure 5.5.A), it can be seen that even after ~5 s after the start of unloading, the friction force (F_x) was still constant. However, at a ~5 μm displacement in the normal direction (*i.e.*, 5 s after the start of the unloading step), the absolute value of the normal force (F_z) suddenly jumped up. The sudden overshoot in the

absolute value of the normal force must be because of backflow of electric charges, which accumulated extensively throughout the dragging step, leading to a rapid decline in the adhesion force [31-33]. In general, if the charge densities at two surfaces charged via CE become so high, an electrical breakdown would occur upon their separation across the separating gap, leading to backflow of charges to the original surface [31-33]. However, when the separating gap between the two surfaces is smaller than the mean free path of the electrons in the separating medium (*e.g.*, 0.5 μm for air), discharge will not happen. But, once the separation distance reaches micrometer dimensions, backflow takes place as some of the initiatory electrons are amplified by ionizing collisions with the molecules of the separating medium [32].

As exemplified in Figure 5.5.A, prior to the first drop in the adhesion force, the friction force was almost constant, as the electrostatic force is independent of distance at these length scales [107], while beyond the first drop, the friction force started to decline. Even though measuring the surface charge density throughout the LDP tests was not practically feasible, as discussed earlier, it seems that when the separating gap reached a specific distance, a partial discharge occurred across the separating medium, which led to a sudden drop in the adhesion force and, consequently, a sharp increase in the absolute value of the normal force [31-33]. However, in a way similar to the few studies reported previously on the effect of surface discharge on the adhesion force [31-33], 1–2 more declines in the measured adhesion force and, in turn, drops in the absolute value of the normal force, were observed throughout the rest of the unloading step. These multiple (*i.e.*, 1 to 3) drops in the adhesion force resulted

in detecting lower pull-off forces in the LDP tests (see Appendix B for the pull-off force values measured in LDP tests) in comparison to those measured in indentation tests [31-33]. In general, backflow of electric charges, which in the extreme case may give rise to formation of sparks at the contact zone, would lower the final charge density at the surface and, as a result, the amount of the adhesion force generated between the two surfaces charged via CE [31-33].

5.4 Summary

In this chapter, it has been shown how the height of the fabricated nanopillars as well as the topography of the nanostructure terminating the nanopillars at the tip were simultaneously controlled, by applying a novel fabrication method consisting of the simultaneous heating and cooling of the Teflon AF melt filling vertically-aligned AAO nanochannels. Using this method, bi-level Teflon AF nanopillars of constant height, yet various geometrical properties, were prepared. The changes in the structural and topographical properties of the fabricated dry adhesives were characterized by SEM and AFM imaging as well as by water contact angle measurement tests. Changes in the robustness and surface area available for contact, as achieved by changes in the topographical properties of the top terminating nanostructure, led to significant variations in the adhesive and frictional properties of the fabricated nanopillars, which were investigated further by indentation and friction tests. Indentation and friction test results revealed that the fabricated electrostatic-based dry adhesives can generate enhanced adhesion and friction strengths, up to ~2.1 and 13 N/cm^2, respectively. The unique structural

properties of bi-level Teflon AF nanopillars as well as their remarkable adhesion strengths in both the normal and shear direction make them an ideal candidate for robotic and medical applications. Moreover, the better understanding of the electrostatic-based adhesion of the fabricated dry adhesive can also shed more light on interfacial interactions of other synthetic dry adhesives, which – similar to bi-level Teflon AF nanopillars – may also be affected by electrostatic interactions developed via surface charging [122].

Chapter 6. Polymeric Bio-inspired Dry Adhesives: van der Waals or Electrostatic Interactions?

6.1 Introduction

The decisive influence of CE on adhesive properties of synthetic dry adhesives (SDAs) has been discussed in detail in Chapters 3 to 5, in studies of the performance of bi-level Teflon AF nanopillars. Bi-level Teflon AF nanopillars consisted of extremely high aspect-ratio (AR) nanopillars (200 nm in diameter; up to 45 μm tall) with a fluffy nanolayer of the same material on top. Teflon AF, which was used for fabrication of these bi-level nanopillars, has a very low surface energy of 15.7 mJ/m^2 [25]. In fact, the very low surface energy of Teflon AF, which is usual for a fluoropolymer, is limiting its vdW interactions upon contact, as discussed in the previous chapters. Although Teflon AF is not a proficient vdW interaction generator, like other fluoropolymers, it is able to trap electric charges at its surface upon contact. In addition to its charge trapping characteristic, the charges developed at the surface of Teflon AF cannot transfer into its matrix because of the insulating nature of the polymer, which can be determined from its very low dielectric constant ($\varepsilon_{Teflon\ AF}$ = 1.93, the lowest among any known solid organic polymers) [25].

Having the special electrical properties of the applied polymer in mind, extremely high AR nanopillars with a fluffy nanostructure on top were fabricated, as an electrostatic-based dry adhesive. As discussed in Chapters 3 to 5, the exceptional geometrical properties of bi-level Teflon AF nanopillars made possible the development of an intimate contact with a fused

silica hemisphere (6–8 mm in diameter), which was used as a positively polarizable substrate in adhesion tests. With an intimate contact, efficient charge separation via CE at the interface between bi-level Teflon AF nanopillars and the fused silica probe was obtained. The efficient surface charging in this manner allowed the generation of large electrostatic interactions between Teflon AF nanopillars and the probe, resulting in remarkable normal and shear adhesion strengths (up to ~2.1 and 17 N/cm^2, respectively), even larger than those of a gecko foot pad (1 and 10 N/cm^2, respectively) [2].

In this chapter, the possible influence of surface charging on the adhesive behavior of polymeric SDAs, in general, will be discussed. To do so, significant attention will be paid to the largely neglected electrostatic interactions in adhesion of bi-level Teflon AF nanopillars (as the only so far reported SDA which mainly works based on electrostatic forces). Then, several examples will be given from other SDAs reported in the literature, where surface charging could have played a significant role while its impact was neglected, and their adhesion performance will be discussed accordingly.

6.2 Dry adhesives: van der Waals vs. electrostatic interactions

Amongst various animals and insects which have been used as the prototype in fabrication of SDAs, geckos have indeed received the most attention [15-18,22]. The superior adhesive ability of geckos has been related to the micro/nanoscale hierarchical structure of their foot pads, allowing them to adhere to almost any surface via the weak yet universal vdW forces

[2-5,9,11,80,95,96]. More specifically, it has been argued that vdW interactions loosely adhere each fibril of the toe pads to the substrate that the animal is walking on or clinging to [3]. Although the interaction force generated at the tip of each fibril is very small, the total interaction force generated by the large number of fibrils is very large [2,3], leading to a strong adhesion force at the interface between the substrate and the animal toe pads. It is worthwhile to mention that geckos are the biggest animals with the densest fibril packing of foot pads (~14000 fibrils/mm^2) [3], which use the dry adhesion mechanism for their locomotion [88,144].

With reference to the gecko's dry adhesion mechanism, the adhesion performance of SDAs has been analyzed based on the idea that relatively short-range vdW forces are the most dominant forces ruling the adhesion of dry adhesives [15-18,22]. Even so, one knows that upon contact of any two surfaces, electric charges also separate – up to a certain amount – across the interface between the substrates [30,31,34,37,106], resulting in formation of electrostatic interactions between them [29,32,33,38]. Although occurrence of surface charging is common and it can have a significant impact on interfacial interactions, as discussed in subsections 2.3.2 and 2.3.3, the contribution of CE-driven electrostatic interactions has been conventionally ruled out in design and analysis of SDAs.

6.2.1 Bi-level Teflon AF nanopillars

Regardless of the lack of attention to CE and the crucial role it might have in adhesive behavior of bio-inspired dry adhesives, as discussed in Chapters 3 to 5, we have succeeded in fabricating a dry adhesive, which mainly relies on electrostatic interactions developed through surface charging [29,38,97]. The polymer used for fabrication of the electrostatic-based dry adhesive was a fluoropolymer of remarkably low surface energy (*i.e.*, Teflon AF with surface energy of 15.7 mJ/m^2) [25]. As a matter of fact, the very low surface energy of Teflon AF (which is typical for a fluoropolymer) does not allow the polymer to generate efficient vdW interactions at its surface. For instance, the vdW-driven adhesion force which can be obtained upon intimate contact between Teflon AF and a – 8 mm in diameter – fused silica hemisphere is only about 1.14 or 1.06 mN, according to Hamaker and JKR theories, respectively (see Chapter 4).

Even though Teflon AF is not an efficient vdW interaction generator, this polymer, as a fluoropolymer, has a tendency to become highly charged at its surface upon contact, allowing that to generate electrostatic interactions through CE. However, generating strong electrostatic interactions by trapping large amounts of electric charges at the surface of any material, including Teflon AF, requires that the surface comes into an intimate contact with the substrate touching that. In this regard, extremely high AR nanopillars (200 nm in diameter) with a unique fluffy nanostructure on top were developed on Teflon AF. Applying a novel fabrication technique, base nanopillars were terminated at the tip with an exceptional fluffy nanostructure of the same material. The special geometrical properties of bi-level Teflon AF nanopillars allowed the formation of the intimate contact which is necessary for

the occurrence of efficient surface charging. Doing so, bi-level Teflon AF nanopillars of 80 μm height, for instance, succeeded in generating pull-off forces as large as 100 mN, which is almost 100 times larger than those obtainable through vdW interactions. Upon contact of Teflon AF nanopillars with the adhesion testing probe, electric charges transferred across the contact interface. The transfer of electric charges was followed by separation of some charges between the dry adhesive and the probe upon their detachment. Eventually, separation of electric charges at the interface led to strong electrostatic interactions and therefore, large adhesion forces between the nanopillars and the probe.

In addition to the surprisingly large magnitude of the developed pull-off forces, what is also very important in the adhesive behavior of Teflon AF nanopillars is the trend of changes of pull-off forces that were generated by varying the applied load on the dry adhesive. More specifically, it was observed that by increasing the applied load, adhesion forces achieved by the fabricated dry adhesive increased almost linearly (see Figure 4.1). The load-dependent behavior in contact of bi-level Teflon AF nanopillars was anticipated, since load-dependency is a common behavior for an electrostatic-based system. To be more specific, according to the simple capacitor model (subsection 2.3.2.2; Equation 2.14), increasing the area of contact should lead to a linear enhancement in the electrostatic interaction force that a surface can develop via surface charging. Hence, in case of the contact between bi-level Teflon AF nanopillars and the adhesion testing probe, it was observed that by increasing the applied load (which increased almost linearly the apparent area of contact), the pull-off force obtained by the dry adhesive increased linearly as well.

As a matter of fact, adhesion of bi-level Teflon AF nanopillars encompasses the two main trademarks of electrostatic-based systems, which are large pull-off forces plus area-dependency of their adhesion, as described in detail in subsection 2.3.3. However, it should be noted that the dry adhesive fabricated from Teflon AF is not the only one of its kind showing such behavior in adhesion tests. There are other SDAs which have shown the same characteristics (*i.e.*, large pull-off forces plus area-dependency of adhesive performance) in their adhesion tests [8,54-57,63,145-148]. In the literature, this seemingly irregular behavior of namely vdW-based dry adhesives, which do not conform to the general traits of a vdW-based system (see subsections 2.3.2 and 2.3.3), has been explained by theories that will be briefly discussed in the next subsection.

6.2.2 van der Waals-driven adhesion of dry adhesives

Conventionally, it has been assumed that adhesion of SDAs comes from vdW interactions. Even so, it has also been reported that some dry adhesives can generate extremely large adhesion forces beyond the limits of vdW forces [53,57,63,147]. These unusually large adhesion forces generated by several dry adhesives were explained by the so-called "contact splitting" theory [8]. To look into the details of this model, the characteristic contact between a hemisphere of radius R and a flat surface needs to be considered. The magnitude of the adhesion force between the hemisphere probe and the flat surface (F_{vdW}) can simply be determined by the JKR model (Equation 2.12), by considering the vdW forces as the only

dominant interfacial forces at the contact zone. Now, assuming that the flat surface is split up into n sub-surfaces (*i.e.*, pillars), each with radius of R^2/n (self-similar scaling), it can be considered that each pillar is acting as an individual substrate. Doing so, the total adhesion force ($F_{pull\text{-}off}$) obtainable by the pillars would be larger than that expected from the JKR model for the flat surface (*i.e.*, F_{vdW}), and its magnitude can be estimated from [8]

$$F_{pull-off} = \sqrt{n}\, F_{vdW}$$

Equation 6.1

Equation 6.1 simply describes how a fibrillar pattern with a large number of contacts (n) can lead to an increase in the observed adhesion force in comparison to the corresponding flat surface.

Besides the contact splitting approach, the superior adhesion of fibrillar structures in comparison to that of flat surfaces has also been explained by comparing the adhesive behavior of SDAs with that of regular pressure-sensitive adhesives (PSAs), such as Scotch tapes [80]. It is known that PSAs can generate comparatively large adhesion forces because of the large effective work of adhesion (γ_{eff}) which they can generate upon contact, outperforming the vdW-driven interface energy (γ) [80]. The large obtainable effective work of adhesion by PSAs is mostly – but not solely – due to the chance of elongation of the soft polymeric layer of PSAs, which allows the development of long-range interactions with the contacted substrate (see Figure 6.1.A). The developed long-range interactions from stretching of the polymeric strings of the PSA basically result in the enhancement of the crack

propagation energy and eventually, the development of large effective interfacial energies (γ_{eff}) [80].

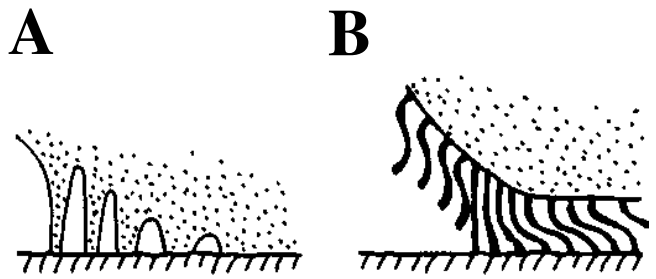

Figure 6.1. (A) Breaking an adhesion junction between a PSA and a hard solid substrate. The stretching of the soft polymeric layer of the PSA allows the formation of long-range interactions between the adhesive and the substrate, leading to generation of an effective work of adhesion (γ_{eff}), much larger than that obtainable solely through vdW interactions (*i.e.*, γ). (B) Detachement of a fibrillar dry adhesive from a hard solid substrate. Resembling the soft feature of PSAs, stretching of the fibers of the fibrillar adhesive leads to developement of extremly large effective work of adhesion (γ_{eff}) by the dry adhesive, significantly outperforming the adhesion forces attainable through vdW interactions (*i.e.*, $\gamma_{eff} \gg \gamma$) [80].

Resembling the adhesive behavior of PSAs, the dry adhesion of fibrillar adhesives has also been related to the elongation of their fibrils upon detachment (Figure 6.1.B), leading to strong adhesion forces that an effective dry adhesive can generate [80,95]. When a substrate is brought into contact with a dry adhesive, the dry adhesive fibrils bend and deform – elastically – to conform to the surface of substrate in contact. Doing so, a certain amount of energy would be stored in the fibrils. The strain energy gained by fibrils basically becomes part of the "cohesive energy" of the system, which would be dissipated throughout dynamic debonding of the substrate from the dry adhesive. Put otherwise, each fibril on the dry adhesive behaves as a long-range cohesive bond (see Figure 6.1.B). Having the ability to develop long-range interactions, it has been developed that an effective fibrillar dry adhesive

can generate an effective work of adhesion (γ_{eff}) much larger than the vdW-driven interface energy (γ) [80,95].

In addition to the unusually strong adhesion, another deviation in behavior of namely vdW-based SDAs from the general concepts of vdW interactions has also been observed. In particular, it was reported that the pull-off forces obtained by some dry adhesives showed an improving trend by increasing the area of contact [8,54-57,63,145-148]. The best representative example in this connection is certainly the single-/multi-level milli-/micro-pillars fabricated from PU by Murphy *et al.* [63] (see Figure 6.2).

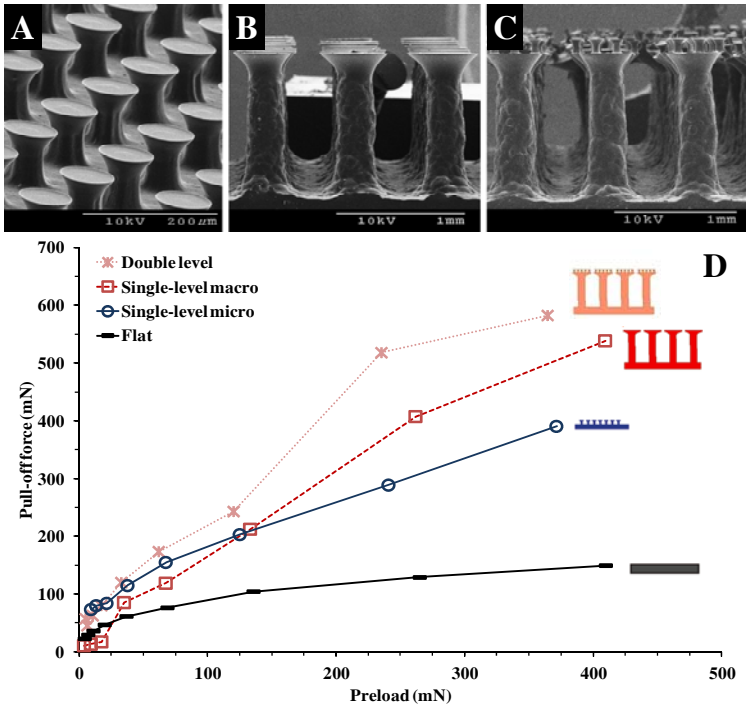

Figure 6.2. SEM images of fibrillar structures fabricated from PU. (A) Single-level micro-pillars; (B) Single-level macro-pillars; (C) Double-level pillars. (D) Pull-off forces vs. preload for various fibrillar patterns as well as for flat control samples [63].

The adhesion performance of their various samples as well as that of the flat control samples were studied by indentation tests, using a 12 mm diameter glass hemisphere as adhesion testing probe. As illustrated in Figure 6.2.D, it was observed that the magnitude of the pull-off force, which the fibrillar patterns could generate at higher preloads (where the area of contact is larger), was larger than what they could generate at smaller preloads [63].

As discussed in subsections 2.3.1 and 2.3.3, it is expected from any vdW-based system, like the SDAs shown in Figure 6.2, that the adhesion force generated be independent of the area of contact, and accordingly independent of the applied preload. The improved performance of dry adhesives, in general, can be explained in line with the contact splitting model which was described earlier in this subsection. More specifically, according to the contact splitting model, the adhesion forces obtainable under elevated preloads should be larger in that, under larger preloads, the number of pillars in contact (*i.e.*, n) is higher. For instance, considering that under a preload f_1, the number of pillars in contact is n_1, then, the obtainable pull-off force between the dry adhesive and the hemispherical probe ($F_{pull\text{-}off}$) would be equal to $(n_1)^{1/2}(F_{vdW})$. However, if the preload is raised to f_2 ($f_2 > f_1$), then the number of pillars in contact would be n_2, which is larger than n_1 (*i.e.*, $n_2 > n_1$). Being so, the obtainable pull-off force in the latter case would be equal to $(n_2)^{1/2}(F_{vdW})$, which is larger than the pull-off force obtained under the smaller preload f_1 (*i.e.*, $(n_1)^{1/2}(F_{vdW})$). In general, the contact splitting model simply indicates that by having a larger number of pillars in contact under elevated preloads, the adhesion force obtainable by a dry adhesive would be accordingly larger. This

is more or less the way that improved performance of dry adhesives is described in the literature.

To this end, surpassing the vdW limits of adhesion by fibrillar adhesives as well as the improvement of their performance under elevated preloads were briefly discussed according to existing theories which are conventionally based on mechanics and the geometry of the system. However, it is worthwhile recalling that these two types of behavior of SDAs, which have been repeatedly observed in adhesion tests on polymeric dry adhesives [8,54-57,63,145-148], are basically the trademarks of electrostatic-based systems. So, knowing that polymeric SDAs are naturally efficient electric charge trappers, as discussed earlier, is it not reasonable to state that the large adhesion and load-dependency in adhesive behavior of SDAs can be – partly, or even entirely – due to their surface charging upon contact? This is the question which will be addressed in the following subsection.

6.2.3 Bio-inspired dry adhesives and contact electrification

How does each fibril of a polymeric dry adhesive adhere to the substrate in contact? To this day, this question is always answered by "vdW forces". But then, why is the effect of "electrostatic forces" which can be generated through surface charging normally neglected in analyzing the bonding of dry adhesive fibrils? One of the main reasons for ignoring the effect of CE in these systems is perhaps the common perception that "the amount of charges which may develop upon contact is very small and so, the effect of surface charging on interfacial

interactions is negligible". As a matter of fact, the first part of this broad assumption is somehow correct! For instance, if nonconductive polymers, which are used in fabrication of SDAs, are brought into contact with another material (and even themselves), typically, surface charge densities in the range of 10^{-5}–10^{-3} C/m^2 develops over their surface (see Table 6.1). Certainly, the reported surface charge densities, which are basically equivalent to 1 electric charge per 12–127 nm^2, are very small. However, what is wrong about the abovementioned statement is that "the effect of surface charging on interfacial interactions of SDAs is NOT negligible". In fact, what has not been taken into consideration in observing the effect of CE on interfacial interactions of SDAs is the fact that formation of strong electrostatic interactions via surface charging, in general, does not necessarily require large amounts of charges to separate upon contact. For instance, the surface charge densities which developed the surprisingly large adhesion strengths of 6.6–8.8 J/m^2 between silica and mica in the Horn and Smith [32] experiments were only 5–20×10^{-3} C/m^2 (~1 electric charge per 8 to 32 nm^2) [32]. So, observing that polymers which have been commonly used in fabrication of dry adhesives can obtain charge densities, more or less, in the same scale (see Table 6.1), it is expected that electrostatic interactions – coming from surface charging – have a much larger impact on the interfacial interactions of polymeric SDAs.

As a matter of fact, although the reported charge densities for polymeric materials (*i.e.*, 10^{-5}–10^{-3} C/m^2) seem small, they are still large enough to generate values of work of adhesion as large as 0.56 mN/cm^2 to 5.6 N/cm^2, according to Equation 2.14.

Table 6.1. Surface charge density for various insulating materials. The numbers cited show the net surface charge densities reported in the literature, while it is expected that local charge densities – even 3 orders of magnitude – larger than these values are formed in micro-/nano-sized domains. The net surface charge density that an insulator can acquire upon contact is typically in the range of 10^{-5} to 10^{-3} C/m^2. However, in cases where surface charging is present through vigorous rubbing, surface charge densities even in the order of 10^2 C/m^2 can be obtained [122].

Material	Substrate	Type of contact	Sign of charge	Charge density [C/m^2]
PDMS	*PDMS*	Intimate-sliding	+/–	0.5×10^{-5}
	PDMS	Intimate	+/–	$\sim 0.5 \times 10^{-5}$
	PDMS	Intimate, in argon	+/–	0.5×10^{-5}
	PDMS	Intimate, in air	+/–	0.3×10^{-4}
	PTFE	Intimate-sliding	+	0.1×10^{-4}
	PTFE	Intimate	+	$\sim 0.8 \times 10^{-5}$
	PC	Intimate-sliding	–	0.2×10^{-4}
	PC	Intimate	–	$\sim 0.2 \times 10^{-4}$
	PVC	Intimate	Not indicated	$\sim 0.7 \times 10^{-4}$
	Stainless Steel	Intimate	Not indicated	$\sim 0.6 \times 10^{-4}$
	Silicon wafer	Intimate	+	$\sim 0.25 \times 10^{-4}$
PC	*PDMS*	Intimate-sliding	+	0.2×10^{-4}
	PDMS	Intimate	+	$\sim 0.2 \times 10^{-4}$
	Various metals	Rolling	+/–	$0.1\text{-}1 \times 10^{-3}$
Polyethylene (PE)	*Mercury*	Intimate	–	$0.1 \times 10^{-4}\text{-}0.2 \times 10^{-3}$
PP	*PP*	Intimate	+/–	0.2×10^{-5}
PS	*PS*	Intimate	+/–	0.9×10^{-5}
	Mercury	Intimate	–	$0.3 \times 10^{-4}\text{-}0.3 \times 10^{-3}$
PVC	*PVC*	Intimate	+/–	$0.3\text{-}0.9 \times 10^{-5}$
	PTFE	Intimate-sliding	+	0.2×10^{-4}
PTFE (Teflon)	*PTFE*	Intimate	+/–	0.5×10^{-5}
	PDMS	Intimate-sliding	–	1.0×10^{-5}
	PDMS	Intimate	–	$\sim 0.8 \times 10^{-5}$
	Nylon 6-6 (polyamide)	Sliding	–	0.2×10^{-4}
	PVC	Intimate-sliding	–	0.2×10^{-4}
	PMMA	Rubbing	–	$\sim 0.1 \times 10^{1}$
	Mercury	Intimate	–	$\sim 1.0 \times 10^{-4}$
Teflon AF	*Fused silica*	Rubbing	–	$\sim 0.8 \times 10^{2}$
Glass	*Stainless Steel*	Rolling	+	0.3×10^{-4}
	Stainless Steel	Intimate	+	0.1×10^{-3}
	Gold	Intimate	+	1.0×10^{-4}
	Aluminum	Intimate	+	0.1×10^{-3}
	Graphite	Intimate	+	0.15×10^{-3}

*SAM: Self-assembled monolayer

The achievable adhesion strengths through surface charging over polymers are actually very large, given that they are even comparable to the surprisingly large adhesion strengths that gecko foot pads can generate (*i.e.*, 1 and 10 N/cm^2 in normal and shear directions, respectively) [2]. So, it is neither logical nor practical to simply exclude the effect of surface charging in the analysis and design of dry adhesives, particularly those made from non-conductive polymers.

As already mentioned, polymers which are employed for fabrication of SDAs can acquire typical surface charge densities in the range of 10^{-5} to 10^{-3} C/m^2 (see Table 6.1). However, it should be noted that using (rather blindly) the reported charge density values for analyzing the adhesion of SDAs might not be such a good idea. The reported charge densities in Table 6.1 are only reflecting the magnitude of the net surface charge densities but not the local charge densities, which can be even much larger than the cited numbers [35]. In other words, it is known that in contact between two surfaces, one surface develops a net negative charge while the other acquires a net positive charge. However, surface charges developed through CE over polymers are not distributed homogenously over the surface. In contrast, each substrate supports a combination of both positive and negative charges, which are spatially distributed in local regions of micro-/nano-scales (see subsection 2.3.2 for more details) [35,49,106,124]. In fact, locally-charged micro-/nano-domains sustain much larger charge densities (even 3 orders of magnitude larger) than the values reported throughout many years as net surface charge densities [35], such as those detailed in Table 6.1. Hence, noting that fibrillar structures have also been fabricated – more or less – in similar micro/nanoscales, one

expects that local forces that each fibril (on a dry adhesive) is dealing with (because of large local charge densities) should be even larger than the forces obtainable from electrostatic interactions of flat substrates (again, see subsection 2.3.2 for details).

All in all, justifying the exclusion of CE in studies on adhesion of polymeric dry adhesives is indeed more difficult than accepting its presence. But again, why, despite all these facts, have surface charging (and the crucial impact it might have on contact of SDAs) been taken lightly thus far? The answer to this question is certainly related to the shortcomings of both theory and technique (as illustrated in subsection 2.3.2.4), which have "hidden" the occurrence of CE and its consequences from scientists who are designing and analyzing bio-inspired dry adhesives. So, maybe now it is time to look for both theoretical models and experimental techniques to clarify further the undisputed occurrence of surface charging, and its influences on performance of bio-inspired dry adhesives.

6.3 Summary

In this chapter, we set out to clarify an important question about polymeric bio-inspired dry adhesives: Is adhesive performance due to van der Waals or electrostatic interactions? In doing so, examples were given along with observed facts not only from the literature but also from our recent work on bi-level Teflon AF nanopillars. It is evident from the literature at large that the contributions of electrostatic interactions, which develop through surface charging, have received little attention in the design and analysis of synthetic dry adhesives.

This lack of attention is mostly due to the shortcomings in fundamental understanding of the mechanism and properties of contact electrification over insulators (particularly non-conductive polymers, which, paradoxically, have been widely used for fabrication of dry adhesives). As a matter of fact, the main requirement for quantifying the occurrence of surface charging over dry adhesives is an accurate apparatus which could measure the amount of charges – that separate over fibrillar structures upon contact – in parallel to changes in interfacial forces both through and after contact. Doing so, a theoretical model which can accurately make a distinction between the contributions of van der Waals interactions and those of electrostatic interactions coming from contact electrification may be obtained.

Chapter 7. Role of Contact Electrification and Electrostatic Interactions in Gecko Adhesion

7.1 Introduction

Geckos, who are capable of walking on walls and hanging from ceilings with the help of micro/nanoscale hierarchical fibrils (setae) on their toe pads [2,5], have become the prime prototype in the design and fabrication of fibrillar dry adhesives [16,17]. Since the unique fibrillar feature of the toe pads of geckos allow them to develop a large actual area of contact with the substrate the animal is walking on or clinging to [2,5], it is expected that the toe setae exchange significant numbers of electric charges with the contacted substrate. Usually, when any two materials, similar or dissimilar, touch each other, electric charges are transferred from one to the other, leading to formation of a net negative charge on one substrate and a net positive one on the other [30,31,34]. Development of an electrical double layer (EDL) [149] at the contact interface via this contact electrification (CE) phenomenon (also known as surface charging) [30,31], essentially gives rise to formation of electrostatic interactions between the charged objects [32,33]. In this chapter, by measuring the magnitude of the electric charges – together with the adhesion forces – that gecko foot pads develop in contact with different materials, the occurrence and effectiveness of CE and electrostatic interactions arising from it in gecko adhesion have been clarified for the first time. Better insight in the role of CE in gecko adhesion is not only very important for understanding of

the principles of the supreme adhesion of these animals, but also is fundamentally very crucial in the design and fabrication of synthetic gecko-inspired dry adhesives, which we have hypothesized to be largely affected by CE-generated electrostatic interactions (see Chapter 6).

7.2 Experimental

Teflon AF 1600, a tetrafluoroethylene (TFE) (35 mol%) and 2,2-bistrifluoromethyl-4,5-difluoro-1,3-dioxole (PDD) (65 mol%) copolymer, was purchased from DuPont. Polydimethylsiloxane (PDMS), received as a two-part Sylgard 184 Silicone Elastomer Kit with base to catalyst mix ratio of 10:1, was acquired from Dow Corning. Fluorinert Electronic Liquid FC-40 for dissolving Teflon AF was obtained from 3M and ethanol (ACS reagent, ≥99.5%) was purchased from Sigma. Ultra-smooth, mirror-finished copper sheets (99%, 28 gauge, 15×15 cm^2), which came coated with a plastic layer to protect them against scratches and possible surface oxidation, were obtained from Fire Mountain Gems and Beads. After cutting the copper sheets into smaller (~5×5 cm^2) pieces, and in preparation for spin-coating the polymer thin films over them, the protective plastic layers on the copper sheets were removed. Then, each sheet was cleaned individually using a commercial metal cleaner (Autosol Metal Polish from Autosol LLC.), followed by sonication in pure ethanol for 40 min using B1500A-MT Ultrasonic Cleaner (VWR International, LLC.). The sheets were finally rinsed with ethanol and, to prevent their oxidation in air, they were kept in ethanol prior to coating them with the polymers.

The polymer thin films were spin-coated onto the copper sheets (~5×5 cm^2) using polymer precursor solutions and a G3–8 Spin Coater (Specialty Coating Systems, Inc.). The corresponding polymer precursor solution, spin speed (ω), and spin time (t) at which the polymer thin films were deposited, are detailed in Table 7.1.

Table 7.1. The corresponding solvent, concentration (C), spin speed (ω), and spin time (t) for fabrication of each polymer thin film as well as the ultimate thin film thickness (h_i) and roughness average (R_a) of each thin film.

Polymer	Solvent	C (wt%)	ω (rpm)	t (s)	h_i (μm)	R_a (nm)
Teflon AF	FC-40	4	1500	30	1.2±0.1	0.1±0.2
PDMS	—	—	6000	60	7.0±0.1	0.5±0.2

After spin-coating, the polymer substrates were annealed for 2 h at 92 °C under vacuum. Annealing under these conditions ensures complete drying of Teflon AF thin films. The polymer substrates were then stored in ambient conditions for a week prior to conducting adhesion and charge measurement tests on them. The storage in ambient conditions was done to ensure that the PDMS was completely cured. The annealing under vacuum was followed by curing at ambient conditions. This was done to both polymer substrates so that the sample preparation was identical for both polymers.

The thicknesses of the polymer thin films (see Table 7.1) were measured by thin film step height measurements from ~1 cm off the edge of the copper sheets using a P-6 Stylus Profiler (KLA-Tencor Corporation). Roughness of the backing copper sheet, as well as of the

polymer thin films (see Table 7.1), were determined by atomic force microscopy (AFM) from a 5×5 μm^2 area from the substrate (Figure 7.1) using a Dimension Icon Atomic Force Microscope (Bruker Corporation) in the tapping-mode.

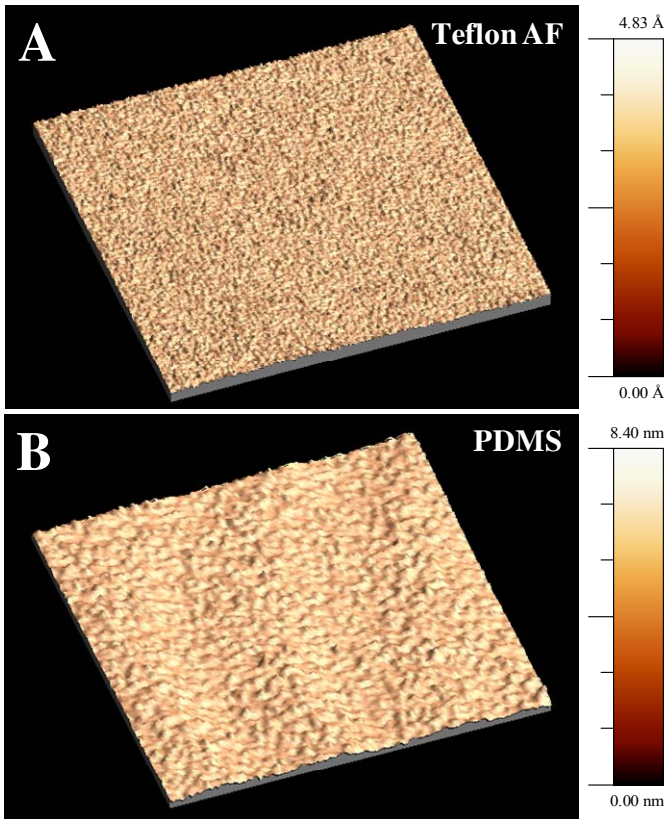

Figure 7.1. Characteristic AFM images taken from a 5×5 μm2 area from (A) Teflon AF and (B) PDMS.

The tip used for AFM imaging was a silicon tip on a nitride lever (ScanAsyst; thickness: 650 nm; length: 115 μm; width: 25 μm), obtained from Bruker Corporation. Analysis of AFM images to obtain the roughness average (R_a) values of the substrates (see Table 7.1) was carried out using WSxM software (Nanotec Electronica S.L.). Each R_a value cited in Table

7.1, including the R_a for the backing copper sheet (=9.7±1.1 nm), is the average value determined from three independently replicated tests, with the deviations corresponding to the standard deviation. As a matter of fact, the measured roughness values are similar and are in the range of roughness at which gecko adhesion is fully functional [105,150].

Polarity characteristics (hydrophobicity and hydrophilicity) of the polymer thin films were determined by measuring the static contact angle of water on them using a home-built set-up. For the water contact angle measurement test, a water droplet (~30 μL in volume) was placed on the polymer thin film at a rate of 15 mL/min. An image of the water droplet was taken from the side, ~20 s after the water droplet was completely deposited onto the sample (Figure 7.2). The static contact angle of each water droplet was then measured by analyzing the captured image using a MATLAB code. Each reported water contact angle result represents the average from six individual and independently replicated experiments along with the standard deviation.

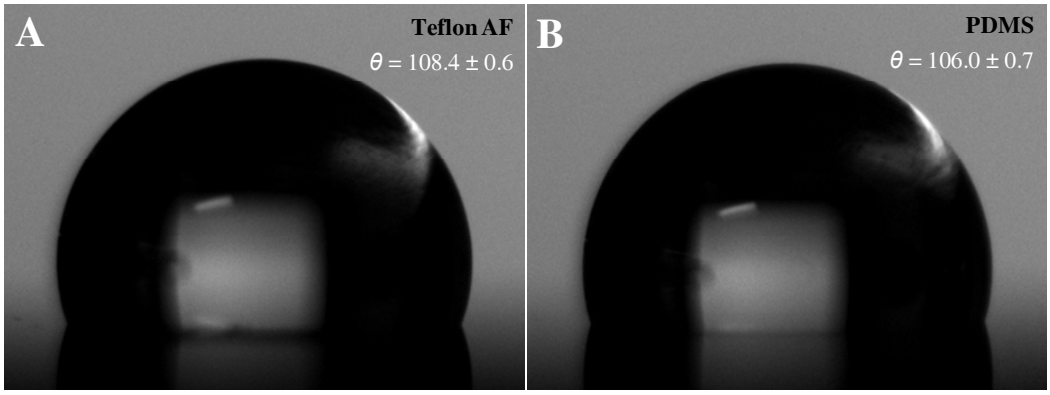

Figure 7.2. Characteristic images of a ~30 μL water droplet, taken from the side, ~20 s after the water droplet was completely deposited onto (A) Teflon AF and (B) PDMS thin films.

To electrically isolate the polymer-coated copper sheets from the surroundings, each sheet was glued to a thick polytetrafluoroethylene (PTFE, Teflon) sheet (6×3.5×0.6 cm^3, L×W×H) using an ethyl cyanoacrylate-based glue (Krazy Glue Corp.) and dried under vacuum at ambient temperature for two hours. The PTFE sheet under the copper sheet was fit into a PTFE plate to provide a frictionless platform for adhesion tests (Figure 7.3). The whole set-up was then mounted on a ~1 cm thick wood plate which was mounted vertically on a wall.

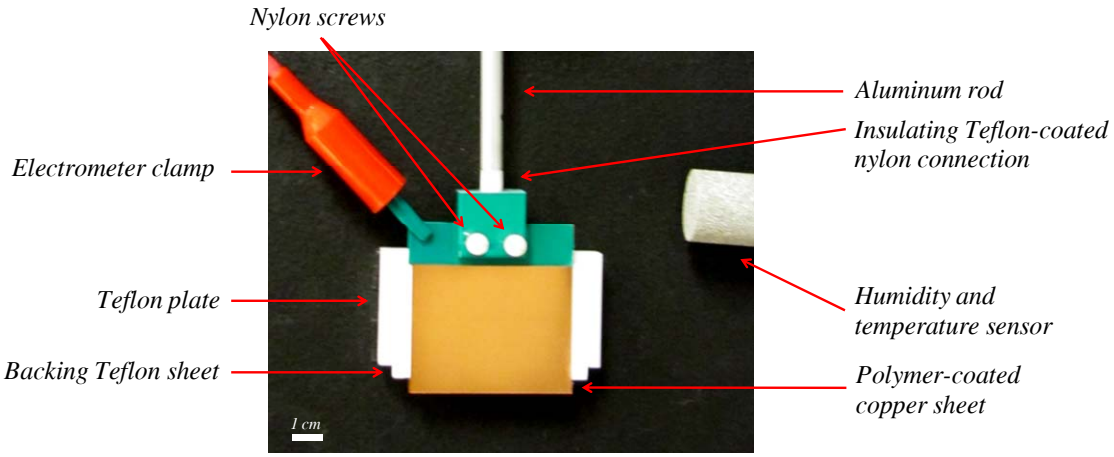

Figure 7.3. The image of the set-up used for *in-situ* adhesion/force measurements. The whole set-up was mounted on a black wood plate, fixed vertically on a wall.

Details on the length, weight, and size of the foot pads of all the five Tokay geckos employed in this research are outlined in Table 7.2. The area of the gecko toe pads was measured by scanning the animal toe pads on a HP Deskjet F4480 All-in-One Scanner/Printer (Hewlett-Packard Development Company) and subsequently measuring the contact area using ImageJ software from National Institutes of Health. All experiments on animals in this research were conducted in compliance with Animals for Research Act of Ontario (Revised Statutes of

Ontario), the Guide to the Care and Use of Experimental Animals from Canadian Council on Animal Care, and the University of Waterloo's Guidelines for the Care and Use of Animals in Research and Teaching.

Table 7.2. Weight, length, and toe pad area of the geckos employed. The pad areas were estimated from analyzing three different scans of the animal toe pads while the deviations correspond to the standard deviations.

Animal number	**Weight** (g)	**Length** (cm)	**Front toe pad area** (mm^2)	**Back toe pad area** (mm^2)
1	55	25	84±4	109±5
2	36	25	83±4	102±5
3	27	23	70±2	85±5
4	48	25	105±5	142±3
5	50	26	121±3	149±3

Before performing adhesion and charge measurement tests, both of the polymer thin films, as well as the gecko foot pads, were grounded to remove any static charge which may have built up on them. Discharging the polymer thin films was carried out by using an Anti-Static Static-Away Brush (Ted Pella, Inc.) to obtain a completely clean and electrically neutral substrate. To remove any previously adsorbed water from the polymer thin films (*i.e.*, water that adsorbed after fabrication of the thin films and before performing the tests), they were rinsed with ethanol and allowed to air dry for a few minutes prior to discharging, before the tests were conducted. The gecko foot pads, on the other hand, were discharged by placing the foot pads on a large polished copper sheet that was grounded to a metal desk. Since the gecko's body is also electrically conductive, throughout both charge and adhesion measurements, the gecko's body itself was also grounded through one of its foot pads (opposite to the foot on which the test was being performed) using a grounded wire; for

instance, when a test was carried out on the right-front leg, the left-back leg was grounded. Experiments were carried out on both front and back legs. The charge and force measurement results were processed and analyzed using Principal Component Analysis (PCA) on STATISTICA from StatSoft Inc.

7.3 Results and discussion

Adhesion and charge measurements were carried out on two substrates, Teflon AF and polydimethylsiloxane (PDMS). Charge and force measurements were performed simultaneously by putting a single foot pad of five live Tokay geckos (*Gekko gecko*) against a vertically-aligned thin film of the polymer, which was coated on a 5×5 cm^2 ultra-polished (roughness average, R_a = 9.7±1.1 nm, n = 3), mirror-finished copper sheet. The foot pad was subsequently pulled down the polymer thin film, dragging the toes across the substrate, until the developed shear force on the polymer was saturated. At the end of the course of dragging, the foot pad was pulled upward (perpendicular from the polymer surface), in order to detach the toes from the substrate. The five steps of the adhesion tests are shown in Figure 7.4.A, while the characteristic adhesion traces for Teflon AF and PDMS are plotted in Figure 7.4.B and 7.4.C, respectively. The static adhesion strength (*i.e.*, adhesion force per unit pad area) over Teflon AF – which was determined at the point where the toes started to slide – was 2.3±0.3 N/cm^2 (n = 10), on average, more than twice as large as that of PDMS (1.1±0.2 N/cm^2, n =10) (Figure 7.4.D). Following the onset of the sliding on both substrates, however, the shear strength increased. Enhancement of the shear strength during dragging is because of

the directionality of the adhesion of gecko toe pads [2,7], considering that they develop a superior contact when the toes get aligned in the direction of dragging (compare Figure 7.4.A-2 with 7.4.A-3). Due to the familiar stick-slip phenomenon [107,140], on the other hand, the increase of the shear strength throughout the dragging step happened in a fluctuating manner.

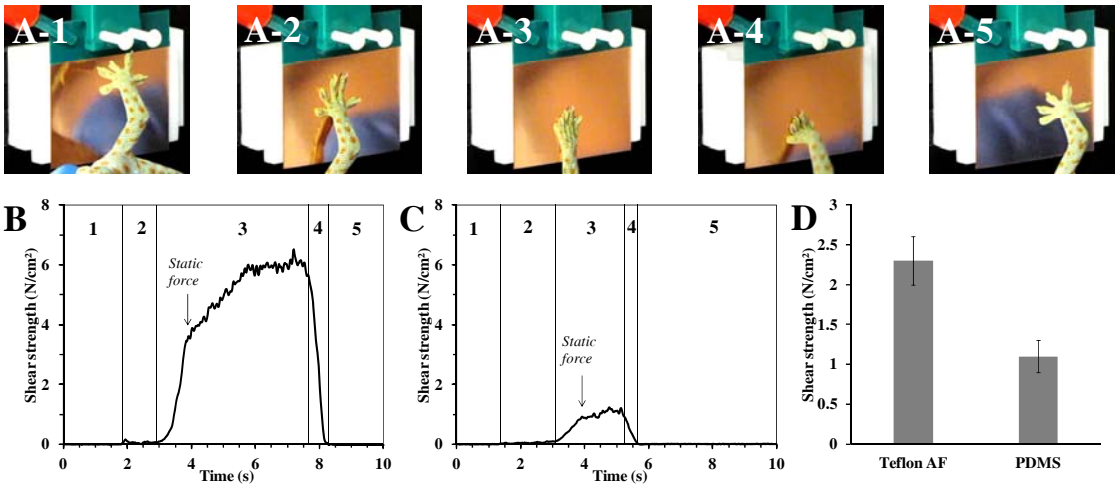

Figure 7.4. (A-1) An originally neutral gecko foot pad was brought close to a vertically-aligned polymer thin film which was coated on a ~5×5 cm^2, mirror-finished, copper sheet. (A-2) The toe pad was placed on the polymer thin film and the surface charge density was measured. (A-3) The foot was pulled down and the toes were dragged over the polymer thin film for a 2-10 mm distance, depending on the type of the polymer. (A-4) Finally, the foot was pulled up – perpendicular from the thin film – until (A-5) the toes completely detached from the substrate. Characteristic changes in the shear strength (*i.e.*, shear force per unit toe pad area) throughout all 5 steps of the in-situ force/charge measurement tests on (B) Teflon AF and (C) PDMS. (D) Static shear strength values determined from force traces recorded during force/charge measurement tests on both Teflon AF and PDMS.

Before discussing the details of CE and the electrostatic interactions arising from that, it should be noted that along with electrostatic forces, van der Waals (vdW) and capillary forces could also contribute to the measured adhesion forces [2,3,13]; vdW interactions naturally exist between two materials in contact [74], while capillary interactions become effectual in humid conditions [13,74]. In regard to the latter, however, since all the

experiments were carried out at the constant relative humidity (RH) of 50±4 % (temperature, T = 24±1 °C), and since both substrates share an almost similar hydrophobicity (Teflon AF, θ = 108.4±0.6 °, n = 6; PDMS, θ = 106.0±0.7 °, n = 6), the contribution of capillary interactions in the overall interfacial interactions for both polymers should be essentially identical – while capillary interactions for PDMS could be even slightly more effective [13,127]. With respect to vdW forces, on the other hand, Teflon AF is also expected to generate somewhat smaller vdW forces in comparison to PDMS (see the Appendix C for more details). In particular, both polymers share a comparable sub-nanometric roughness (Teflon AF, R_a = 0.1±0.2 nm, n = 3; PDMS, R_a = 0.5±0.2 nm, n = 3), and therefore have similar geometry of contact with the gecko foot pad [3,105,150]. Hence, Teflon AF (with a Hamaker constant of 5.1×10^{-20} J) should develop almost 0.8 times smaller vdW forces than PDMS, which has a Hamaker constant of 6.5×10^{-20} J (see the Appendix C for more details). With Teflon AF having a weaker ability than PDMS to generate both vdW and capillary forces, development of observed enhanced adhesion forces by Teflon AF (Figure 7.1.D) points to the decisive contribution of CE-driven electrostatic interactions in gecko adhesion.

In order to determine the contribution of CE-driven electrostatic interactions in the generated adhesion forces, during the adhesion tests, the magnitude of the electric charges – developed right after contact occurred – was measured by image charge analysis [32,33,149]. When an electrically neutral gecko foot pad was brought into contact with the polymer thin film, the toes made contact with the substrate via the nano-scale spatulas (each 200–300 nm wide and 5–10 nm thick) [5,84] at the tip of the keratinous setae [20,21] of each toe on the foot pad

(Figure 7.5). As illustrated in Figures 7.5.B and 7.5.C, the exchange of electric charges between the fibrillar feature of the toe pads and the substrate gave rise to formation of an EDL at the contact interface. Separation of electric charges at the contact zone induced an image charge, with the density of σ_{image}, in the backing copper sheet. Knowing the magnitude of σ_{image} from the readings of the electrometer connected to the back of the copper sheet, the surface charge density over the polymer (σ_s), which can practically be considered equal to that on the foot pad [32,33], was determined (see Appendix C for more details).

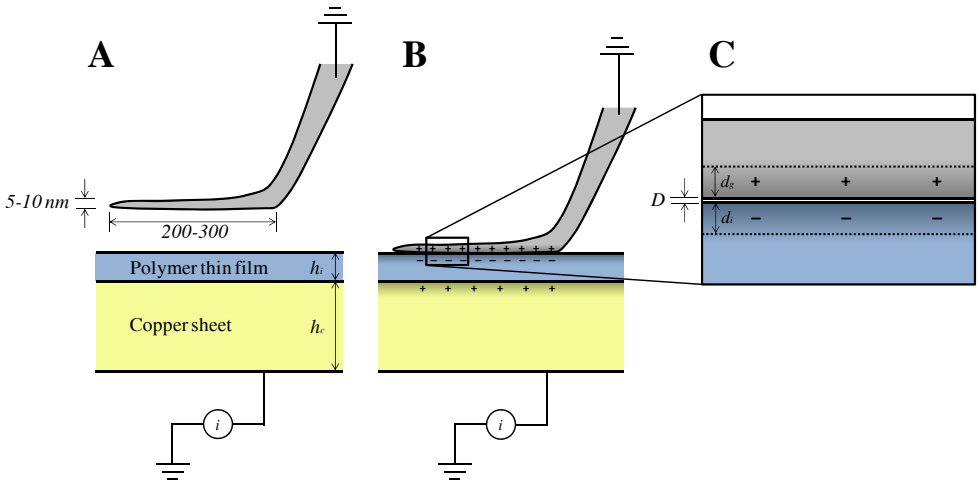

Figure 7.5. (A) Before contact of a nano-spatula – at the tip of a seta of a gecko toe pad – with the polymer thin film, both the spatula and the thin film were electrically neutral. (B) As the toe pad came into contact with the polymer thin film, electric charges separated between the nano-spatula and the thin film. The EDL, which was formed at the contact interface, induced certain electric charges in the backing copper sheet, which was grounded through an electrometer. (C) Electric charges that separated upon contact, penetrated up to a depth of d_i and d_g into the polymer thin film and the contacted nano-spatula, respectively. D is the actual separation distance (~0.3 nm) [2,84] between the nano-spatula and the thin film.

Charge measurement results revealed that during almost all contacts, the gecko foot pad became positively charged while the polymer was negatively charged. As illustrated in Figure 7.6.A, the absolute values of the surface charge densities immediately after intimate

contact with Teflon AF and PDMS were 1.6±0.2 mC/m^2 (n = 10) and 1.3±0.1 mC/m^2 (n = 10), respectively. In principle, these charge densities (equivalent to approximately 1 elementary charge per 89–134 nm^2) are relatively large [31,122], albeit typical for an intimate contact [32,33]. According to the charge measurement results and considering the toe pad-substrate interface as that between two parallel plates (see Appendix C for more details), the electrostatic forces that gecko foot pads develop with Teflon AF and PDMS – in the normal direction before sliding – are 4.7±1.2 N/cm^2 and 2.4±0.4 N/cm^2, respectively. Interestingly, the calculated surface forces are of the same magnitude and also, more or less, of the same proportion (almost, on average, twice larger) as the static lateral adhesion forces (Figure 7.4.D) that were experimentally measured for these substrates.

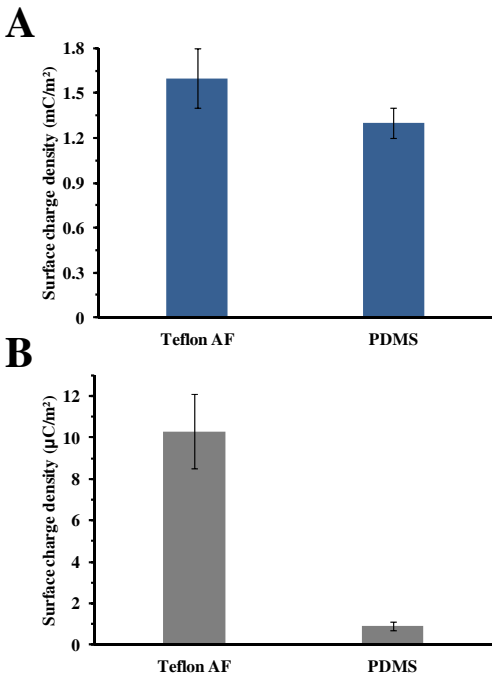

Figure 7.6. (A) Surface charge densities measured right after contact of gecko toe pads with Teflon AF and PDMS. (B) Surface charge densities after a single contact of gecko toe pads with the two polymer thin films.

Although advantageous for generating superior adhesion, electric charges that gecko toe pads develop upon contact are very large in magnitude [31-33,122], and can simply cause the gecko body to become overcharged during locomotion. Even so, we have found that upon detachment from the substrate, most of the electric charges which were exchanged between the toes and the substrate, flowed back to the original surface. In particular, to determine the effect of electrostatic discharge (ESD) on the adhesive properties of Teflon AF and PDMS in contact with gecko toe pads, the magnitude of the charge densities after contact were also measured. After contact-charge densities were measured after placing a single foot pad (five toes) of a gecko on a vertically-aligned thin film, followed by its removal from the substrate (after few seconds) by pulling the foot up perpendicularly from the surface. Measuring after-contact charge in this way allowed us to determine the number of electric charges per toe area, which remained on the substrates after removal of the toe pads. It should be noted that the sign of the electric charges acquired after contact was – mostly – positive for Teflon AF and negative for PDMS, despite both becoming negatively charged upon contact with gecko foot pads.

As illustrated in Figure 7.6.B, charge backflow via the electrostatic discharge phenomenon (which naturally happens during separation of the substrates charged via CE) [30-33,149], led to after-contact surface charge densities of 10.3±1.8 $\mu C/m^2$ (n = 10) over Teflon AF and 0.9±0.2 $\mu C/m^2$ (n = 10) over PDMS. The measured after-contact charge densities, which were two to three orders of magnitude smaller than those developed at the interface during

contact, are also moderately small when compared to typical after-contact charge densities (*i.e.*, 10–1000 μC/m^2) [31,122] of the polymers used. The efficient ESD from gecko toe pads, which is more significant when in contact with PDMS rather than Teflon AF (Figure 7.6.B), is actually not very surprising when the large dielectric constant of β-keratin (the main component of the fibrillar feature of gecko toe pads) [20,21] and the pointy nature of the setae are taken into consideration. More specifically, in contact of an insulator with a high dielectric material (as β-keratin is; see Appendix C for more details), most of the electric charges, which are separated during contact, flow back to the original surface as the surfaces detach from one another [31]. Above and beyond that, surface discharge is naturally very effective when at least one of the surfaces over which discharge occurs has a sharp tip [31], given that electric charges naturally accumulate densely around points and sharp edges [151]. Therefore, seemingly because of the special material and geometrical properties of the setae of the toe pads, upon fracture of the seta-substrate bond, most of the electric charges that were separated during detachment flowed back to the original surface, thus resulting in the very small after-contact charges observed for both substrates.

As illustrated, what makes the difference that geckos stick strongly to one substrate while they do not to the other is the extent of the contribution of CE-driven electrostatic interactions for each substrate. Even so, during the last 80 years of research on gecko adhesion, the contribution of electrostatic interactions in gecko adhesion has always been overlooked [2,3,5,152] – although never completely ruled out [21]. The role of electrostatic interactions in gecko adhesion was always passed over by referring to the experiments

conducted by Dellit [153], where adhesion of a gecko (12 g *Tarentola mauritanica*) was tested against a vertically-aligned chromed metal surface. After bombardment with ionized air, thereby, supposedly, eliminating electrostatic interactions, and observing that the adhesion between the gecko and the metal surface did not change, Dellit concluded that the electrostatic interactions did not contribute to the adhesion of geckos [153]. The control sample used by Dellit was small pieces of a paper that were brought to adhere to a glass rod, which was charged by rubbing in advance [153]. In regard to Dellit's experiments, it should be noted that air ionization is not a proper method for discharging the CE-driven electrostatic interactions of gecko foot pads upon intimate contact. Put otherwise, during ionization of air by radioactive ionization or X-ray radiation, as employed by Dellit [153], elementary air ions (typically ~0.4 nm in size), within a fraction of a second after their creation, attract 8–15 (mostly water) molecules to themselves and form positive and negative molecular clusters, known as "air ions" [151]. As a matter of fact, due to their relatively massive size, air ions can only be employed to eliminate electric charges from an electrostatic contact – like that of the paper-glass with typical micro-scale roughness – where air ions can reach the contact interface to dissipate surface charges. In the intimate contact of seta-substrate, with an atomic separation distance of ~0.3 nm [2,84], however, eliminating CE-generated electrostatic forces by air ionization is not even practical, simply because air ions cannot penetrate between the contact interface in order to dissipate surface charges.

Chapter 8. Concluding Remarks, Main Thesis Contributions, and Recommendations

8.1 Summary and concluding remarks

In this thesis, the fundamental understanding about dry adhesion of both geckos and gecko-inspired adhesives was highlighted first. Following these basic principles, fabrication of synthetic bio-inspired dry adhesives was subsequently discussed. Then, details on the possible sources of the adhesion of both natural and synthetic dry adhesives were illustrated.

We subsequently discussed the following points:

- The fabrication of a state-of-the-art dry adhesive, by replica-molding, from a non-sticky fluoropolymer, Teflon AF. Using anodic aluminum oxide as the mold, for the first time, extremely high aspect-ratio nanopillars with a unique nanostructure at the top were fabricated.
- We then managed to modify the structural properties of both the base and the terminating nanostructure of this novel dry adhesive (by a combination of conventional and a novel fabrication technique that we developed).
- By conducting tribological tests, we have found that the unique structural and material properties of the fabricated nanopillars allowed them to generate enhanced adhesion forces in both normal and shear directions via contact electrification-driven electrostatic interactions.

- More interestingly, certain types of the fabricated dry adhesive have succeeded to generate enhanced adhesion forces under water (the exact mechanism of adhesion underwater is not fully understood).

Following the fabrication, modification and characterization of the structural as well as the adhesion properties of bi-level Teflon AF nanopillars, we set out to look into the contribution of contact electrification dry adhesives in the adhesive performance of other synthetic dry adhesives.

- By looking into the performance of other polymeric dry adhesives and by pooling together the surface charge densities that polymers other than Teflon AF generate upon contact, we have explained the possibility of the occurrence and also the effectiveness of contact electrification in the adhesive performance of polymeric dry adhesives.
- We have shown that not only is contact electrification highly expected to happen in contact of polymeric dry adhesives, but also it should have a great contribution in their adhesive properties.

After looking into the role of contact electrification in adhesive performance of synthetic dry adhesives, we looked into the role of contact electrification and the electrostatic interactions arising from it in dry adhesion of their prototype, geckos.

- By directly measuring the magnitude of surface charges along with adhesion forces that geckos develop on various surfaces, we have shown that gecko adhesion is greatly dominated by unappreciated before contact electrification-driven electrostatic interactions. This was shown for the first time.
- Our first experimental evidence for the decisive role of electrostatic interactions in gecko adhesion is not only very important for understanding the fundamentals of the supreme dry adhesion of geckos, but also it is very crucial in design and fabrication of synthetic dry adhesives, which we speculated to largely rely on contact electrification-driven electrostatic interactions for their performance.

8.2 Main thesis contributions

Over 2,000 years ago, Aristotle commented on the surprising ability of geckos to "run up and down a tree in any way, even with the head downwards". During the last century or so, scientists have conducted research to find the origin of the supreme adhesion of geckos. In this vein, which also led to the creation of synthetic gecko-inspired fibrillar dry adhesives almost a decade ago, and after ruling out all postulated sources of adhesion (*e.g.*, suction, micro-interlocking, glue, and also electrostatic interactions), the supreme adhesion of geckos was eventually attributed, in the early 2000s, to the dominance of van der Waals interactions, which naturally exist in contact of any two surfaces. In humid conditions, however, the assisting role of capillary forces has also been discussed. In summary, over a thousand papers, reviews, and book chapters have been published on the dry adhesion of geckos and

also on synthetic gecko-inspired dry adhesives, all relying on the dominance of van der Waals interactions (and the assisting contribution of capillary interactions), in order to explain adhesion.

In this research, we have succeeded in fabricating a state-of-the-art bi-level nanostructure (as a fibrillar dry adhesive) from a hydrophobic polymer, Teflon AF, having the weakest van der Waals interactions of all solid organic polymers (Chapter 3). Although Teflon AF is not an effective van der Waals interaction generator, surprisingly large adhesion forces were detected for the fabricated dry adhesive, which could not be explained based on the principles of van der Waals interactions. The contradictory behavior of Teflon AF nanopillars led us to look into the occurrence and effectiveness of contact electrification-driven electrostatic interactions, which a fluoropolymer like Teflon AF can effectively generate (see Chapter 4 and 5).

After re-examining the role of contact electrification in the adhesive performance of bi-level Teflon AF nanopillars, and by considering the surface charge densities that polymers other than Teflon AF can generate upon contact, we have illustrated in Chapter 6 the possibility of occurrence of contact electrification and role of electrostatic interactions arising from it in the adhesive performance of other polymeric dry adhesives.

Motivated by our detailed review of the literature and considering that all the principles regarding the likelihood of contact electrification in synthetic dry adhesives are also

applicable to the dry adhesion of their prototype, geckos, we set out to address an even more important question: "Does gecko adhesion stem from electrostatic interactions?". From this perspective, in Chapter 7, we have illustrated – for the first time – the dominance of contact electrification-driven electrostatic interactions in gecko adhesion. Otherwise stated, our results completely clarified that it is the contact electrification-driven electrostatic interactions which dictate the strength of gecko adhesion, and not the van der Waals or capillary forces.

8.3 Recommendations for future steps

8.3.1 Short-term recommendations

There are several short-term studies which can be carried out to address some of the unanswered questions which occurrence of contact electrification can raise in regard to the dry adhesion of both natural and synthetic dry adhesives.

- First and foremost, although we have shown electrostatic forces are dominant, one can still investigate what percentage of gecko adhesion is coming from electrostatic interactions. In fact, this can be achieved by some experiments in completely dry conditions (which essentially eliminate the role of capillary forces). Following that, some theoretical analysis or even simulations can be conducted to distinguish the input of van der Waals forces from that of electrostatic interactions in dry adhesion of geckos and, from that perspective, that of gecko-inspired dry adhesives.

- Next, it needs to be clarified how water uptake alters the adhesive properties of gecko toe pads. For several decades, adhesion of geckos has been studied according to material properties of β-keratin, the main component comprising the fibrillar feature of gecko toe pads. Even so, it has been widely overlooked that keratinous materials can uptake significant amounts of water in humid conditions, and their material properties (specifically, dielectric constant and conductivity) will thus significantly change (by even an order of magnitude). From this perspective, it is very crucial that the role of water uptake be clarified in adhesive properties of geckos, from the aspect of contact electrification-driven electrostatic interactions.

In regard to synthetic dry adhesives, specifically bi-level Teflon AF nanopillars, some additional questions also need to be answered.

- First, what is the mechanism of the formation of the finger-like nanostructure developing ahead of the polymer melt in the alumina nanochannels? Even though we have managed to control its geometrical properties by adjusting the processing temperatures, the exact mechanism of its formation, which is exclusive to infiltration of Teflon AF melt in alumina nanochannels, is still elusive. Clarifying this mechanism is not only important for understanding better the behavior of Teflon AF melt in alumina nanochannels, but also it can pave the way for incorporation of the fingering phenomenon in nanochannels toward fabrication of either more advanced nanostructures, even from other materials.

- Next, the exact mechanism of the underwater adhesion of bi-level Teflon AF nanopillars is still missing. As this characteristic of bi-level Teflon AF nanopillars is very interesting and can help the emergence of this nanostructure in so many other advanced applications, as discussed in the thesis, it is very important that this interesting behavior of Teflon AF nanopillars be also completely studied.

8.3.2 Long-term recommendations

Since the idea and evidence about the occurrence of contact electrification and dominance of electrostatic interactions in dry adhesion of geckos and gecko-inspired dry adhesives are absolutely new, they raise several interesting questions for long-term future work.

- First, the role of many variables which naturally influence contact electrification (*e.g.*, the nature of the contacting materials, possible partial discharge across the separating gap, surface topography, humidity, duration of contact, surface contamination, and temperature) needs to be investigated in dry adhesion of both natural and synthetic dry adhesives.
- Another important factor is the magnitude of local charge densities. In particular, electric charges which separate via contact electrification, do not distribute in a homogenous manner over insulators which are conventionally used to fabricate dry adhesives. In contrast, they localize themselves in micro/nanodomains which are more or less of the same scale as the size of both natural and synthetic fibrillar dry adhesives. So, seeing that the charge densities on these micro/nanodomains are

naturally (up to 3 orders of magnitude) larger than the net surface charge densities that surface charge characterization techniques do measure, it is needed that their role in adhesive properties of dry adhesives be clarified.

- Indeed, another very critical factor, which can largely affect the magnitude of electrostatic interactions arising from contact electrification, is the depth of the penetration of electric charges in the contacted substrates. In the literature, various numbers, ranging from the atomic scale of less than a nanometer up to few micrometers, are reported for charge penetration depth in case of insulators. Seeing that even a slight change in charge penetration depth can significantly alter the magnitude of the contact electrification-driven electrostatic interactions over insulators, it is very crucial that a systematic study regarding this matter be carried out.
- Last but not least, in the case of dry adhesion of both natural and synthetic dry adhesives, the mechanism of charge transfer, which can be either electron, ion, and/or material transfer, needs to be investigated. In fact, there is an ongoing controversy regarding the mechanism of charge transfer over insulators. However, given that the charge transfer mechanism is essentially dictating all contact electrification properties, it is essential to figure out the exact mechanism of charge transfer in the case of dry adhesives, either natural or synthetic ones.

References

[1] Izadi H, Penlidis A. Macromolecular Reaction Engineering 2013;7(11):570-572.

[2] Autumn K, Liang YA, Hsieh ST, Zesch W, Chan WP, Kenny TW, et al. Nature 2000;405(6787):681-685.

[3] Autumn K, Sitti M, Liang YA, Peattie AM, Hansen WR, Sponberg S, et al. Proceedings of the National Academy of Sciences 2002;99(19):12252-12256.

[4] Autumn K, Gravish N. Philosophical Transactions of the Royal Society A: Mathematical, Physical and Engineering Sciences 2008;366(1870):1575-1590.

[5] Autumn K. Properties, principles, and parameters of the gecko adhesive system. Biological adhesives: Springer; 2006. p. 225-256.

[6] Autumn K, Majidi C, Groff R, Dittmore A, Fearing R. The Journal of Experimental Biology 2006;209(18):3558-3568.

[7] Autumn K, Dittmore A, Santos D, Spenko M, Cutkosky M. The Journal of Experimental Biology 2006;209(18):3569-3579.

[8] Arzt E, Gorb S, Spolenak R. Proceedings of the National Academy of Sciences 2003;100(19):10603-10606.

[9] Gorb SN. Philosophical Transactions of the Royal Society A: Mathematical, Physical and Engineering Sciences 2008;366(1870):1557-1574.

[10] Gorb SN, Sinha M, Peressadko A, Daltorio KA, Quinn RD. Bioinspiration & biomimetics 2007;2(4):S117.

[11] Kesel A, Martin A, Seidl T. The Journal of Experimental Biology 2003;206(16):2733-2738.

[12] Kesel AB, Martin A, Seidl T. Smart Materials and Structures 2004;13(3):512-518.

[13] Huber G, Mantz H, Spolenak R, Mecke K, Jacobs K, Gorb SN, et al. Proceedings of the National Academy of Sciences 2005;102(45):16293-16296.

[14] Huber G, Gorb SN, Spolenak R, Arzt E. Biology Letters 2005;1(1):2-4.

[15] Hu S, Xia Z, Dai L. Nanoscale 2013;5(2):475-486.

[16] Hu S, Xia Z. Small 2012;8(16):2464-2468.

[17] Boesel LF, Greiner C, Arzt E, del Campo A. Advanced Materials 2010;22(19):2125-2137.

[18] Jeong HE, Suh KY. Nano Today 2009;4(4):335-346.

[19] Geim A, Grigorieva SDI, Novoselov K, Zhukov A, Shapoval SY. Nature Materials 2003;2(7):461-463.

[20] Alibardi L. Zoology 2009;112(6):403-424.

[21] Maderson P. Nature 1964; 203(4946):780-781.

[22] Kwak MK, Pang C, Jeong H, Kim H, Yoon H, Jung H, et al. Advanced Functional Materials 2011;21(19):3606-3616.

[23] Ho AYY, Yeo LP, Lam YC, Rodríguez I. ACS Nano 2011;5(3):1897-1906.

[24] Jeong HE, Lee J, Kim HN, Moon SH, Suh KY. Proceedings of the National Academy of Sciences 2009;106(14):5639-5644.

[25] Scheirs J. Modern fluoropolymers: high performance polymers for diverse applications: Wiley; 1997.

[26] Craster R, Matar O. Reviews of Modern Physics 2009;81(3):1131-1198.

[27] Bonn D, Eggers J, Indekeu J, Meunier J, Rolley E. Reviews of Modern Physics 2009;81(2):739-805.

[28] Cazabat A, Heslot F, Troian S, Carles P. Nature 1990;346(6287):824-826.

[29] Izadi H, Golmakani M, Penlidis A. Soft Matter 2013;9(6):1985-1996.

[30] Harper WR. Contact and frictional electrification: Laplacian Press; 1967.

[31] Lowell J, Rose-Innes A. Advances in Physics 1980;29(6):947-1023.

[32] Horn RG, Smith DT. Science 1992;256(5055):362-364.

[33] Horn RG, Smith DT, Grabbe A. Nature 1993;366(6454):442-443.

[34] Apodaca MM, Wesson PJ, Bishop KJ, Ratner MA, Grzybowski BA. Angewandte Chemie International Edition 2010;122(5):958-961.

[35] Baytekin H, Patashinski A, Branicki M, Baytekin B, Soh S, Grzybowski BA. Science 2011;333(6040):308-312.

[36] Baytekin HT, Baytekin B, Soh S, Grzybowski BA. Angewandte Chemie International Edition 2011;50(30):6766-6770.

[37] McCarty LS, Whitesides GM. Angewandte Chemie International Edition 2008;47(12):2188-2207.

[38] Izadi H, Sarikhani K, Penlidis A. Nanotechnology 2013;24(50):505306.

[39] Lee H, Lee BP, Messersmith PB. Nature 2007;448(7151):338-341.

[40] Varenberg M, Gorb S. Journal of the Royal Society interface 2008;5(20):383-385.

[41] Yu Z, Watson PK, Facci JS. Journal of Physics D: Applied Physics 1990;23(9):1207-1211.

[42] Liu C, Bard AJ. Nature Materials 2008;7(6):505-509.

[43] Liu C, Bard AJ. Chemical Physics Letters 2009;480(4):145-156.

[44] Baytekin HT, Baytekin B, Incorvati JT, Grzybowski BA. Angewandte Chemie International Edition 2012;124(20):4927-4931.

[45] Baytekin B, Baytekin HT, Grzybowski BA. Journal of the American Chemical Society 2012;134(17):7223-7226.

[46] Soh S, Kwok SW, Liu H, Whitesides GM. Journal of the American Chemical Society 2012;134(49):20151-20159.

[47] Sow M, Widenor R, Kumar A, Lee SW, Lacks DJ, Sankaran RM. Angewandte Chemie International Edition 2012;124(11):2749-2751.

[48] Sow M, Lacks DJ, Sankaran RM. Journal of Electrostatics 2013;71(3):396-399.

[49] Davies D. Journal of Physics D: Applied Physics 1969;2(11):1533-1537.

[50] Liu C, Bard AJ. Journal of the American Chemical Society 2009;131(18):6397-6401.

[51] Terris B, Stern J, Rugar D, Mamin H. Physical Review Letters 1989;63(24):2669-2672.

[52] Glassmaker NJ, Jagota A, Hui C, Noderer WL, Chaudhury MK. Proceedings of the National Academy of Sciences 2007;104(26):10786-10791.

[53] Greiner C, del Campo A, Arzt E. Langmuir 2007;23(7):3495-3502.

[54] Greiner C, Arzt E, del Campo A. Advanced Materials 2009;21(4):479-482.

[55] Greiner C, Buhl S, del Campo A, Arzt E. The Journal of Adhesion 2009;85(9):646-661.

[56] Shen L, Glassmaker NJ, Jagota A, Hui C. Soft Matter 2008;4(3):618-625.

[57] del Campo A, Greiner C, Arzt E. Langmuir 2007;23(20):10235-10243.

[58] Sitti M, Fearing RS. Journal of Adhesion Science and Technology 2003;17(8):1055-1073.

[59] Parness A, Soto D, Esparza N, Gravish N, Wilkinson M, Autumn K, et al. Journal of the Royal Society Interface 2009;6(41):1223-1232.

[60] Jeong HE, Kwak MK, Suh KY. Langmuir 2010;26(4):2223-2226.

[61] Bae W, Kwak MK, Jeong HE, Pang C, Jeong H, Suh K. Soft Matter 2013;9(5):1422-1427.

[62] Murphy MP, Aksak B, Sitti M. Small 2009;5(2):170-175.

[63] Murphy MP, Kim S, Sitti M. ACS Applied Materials & Interfaces 2009;1(4):849-855.

[64] Lee DY, Lee DH, Lee SG, Cho K. Soft Matter 2012;8(18):4905-4910.

[65] Jeong HE, Lee SH, Kim P, Suh KY. Nano letters 2006;6(7):1508-1513.

[66] Kustandi TS, Samper VD, Yi DK, Ng WS, Neuzil P, Sun W. Advanced Functional Materials 2007;17(13):2211-2218.

[67] Majidi C, Groff R, Maeno Y, Schubert B, Baek S, Bush B, et al. Physical Review Letters 2006;97(7):076103.

[68] Lee J, Majidi C, Schubert B, Fearing RS. Journal of the Royal Society Interface 2008;5(25):835-844.

[69] Schubert B, Lee J, Majidi C, Fearing RS. Journal of the Royal Society Interface 2008;5(25):845-853.

[70] Gillies AG, Fearing RS. Langmuir 2011;27(18):11278-11281.

[71] Lee H, Bhushan B. Journal of Colloid and Interface Science 2012;372(1):231-238.

[72] Kinloch AJ. Adhesion and adhesives: science and technology: Springer; 1987.

[73] Kendall K. Molecular adhesion and its applications: the sticky universe: Springer; 2001.

[74] Israelachvili JN. Intermolecular and surface forces: revised third edition: Academic press; 2011.

[75] Vakula VL, Pritykin LM. Polymer adhesion: physico-chemical principles: Ellis Horwood; 1991.

[76] Lee L. Fundamentals of adhesion: Plenum Publishing Corporation; 1991.

[77] Pocius AV. Adhesion and adhesives technology: an introduction: Hanser Verlag; 2002.

[78] Izadi H, Penlidis A. Macromolecular Reaction Engineering 2013;7(10):482-483.

[79] Sameoto D, Menon C. Smart Materials and Structures 2010;19(10):103001.

[80] Persson B. The Journal of Chemical Physics 2003;118(16):7614-7621.

[81] Spuskanyuk A, McMeeking R, Deshpande V, Arzt E. Acta Biomaterialia 2008;4(6):1669-1676.

[82] Autumn K. MRS Bulletin 2007;32(6):473-478.

[83] Autumn K, Peattie AM. Integrative and Comparative Biology 2002;42(6):1081-1090.

[84] Tian Y, Pesika N, Zeng H, Rosenberg K, Zhao B, McGuiggan P, et al. Proceedings of the National Academy of Sciences 2006;103(51):19320-19325.

[85] Hu S, Jiang H, Xia Z, Gao X. ACS Applied Materials & Interfaces 2010;2(9):2570-2578.

[86] Del Campo A, Arzt E. Macromolecular Bioscience 2007;7(2):118-127.

[87] Glassmaker N, Jagota A, Hui C, Kim J. Journal of the Royal Society Interface 2004;1(1):23-33.

[88] Spolenak R, Gorb S, Gao H, Arzt E. Proceedings of the Royal Society A: Mathematical, Physical and Engineering Science 2005;461(2054):305-319.

[89] Qu L, Dai L. Advanced Materials 2007;19(22):3844-3849.

[90] Qu L, Dai L, Stone M, Xia Z, Wang ZL. Science 2008;322(5899):238-242.

[91] Ge L, Sethi S, Ci L, Ajayan PM, Dhinojwala A. Proceedings of the National Academy of Sciences 2007;104(26):10792-10795.

[92] Röhrig M, Thiel M, Worgull M, Hölscher H. Small 2012;8(19):3009-3015.

[93] Varenberg M, Pugno NM, Gorb SN. Soft Matter 2010;6(14):3269-3272.

[94] Greiner C, Spolenak R, Arzt E. Acta Biomaterialia 2009;5(2):597-606.

[95] Yao H, Gao H. Journal of Mechanics and Physics of Solids 2006;54(6):1120-1146.

[96] Barnes WJP. Journal of Comparative Physiology A: Neuroethology, Sensory, Neural, and Behavioral Physiology 2006;192(11):1165-1168.

[97] Izadi H, Zhao B, Han Y, McManus N, Penlidis A. Journal of Polymer Science Part B: Polymer Physics 2012;50(12):846-851.

[98] Hamaker H. Physica 1937;4(10):1058-1072.

[99] Lifshitz E. Soviet Physics, JETP 1956;2(1):73-83.

[100] Lee S, Sigmund WM. Colloids and Surfaces A: Physicochemical and Engineering Aspects 2002;204(1):43-50.

[101] Hertz H. Miscellaneous papers: Macmillan; 1896.

[102] Derjaguin B, Muller V, Toporov YP. Journal of Colloid and Interface Science 1975;53(2):314-326.

[103] Maugis D. Journal of Colloid and Interface Science 1992;150(1):243-269.

[104] Johnson K, Kendall K, Roberts A. Proceedings of the Royal Society of London.A.Mathematical and Physical Sciences 1971;324(1558):301-313.

[105] Persson B, Gorb S. The Journal of Chemical Physics 2003;119(21):11437-11444.

[106] Lacks DJ, Sankaran RM. Journal of Physics D: Applied Physics 2011;44(45):453001.

[107] McGuiggan PM. Langmuir 2008;24(8):3970-3976.

[108] Diaz A, Wollmann D, Dreblow D. Chemistry of Materials 1991;3(6):997-999.

[109] Williams MW. Journal of Electrostatics 2013;71(1):53-54.

[110] Lee L. Journal of Electrostatics 1994;32(1):1-29.

[111] Brennan W, Lowell J, O'Neill M, Wilson M. Journal of Physics D: Applied Physics 1992;25(10):1513-1517.

[112] Homewood K. Journal of Physics D: Applied Physics 1984;17(6):1255-1263.

[113] Smith DT. Journal of Electrostatics 1991;26(3):291-308.

[114] Rimai D, Ezenyilimba M, Goebel W, Cormier S, Quesnel D. Journal of Imaging Science and Technology 2002;46(3):200-207.

[115] Rimai D, Quesnel D. The Journal of Adhesion 2002;78(5):413-429.

[116] Rimai D, Quesnel D, Reifenberger R. The Journal of Adhesion 2000;74(1-4):283-299.

[117] Tang T, Hui C, Jagota A. Journal of Physics D: Applied Physics 2006;99(5):054906.

[118] Bailey AG. Journal of Electrostatics 2001;51-52:82-90.

[119] Lowell J. Journal of Physics D: Applied Physics 1981;14(8):1513-1522.

[120] Lowell J. Journal of Physics D: Applied Physics 1977;10(17):L233-L235.

[121] Lowell J. Journal of Physics D: Applied Physics 1990;23(8):1082-1091.

[122] Izadi H, Penlidis A. Macromolecular Reaction Engineering 2013;7(11):588-608.

[123] Thomas SW, Vella SJ, Kaufman GK, Whitesides GM. Angewandte Chemie International Edition 2008;120(35):6756-6758.

[124] Rezende C, Gouveia R, da Silva M, Galembeck F. Journal of Physics: Condensed Matter 2009;21(26):263002.

[125] Bhushan B. Langmuir 2012;28(3):1698-1714.

[126] Stark AY, Sullivan TW, Niewiarowski PH. The Journal of Experimental Biology 2012;215(17):3080-3086.

[127] Stark AY, Badge I, Wucinich NA, Sullivan TW, Niewiarowski PH, Dhinojwala A. Proceedings of the National Academy of Sciences 2013;110(16):6340-6345.

[128] Kim T, Jeong HE, Suh KY, Lee HH. Advanced Materials 2009;21(22):2276-2281.

[129] Lu G, Hong W, Tong L, Bai H, Wei Y, Shi G. ACS Nano 2008;2(11):2342-2348.

[130] Meng G, Jung YJ, Cao A, Vajtai R, Ajayan PM. Proceedings of the National Academy of Sciences 2005;102(20):7074-7078.

[131] Olsen DA, Osteraas AJ. The Journal of Physical Chemistry 1964;68(9):2730-2732.

[132] Kim E, Xia Y, Whitesides GM. Nature 1995;376(6541):581-584.

[133] Martín J, Maiz J, Sacristan J, Mijangos C. Polymer 2012;53(6):1149-1166.

[134] Martín J, Mijangos C. Langmuir 2008;25(2):1181-1187.

[135] Zhang M, Dobriyal P, Chen J, Russell TP, Olmo J, Merry A. Nano Letters 2006;6(5):1075-1079.

[136] Blonski S, Garofalini S. Surface Science 1993;295(1-2):263-274.

[137] Barbero DR, Saifullah MS, Hoffmann P, Mathieu HJ, Anderson D, Jones GA, et al. Advanced Functional Materials 2007;17(14):2419-2425.

[138] Suh D, Choi S, Lee HH. Advanced Materials 2005;17(12):1554-1560.

[139] Baeg K, Noh Y, Kim D. Solid-State Electronics 2009;53(11):1165-1168.

[140] Persson B, Popov V. Solid State Communications 2000;114(5):261-266.

[141] Srivastava D, Lee I. Advanced Materials 2006;18(18):2471-2475.

[142] Charvat F, Kingery W. Journal of the American Ceramic Society 1957;40(9):306-315.

[143] Sweet J, Roth E, Moss M. International Journal of Thermophysics 1987;8(5):593-606.

[144] Gao H, Yao H. Proceedings of the National Academy of Sciences 2004;101(21):7851-7856.

[145] Sitti M, Cusick B, Aksak B, Nese A, Lee H, Dong H, et al. ACS Applied Materials & Interfaces 2009;1(10):2277-2287.

[146] Northen MT, Greiner C, Arzt E, Turner KL. Advanced Materials 2008;20(20):3905-3909.

[147] Kim S, Sitti M, Xie T, Xiao X. Soft Matter 2009;5(19):3689-3693.

[148] Ko H, Lee J, Schubert BE, Chueh Y, Leu PW, Fearing RS, et al. Nano Letters 2009;9(5):2054-2058.

[149] Ireland PM. Journal of Electrostatics 2009;67(2):462-467.

[150] Huber G, Gorb SN, Hosoda N, Spolenak R, Arzt E. Acta Biomaterialia 2007;3(4):607-610.

[151] Jonassen N. Electrostatics: Springer; 2002.

[152] Hiller U. Zeitschrift Für Morphologie der Tiere 1968;62(4):307-362.

[153] Dellit W. Zur anatomie und physiologie der Geckozehe. Jenaische Zeitschrift fr Naturwissenschaft 1934;68:613-656.

[154] Park H, Park C, Tzoganakis C, Tan K, Chen P. Industrial and Engineering Chemistry Research 2006;45(5):1650-1658.

[155] From the product specifications reported by the producer.

[156] Happey F. Applied fibre science: Academic Press; 1978.

[157] Maeda H. Biophysical Journal 1989;56(5):861-868.

[158] Marzec E. Bioelectrochemistry and Bioenergetics 1998;46(1):29-32.

[159] Marzec E, Kubisz L. International Journal of Biological Macromolecules 1997;20(2):161-165.

[160] Marzec E. Radiation Physics and Chemistry 2000;59(5):477-481.

[161] Rizvi TZ, Khan MA. International Journal of Biological Macromolecules 2008;42(3):292-297.

[162] Land M. Progress in Biophysics and Molecular Biology 1972;24:75-106.

Appendix A. Supporting Information for Chapter 4

High aspect-ratio (AR) nanopillars terminated with a fluffy nanostructure on top were fabricated on Teflon AF by infiltration of the polymer melt into an anodic aluminum oxide (AAO) membrane as the mold. The effective elastic modulus (E_{eff}) of the fabricated nanopillars can be calculated by Equation 2.1. Considering E = 1.5 GPa [25], μ = 0.35, θ = 89°, and 25% porosity in the mold, which results in $d = 8\times10^{12}$ pillars/m^2, the theoretical effective elastic modulus of nanopillars, excluding the hierarchical level, was calculated. For an identical structure, increasing the pillar height (and, consequently, enhancing the AR of pillars) results in lower effective elastic modulus for the fibrillar structure. Lower elastic modulus allows the probe to penetrate deeper into the dry adhesive and thus the number of pillars which come into contact at a specific loading force increases.

Figure A.1.A shows the schematic of an indentation test and typical force traces (*i.e.*, normal force vs. displacement) for all samples under the nominal preload of 50 mN. The measured ultimate penetration depths (L_{pd}) of the fused silica probe in nanopillars as well as the flat control sample at different preloads are plotted in Figure A.1.B. By using the probe penetration depth values (L_{pd}) and considering the geometrical correlations of the probe in contact, the approximate apparent surface area at the contact zone (a_{con}) was calculated by $a_{con} = \pi L_{pd} (d' - L_{pd})$ where d' is the probe diameter (see Figure A.1.C) [63].

It can be seen in Figure A.1.C that the change of the surface area with preload within the applied preload range of ~5–50 mN is almost linear for all samples, including the bi-level

nanopillars and the flat control sample. Using the calculated apparent contact areas, the adhesion strength (pull-off force per unit surface area) for hierarchical nanopillars at different preloads has been calculated (Figure A.1.D). The plot in Figure A.1.D was used to calculate the maximum adhesion strength and the corresponding pull-off force for nanopillars of different geometrical properties.

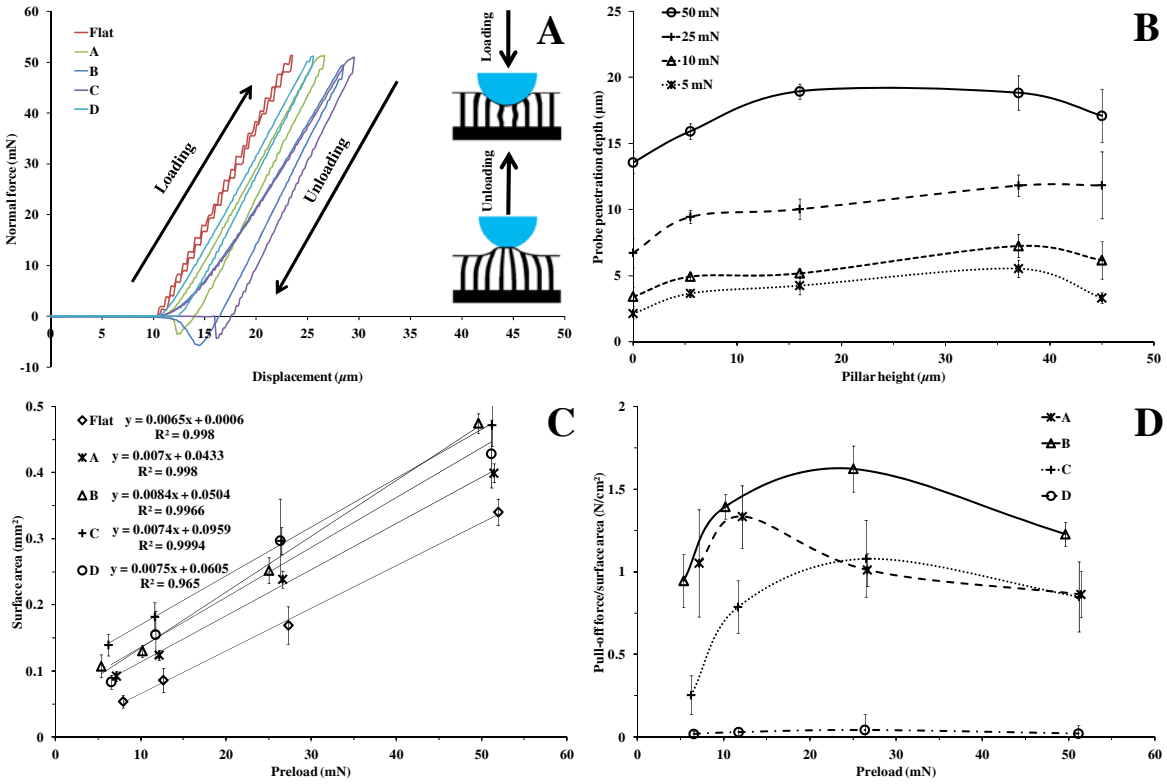

Figure A.1. (A) Typical force traces (normal force vs. displacement) for different nanopillars of ~5.5, 16, 37, and 45 μm tall (samples A, B, C, and D, respectively) as well as for the flat control samples under a nominal preload of 50 mN. The schematic shows the two steps of loading and unloading in an indentation test with a hemispherical fused silica probe (8 mm in diameter) on bi-level Teflon AF nanopillars. (B) Corresponding probe penetration depth, (C) Apparent surface area, and (D) Adhesion strength (*i.e.*, pull-off force per unit surface area) for double-level nanopillars of 200 nm in diameter at nominal preloads of 5, 10, 25, and 50 mN.

According to Lifshitz theory [99], the Hamaker constant between phase 1 (fused silica probe) and phase 2 (Teflon AF) interacting across the medium 3 (air) can be calculated by Equation

2.5. Considering that $\varepsilon_1 = 3.8$, $n_1 \approx 1.448$, $\varepsilon_2 = 1.93$, $n_2 \approx 1.31$, $\varepsilon_3 = 1$, and $n_3 = 1$, the Hamaker constant for the fused silica probe in contact with a flat Teflon AF surface would be approximately equal to 5.64×10^{-20} J at 298 K.

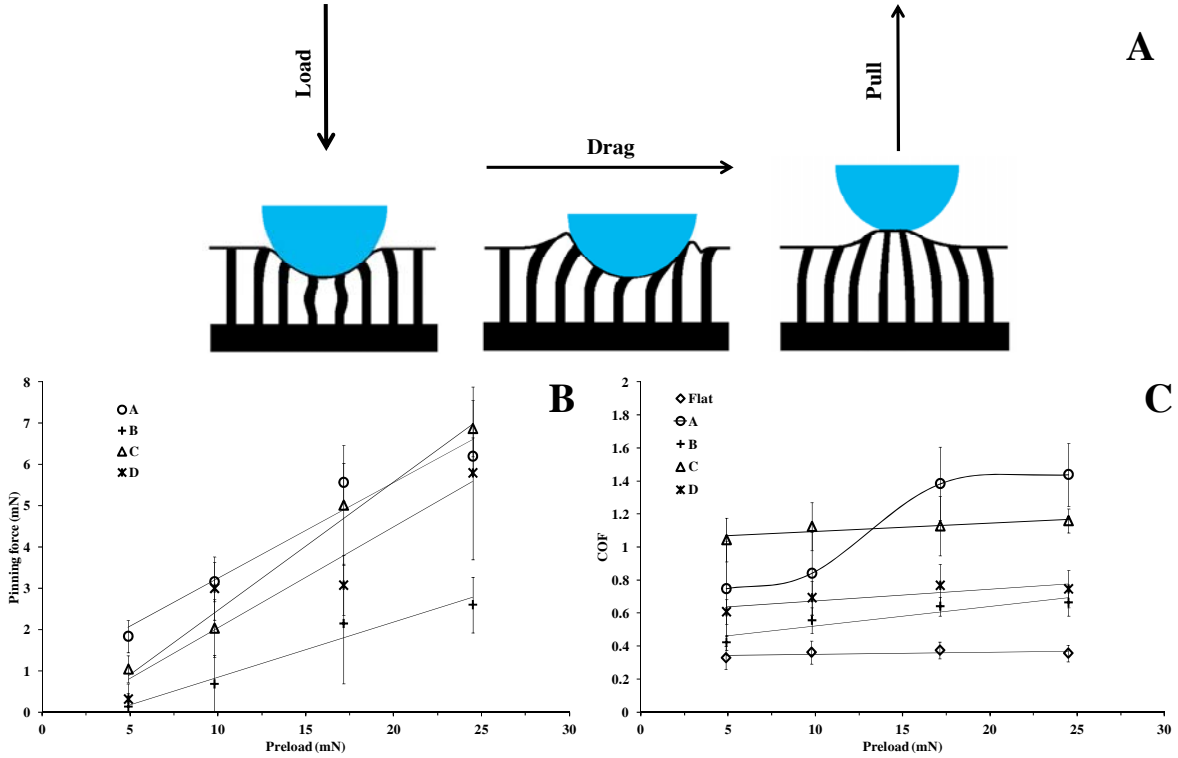

Figure A.2. (A) Schematic of the three steps of load, drag, and pull in a typical LDP test with a hemispherical fused silica probe (8 mm in diameter) on bi-level Teflon AF nanopillars. (B) Pinning force (*i.e.*, the amount of decrease in the absolute value of the normal force at the start of the dragging step in LDP tests) and (C) Static coefficient of friction (COF) for the flat control sample and nanopillars of 200 nm in diameter with different heights of approximately 5.5, 16, 37, and 45 μm (samples A, B, C, and D, respectively) at nominal preloads of 5, 10, 17.5, and 25 mN.

The schematic of an LDP test on bi-level nanopillars is shown in Figure A.2.A. In the LDP tests, at the start of dragging the probe over the nanopillars, a rapid substantial decrease in the absolute value of the loading force (*i.e.*, the normal force) was detected. The absolute value of this decrease (called "pinning force") at different preloads, for all hierarchical nanopillars,

has been plotted in Figure A.2.B. The pinning force for the flat sample was not detected; for nanopillars, it was significant and increased linearly with preload. The static coefficient of friction (COF) values for all hierarchical nanopillars as well as for the flat control sample at different preloads are plotted in Figure A.2.C. The measured static COF at the onset of dragging quantifies the force required to initiate the motion divided by the actual force pressing the probe over the nanopillars. The static COF for the flat surface was constant, as expected, but that of the nanopillars increased with increasing the preload (see Figure A.2.C); overall, the COF values were remarkably higher than those of the flat surface.

Appendix B. Supporting Information for Chapter 5

Fabrication of bi-level Teflon AF nanopillars was carried out by replica-molding using an anodic aluminum oxide (AAO) membrane as the mold. The AAO membrane (with the hierarchical level facing up) [130] was placed on top of a hotplate (EchoTherm Digital Hot Plate; ±1 °C temperature stability; Pines Scientific, Inc.) which was covered with aluminum foil. Next, a stainless steel (SS) cylinder (inner diameter of ~19 mm) was positioned over the mold and the polymer granules (~0.2 g) were placed inside the cylinder over the mold. A SS piston (type 304) with a cooling setup over it was fitted inside the cylinder and on top of the polymer granules (see Figure B.1). The cooling temperature (T_C) was adjusted to the desired temperature of –20, 0, 20, or 40 °C, by circulating cooling liquid (silicon oil; Thermofluid M40.165.10; temperature range: –40 to 165 °C) through a glass chamber above the SS cylinder (Figure B.1). The temperature of the cooling liquid was adjusted using a Petite Fleur circulator (temperature range: –40 to 200 °C, temperature stability: ±0.01 °C) from Peter Huber Kältemaschinenbau GmbH. One hour after initiation of the cooling, the hotplate was turned on to reach the desired heating temperature (T_H) of 300 °C. After 6 h, the hotplate was turned off while the cooling setup kept working for another hour. Subsequently, after bringing the temperature of the setup to room temperature, the sample (while it was still connected to the SS cylinder) was immersed in 1.25 M NaOH solution. After 6 h, the sample was detached from the cylinder and immersed in a fresh 1.25 M NaOH solution for another 18 h. Then, the sample was removed from the solution and subsequently rinsed with

deionized (DI)-water. The sample was dried afterwards with an air stream, while complete drying was achieved by vacuum drying at room temperature overnight.

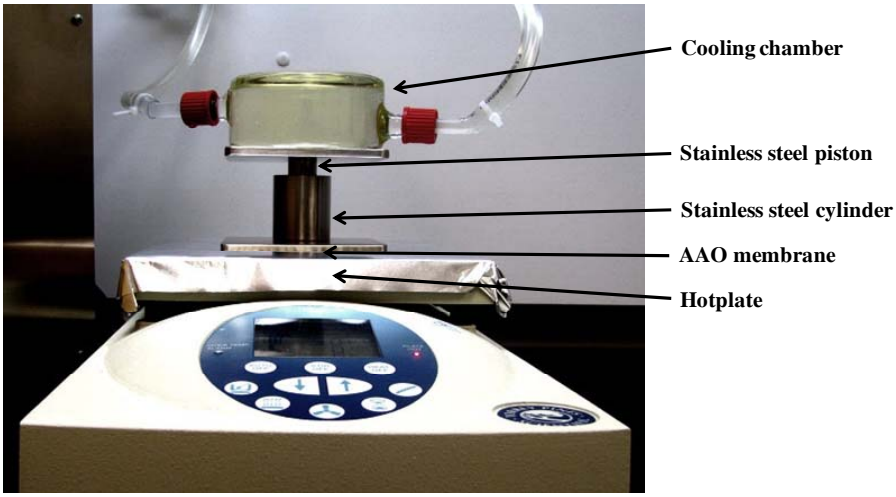

Figure B.1. Setup used for fabrication of bi-level Teflon AF nanopillars. The AAO mold was heated from the bottom by a hotplate while it was cooled down from the top using the cooling system placed over the SS piston above the polymer.

Typical atomic force microscopy (AFM) images (topography scans) for samples A, B, C, and D (processed at the cooling temperatures of –20, 0, 20, and 40 °C, respectively) are shown in Figure B.2. The topography images are used to determine the roughness average (R_a) value for each sample.

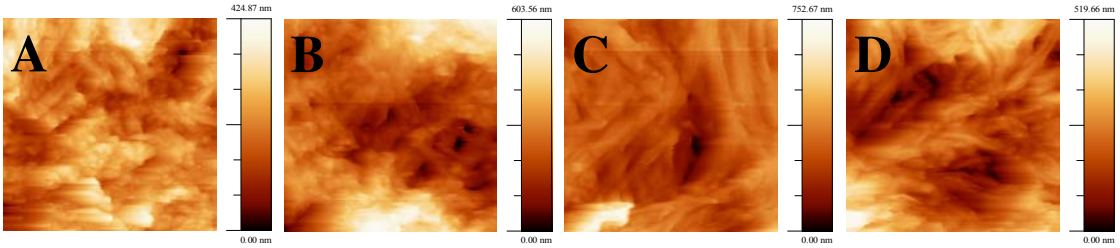

Figure B.2. Characteristic topography AFM images taken from a 5×5 μm^2 area of bi-level Teflon AF nanopillars processed at the cooling temperature of (A) -20 °C, (B) 0 °C, (C) 20 °C, and (D) 40 °C (samples A, B, C, and D, respectively).

The formation of the fluffy nanostructure on top of the base nanopillars depended strongly on the presence of the SS cylinder, which was placed on top of the polymer, in order to cool it from the top (see Figure B.1). Samples prepared at ambient conditions (T_H = 300 °C; T_C = 24±1 °C), without the SS on top, had more of a planar sheet-like terminating nanostructure on top, as can be seen in Figure B.3.

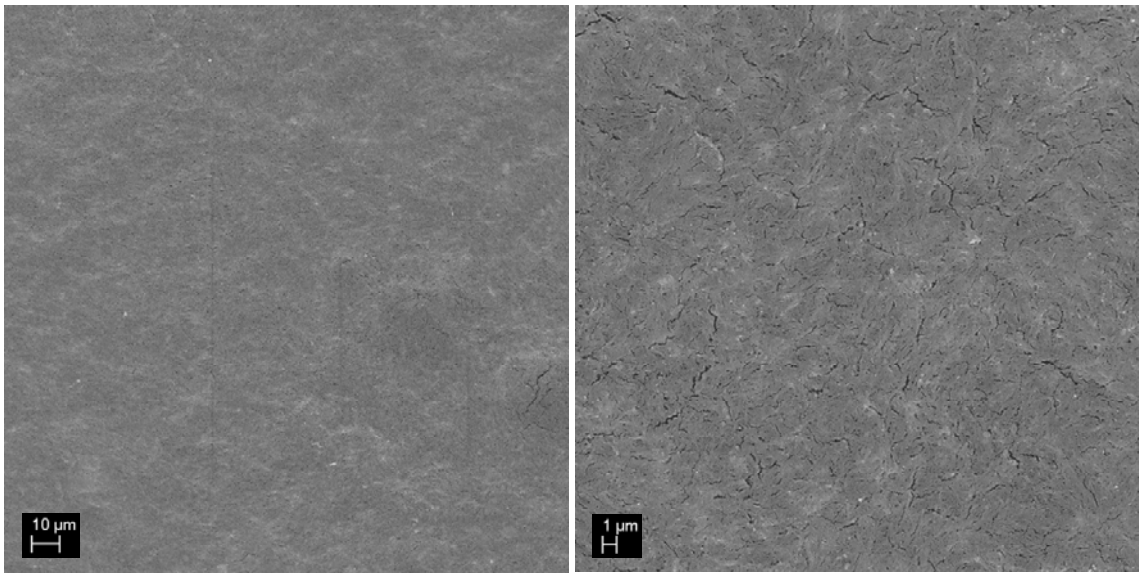

Figure B.3. Scanning electron microscope (SEM) images (top-view) of bi-level Teflon AF nanopillars processed at the heating temperature of 300 °C but at ambient conditions (24±1 °C) without the cooling system or either the SS cylinder on top. SEM images are taken from one sample at different magnifications.

To fabricate perfectly flat Teflon AF sheets, as control samples, the polymer granules were placed in an orderly fashion over a bare silicon wafer on a hotplate. Both the silicon wafer and polymer granules were covered with a glass Petri dish to reduce the chance of air dust contamination of the samples. The temperature was slowly ramped to 340 °C, where the

polymer was processed for 9 h. Then, after cooling the setup down to room temperature, the silicon wafer and the transparent bubble-free Teflon AF sheet, which was still attached to the silicon wafer, were immersed in 1.25 M NaOH solution. After detachment of the polymer sheet from the silicon wafer, it was separately immersed in a fresh 1.25 M NaOH solution. At the end, after four more hours, the polymer sheet was removed from the solution, rinsed with DI-water, and dried afterwards with an air stream [29].

The surface energy of the polymer melt at various temperatures (see Figure B.4) in the range of 260 to 360 °C was measured by the Axisymmetric Drop Shape Analysis (ADSA) approach using a home-built setup. In this method, a polymer pendent drop was formed inside an optical viewing cell consisting of an electrically heated SS cylinder (30 mm in diameter and 25 mm in length) with two sapphire windows perpendicular to the cell axis. The pendent drop was suspended at the tip of a heated SS rod and every one minute, an image was taken from the polymer droplet. When the surface tension, determined from analyzing the digitized image using the Laplace equation of capillarity, was fairly constant (*i.e.*, having < 5% deviation) for at least 1 h, the surface was considered to have reached equilibrium. The equilibrium surface tension values measured are reported in Figure B.4. Each point on surface energy on the figure is an average from three equilibrium surface tension values obtained in independently replicated experiments, while each error bar signifies the corresponding standard deviation. Further details regarding the setup and the analysis of the surface energy measurement test can be found in the paper by Park *et al*. [154]. The thermal

conductivity of Teflon AF at 300 °C was determined from extrapolating the thermal conductivity vs. temperature results reported in the range of ~60 to 200 °C by Scheirs [25].

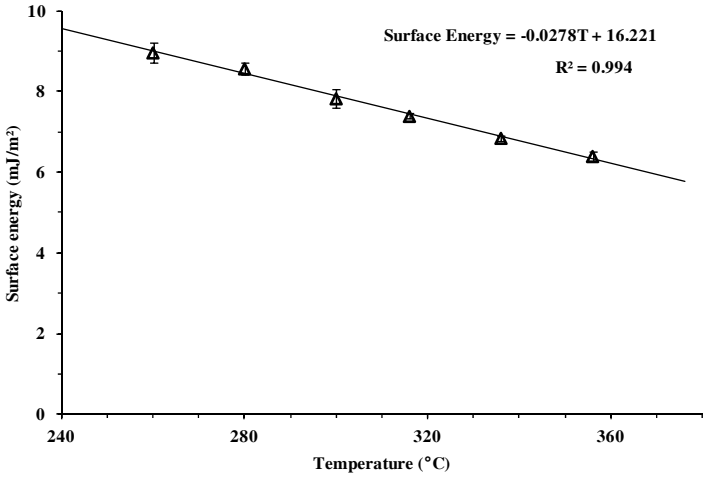

Figure B.4. Surface energy of Teflon AF melt at various temperatures in the range of 260 to 360 °C. The surface energy of the polymer was measured using the ADSA method.

The adhesive and frictional properties of bi-level Teflon AF nanopillars as well as those of the flat control samples were characterized by indentation and load-drag-pull (LDP) tests. In a characteristic indentation test, a hemispherical fused silica probe (8 mm in diameter) was pressed at a constant speed of 1 μm/s on the sample surface until the normal force reached the maximum preset force of the so-called preload (~5, 10, 25, or 50 mN). After holding the probe for 30 s at the particular preload, the probe was pulled up at a constant speed of 1 μm/s until it completely detached from the substrate. In a LDP test, the same hemispherical fused silica probe was pressed to the sample surface at the same loading speed of 1 μm/s (loading step) until the normal force reached the desired preload of ~5, 10, 17.5, or 25 mN. After holding the probe for 30 s and under constant load, the probe was dragged over the sample

surface at a constant speed of 10 μm/s (dragging step) for a 500 μm distance. At the end of the dragging course, the probe was instantaneously moved upward at the same unloading speed of 1 μm/s (pulling step) until it completely detached from the surface.

Characteristic force traces (*i.e.*, normal force vs. displacement) in indentation tests under the nominal preload of 50 mN are plotted in Figure B.5.A for all samples, including flat control samples as well as bi-level Teflon AF nanopillars of various geometrical properties. The ultimate penetration depth (L_{pd}) of the fused silica probe in bi-level Teflon AF nanopillars and also in the flat control samples at different preloads was used to measure the apparent surface area at the contact zone (a_{con}) by $a_{con} = \pi L_{pd} (d' - L_{pd})$, where d' is the probe diameter (8 mm) [63]. As illustrated in Figure B.5.B, within the applied preload range of ~5–50 mN, the change of the surface area with preload is linear for all samples, except for sample A. As can be seen in Figure B.5.B, the apparent area of contact for sample A, beyond the preload of 25 mN, did not increase linearly. In fact, as sample A is very soft, the probe penetration depth exceeded the length of the nanopillars (*i.e.*, ~25 μm) under elevated preloads; that is, pressures beyond 25 mN involved the backing layer in holding the normal force, which led to a shift in the trend of surface area changes at the highest applied preload. However, it should be noted that sample A had the largest surface area in comparison to other samples due to its relatively softer structure. In general, under an identical preload, the softer the surface is, the deeper the probe penetrates and the larger the area of contact is.

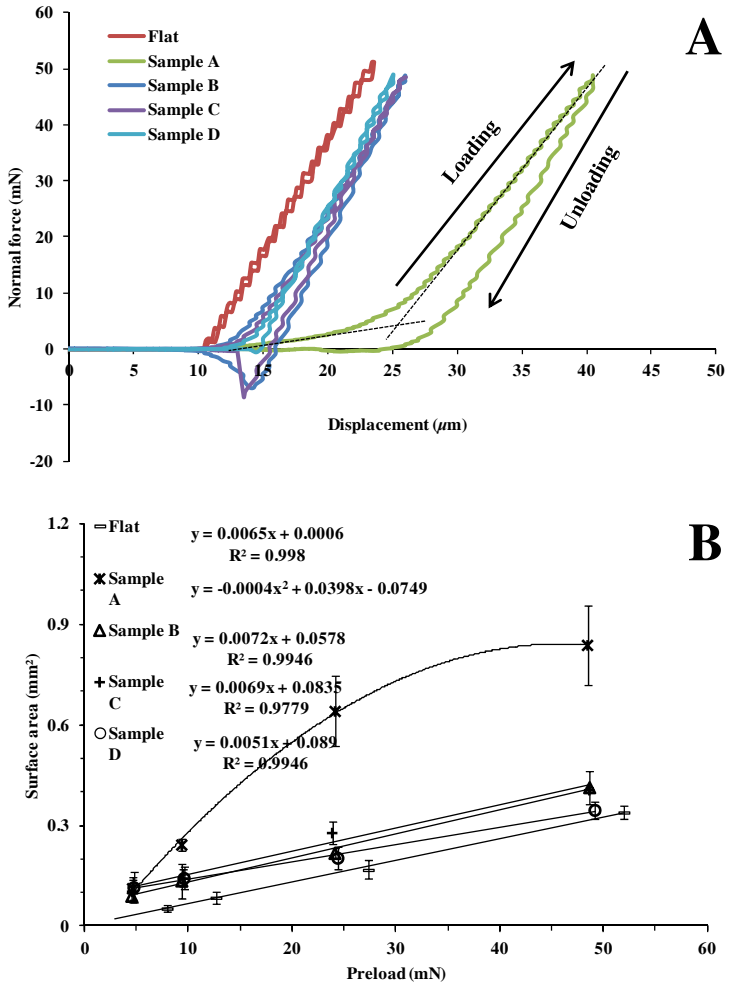

Figure B.5. (A) Typical force traces (normal force vs. displacement) for different nanopillars processed at the cooling temperatures of –20, 0, 20, and 40 °C (samples A, B, C, and D, respectively) as well as for flat control samples under a nominal preload of 50 mN. For the sake of visual clarity, the plots do not include the 30 s holding time between the loading and unloading steps. The dashed lines show the linear fits for the loading stage for sample A. (B) Apparent surface area for the same bi-level Teflon AF nanopillars as well as the flat control samples under nominal preloads of 5, 10, 25, and 50 mN.

It should be noted that the force vs. displacement plots of Figure B.5.A do not include the 30 s holding time applied during the indentation tests. As a matter of fact, there are some fluctuations in the original force vs. displacement data during the 30 s holding time because of the possible creeping of the samples at that time and also the deflection of the indentation machine (~0.5 μm) at the start of the unloading step and upon changing the direction of its

movement (see Figure B.6.A). Therefore, for the sake of visual clarity, a deflection distance of ~0.5 μm has been considered for all samples and accordingly adjusted for them (see Figure B.6.B), while the 30 s holding time was eliminated from all the plots reported in Figure B.5.A.

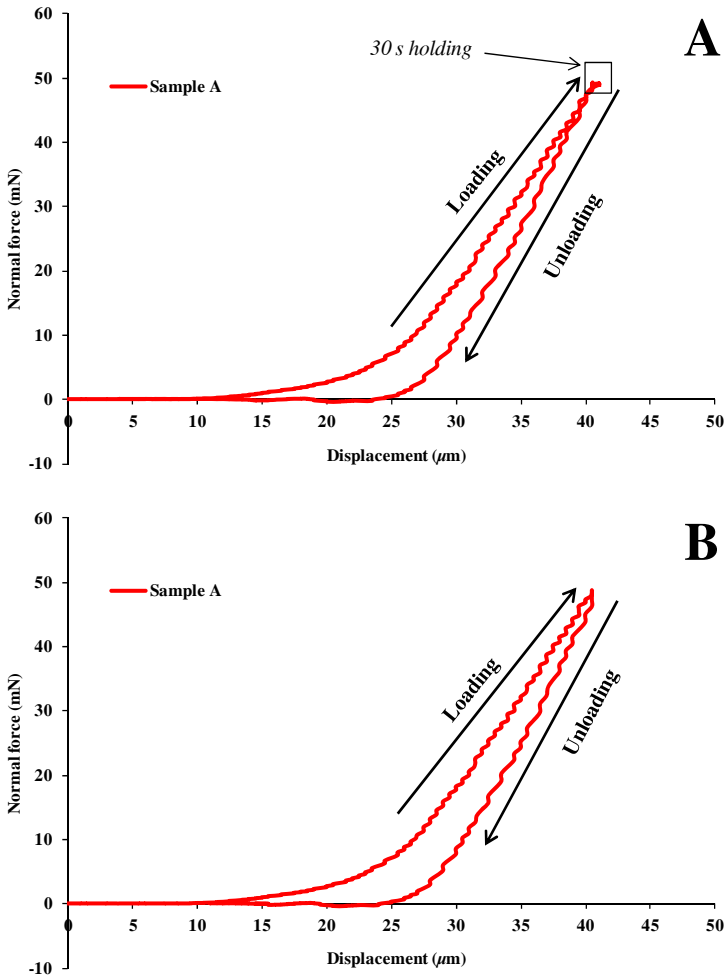

Figure B.6. (A) Original characteristic normal force vs. displacement trace for bi-level Teflon AF nanopillars processed at –20 °C (sample A). (B) The same normal force vs. displacement trace after removal of the 30 s holding time from the plot and adjusting the ~0.5 μm deflection of the indentation machine.

Last but not least, the pull-off forces measured upon detaching the fused silica probe from bi-level Teflon AF nanopillars in LDP tests are presented in Figure B.7. The deviation from indentation tests and also large error bars for pull-off force results of LDP tests (Figure B.7) were obtained because of the unpredictable nature of the partial surface discharge, which took place upon unloading the probe from the nanopillars.

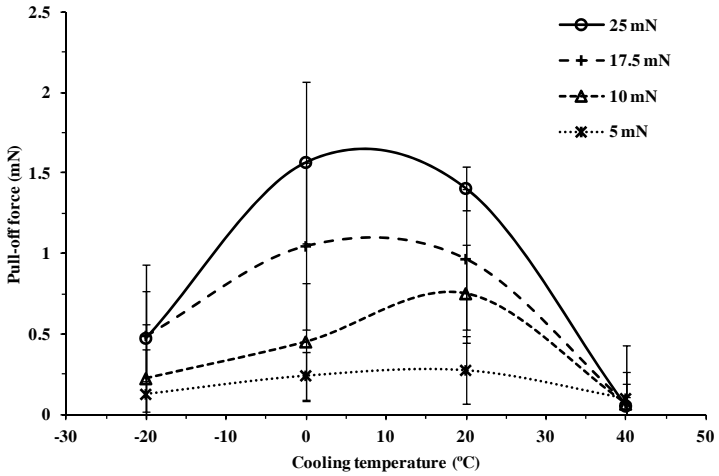

Figure B.7. Pull-off force values measured upon unloading in LDP tests at various preloads of 5, 10, 17.5, and 25 mN for different nanopillars processed at the cooling temperature of –20, 0, 20, and 40 °C (samples A, B, C, and D, respectively).

Appendix C. Supporting Information for Chapter 7

During charge measurement tests, as a gecko foot pad was brought into contact with the polymer thin film, electric charges were separated at the contact interface, leading to induction of an image charge on the backing copper sheet. During contact, and even after separation of the gecko foot pad from the substrate, the sign and density of the induced image charges (σ_{image}) were concurrently recorded by an electrometer (Model 6517A Electrometer/High Resistance Meter from Keithley Instruments), which was connected to the back of the copper sheet. Using σ_{image} and neglecting the effect of charge backflow via tunneling [31,36], the actual surface charge density over the polymer (σ_s) during contact was determined by [149]

$$\sigma_{image} = \sigma_s \left(\frac{D + d_i + d_g}{\frac{(h_i - d_i)}{\varepsilon_i} - \frac{d_g}{\varepsilon_g} + \frac{D}{\varepsilon_D}} \right)$$

Equation C.1

where D is the actual separation distance between the setae and the thin film; d_i and d_g are the charge penetration depths in the polymer and the nano-spatula at the tip of each seta, respectively. h_i is the thickness of the polymer thin film, and ε_i, ε_g, and ε_D are the dielectric constants of the polymer, the seta, and the separating medium, respectively. For after-contact charge measurements, however, when the gecko foot pad is pulled away from the polymer thin film, the measured image charge density (σ_{image}) is essentially equal to the actual surface charge density over the polymer (σ_s), and no further calculation is required [149].

In calculating the surface charge density during contact, since gecko toe pads come into intimate contact while both the nano-spatulas of gecko setae and polymer surfaces are perfectly smooth at a sub-nanometer scale (see Table 7.1), the actual separation distance, D, was considered as that of the interatomic separation distance of ~0.3 nm [2,84]. The charge penetration depths, d_i and d_g, were considered equal and approximated by 3 nm [111]. The charge penetration depth of 3 nm was employed for all calculations because it is the upper limit of charge penetration reported for a single contact with an insulator (although lower charge penetration depths in the order of atomic dimensions, as small as 0.35±0.8 nm [112], have also been reported for a single contact with an insulator). It should be noted that using smaller charge penetration depth values for charge calculations does not affect any of the conclusions drawn herein. If, however, smaller penetration depths were used, the surface charge densities would be larger than those reported in this report, which still completely support our conclusions. The dielectric constants (ε_i) of Teflon AF and PDMS were considered as 2.65 [155] and 1.93 [25], respectively. Although the dielectric constants of the employed polymers are constant, the dielectric constant of β-keratin (ε_g), the main component of the fibrillar feature (setae) on the gecko toe pads [20,21], varies between ~4 and 20 [156-160], depending on the water uptake of the material, which depends on the environmental conditions.

In particular, keratinous materials absorb a specific amount of water depending on the humidity. Considering that absorbing water from air can dramatically alter both the dielectric constant and the conductivity of a keratinous material [156-161], and in order to reduce the

influence of the humidity history on the uptake of water by gecko foot pads, the geckos were incubated in a plastic chamber (with RH of ~100%) for ~2 h prior to both charge and adhesion tests. In addition, all tests were carried out at constant relative humidity (RH) of 50±4 % (temperature, T=24±1 °C). Therefore, for the charge calculated using Equation C.1, the intermediate value of 16 was considered for ε_g, given that it is the approximate average value reported for keratinous materials in the range of relative humidity employed for our experiments [158,159,161]. It is also worthwhile mentioning that, for charge calculations, the effect of using the lower or upper values of ε_g (*i.e.*, 4 or 20, respectively) on the final results is negligible.

Although water uptake by gecko foot pads in humid conditions does not significantly affect the charge calculations, humidity variations have proven to have a significant (and complicated) effect on contact electrification, which differs from system to system [31,36]. Therefore, RH was kept constant – yet relatively high – in all experiments. The relatively high specific RH of 50±4 % was chosen for two reasons. First, Tokay geckos, employed in this research, inhabit tropical forests where humidity levels are normally high [126]. Secondly, formation of water layers over the polymer in humid conditions can help to stabilize their surface charging [36]. Therefore, to obtain more consistent results, all experiments were performed at the relatively high and consistent RH of 50±4 %. It should be noted that water is not necessary for contact electrification to occur [36] and effective surface charging does happen in even completely dry conditions [32,33,36]. Temperature and RH

were monitored using a HI 93640N Thermohygrometer (HANNA Instruments Inc.) with resolution of ±0.5 °C for temperature measurements and ±4% for RH readings.

In calculations of charge densities by Equation C.1, the dielectric constant of the separating medium (ε_D) was considered equal to 1, the dielectric constant of air. However, it should be noted that at the RH of 50±4 % where the experiments were carried out, it is expected that small amounts of water adsorb over the polymer thin films. Since the employed polymers are hydrophobic, the thickness of the adsorbed layer of water is typically less than 0.2 nm – roughly a thickness of a monolayer of water [13]. Seeing that the dielectric constant of a monolayer of water (≈6) is not very high (as that of the bulk of water (≈80)), in charge calculations, the presence of water at the interface was ignored, since the effect of its incorporation in charge measurements was negligible.

To investigate the influence of surface charging on the adhesion of gecko foot pads, the magnitude of the total generated adhesion force against each substrate was also recorded during all the experiments. Adhesion forces were recorded using a dual-range force sensor (at the ±10 N range with ±0.01 N resolution; Vernier Software & Technology, LLC.), which was connected to the copper sheet – from the top – with an aluminum rod (see Figure 7.3). Force data collection was conducted by Logger Lite software (Vernier Software & Technology, LLC.), connected to the force sensor.

During adhesion tests, the gecko foot pad was dragged across Teflon AF for 2–3 mm and across PDMS for about 10 mm. This was because dragging the toes further than few millimeters over Teflon AF led to a significant increase in surface forces that the fibrillar lamellae on the gecko toe pads were pulled off the toe. Therefore, to obtain consistent results without damaging the fibrillar feature of the toes, the foot pad was dragged for only few millimeters over Teflon AF to saturate the shear forces (up to 6–7 N/cm^2). Over PDMS, on the other hand, since less adhesion occurred (maximum up to ~1.5 N/cm^2), the foot pads could be dragged further. In order to reach the saturation shear adhesion forces, the foot pads were dragged about 10 mm over PDMS, which did not cause any damage to the fibrillar feature of the toes.

The magnitude of the van der Waals (vdW) interaction force between two smooth solid bodies, such as that between gecko toes and the polymer substrates, can be theoretically determined with the Hamaker method [74,98]. According to the Hamaker method, the vdW-driven force (F_{vdW}) interacting between phase 1 (a tip of a nano-spatula (considered as a curved segment of a sphere with radius, $R \approx 2$ μm) [2]) and phase 2 (polymer thin film) across medium 3 at the separation distance D can be calculated by $F_{vdW} = -A_{132}R/6D^2$ [2], where A_{132} is the Hamaker constant between phase 1 and phase 2, interacting across medium 3. Since the geometry of contact on both Teflon AF and PDMS is the same, the difference between the vdW interactions of the employed polymers can be simply reduced to the difference between their Hamaker constants for contact with gecko foot pads. The corresponding Hamaker constant for each system can be determined according to the Lifshitz

model [99], where multi-body interactions are considered in the presence of a continuous separating medium. Considering the dielectric constant of Teflon AF as 1.93 and its refractive index as 1.31 (which are the lowest dielectric constant and refractive index of all solid organic polymers) [25], the Hamaker constant for Teflon AF-seta contact would be 5.1×10^{-20} J. On the other hand, PDMS, which has a larger dielectric constant (2.65) [155] and refractive index (1.41) [155] than Teflon AF, has a Hamaker constant of 6.5×10^{-20} J (~1.3 times larger than that of Teflon AF) when in contact with a gecko seta. In contact with both substrates, the dielectric constant and refractive index of seta was considered as those of keratin and equal to 16 (as discussed earlier) and 1.55 [162], respectively.

The magnitude of the electrostatic interaction force (F_{elc}) that was generated between the gecko toe pad and the substrate can simply be determined from [97,122]

$$F_{elc} = -\frac{a\sigma_s^2}{2\varepsilon_0\varepsilon_r}$$

Equation C.2

where a is the area of contact, σ_s is the contact surface charge density, ε_0 is the permittivity of free space, and ε_r is the effective dielectric constant of the contact interface; ε_r can be obtained from

$$\frac{D + d_i + d_g}{\varepsilon_r} = \frac{D}{\varepsilon_D} + \frac{d_i}{\varepsilon_i} + \frac{d_g}{\varepsilon_g}$$

Equation C.3

where D is the actual separation distance between the foot pad and the polymer thin film, while d_i and d_g are the charge penetration depths in the polymer and the nano-spatula at the

tip of each individual seta, respectively; ε_i, ε_g, and ε_D are the dielectric constants of the polymer, the gecko fibrils (setae), and the separating medium, respectively.

In calculations of CE-driven adhesion forces by Equation C.2 and C.3, the dielectric constant of the separating medium (ε_D) was again considered equal to the dielectric constant of air (*i.e.*, 1). However, it is worthwhile mentioning that by considering even a monolayer of water at the interface (which is doubtful to form on such hydrophobic materials as Teflon AF and PDMS at RH of 50±4 %), the force calculations would change by less than ~20%; in particular, the effective dielectric constant of the interface (ε_r) for Teflon AF would change from 3.1 to 3.5 while that of PDMS would go up from 3.9 to 4.6, leading to approximately 20% change in force calculations.